CONTENTS

Navid Moshtaghi Yazdani
Experimental Evaluation of the Effects of Structural Changes on the Vibration Properties of CK35 Steel 53

Damak Hanen
The Practical Feedback Stabilization for Evolution Equations in Banach Spaces 58

Mohammad Javad Fotuhi, Zafer Bingul
Comparative Study of the Parallel and Angular Electrical Gripper for Industrial Applications 66

Marcin Kalinowski, Zbigniew Kamiński
Measurement and Evaluation of Functional and Operational Coefficients of Hydraulic Solenoid Valve Prototypes Used for Variable Valve Timing Control in Combustion Engines 74

Onur Şahin, Barış Erbaş, Brent Wilson
Approximate Formulation of the Rigid Body Motions of an Elastic Rectangle under Sliding Boundary Conditions 82

Hoang Lan Ton-That
Plate Structural Analysis Based on a Double Interpolation Element with Arbitrary Meshing 91

Włodzimierz Balicki, Paweł Głowacki, Leszek Loroch
Birds Strike – Impact on the Safety of Civil Aircraft Operations in Poland in 2008- 2018 100

Abstracts XI

ABSTRACTS

Navid Moshtaghi Yazdani
Experimental Evaluation of the Effects of Structural Changes on the Vibration Properties of CK35 Steel

The microstructure of some components which operate in high-temperature conditions (e.g. boiler components, turbine blades used in gas power plants, jet engines and reactors) is subjected to changes in long run, which leads to a degradation in the mechanical properties of these components and consequently, reduces their lifecycle. Therefore, it is so useful to detect the changes in the microstructure of these parts during their operation, employing an easy, fast and non-destructive method to determine their remaining life. In this study, we evaluate the effects of the microstructural changes on natural frequencies and the damping coefficient of CK35 steel, employing the experimental modal test. We aim to use the method for power plant components, if it has significant effects. To do so, we applied spheroidization heat treatment on CK35 steel samples having a primary structure of ferrite-pearlite for 24 and 48 hours. Then, we carried out the experimental modal test on samples having different metallurgical structures, but with the same dimensions and weights. According to the findings, the spherical ferrite-carbide particles in the ferrite structure increase the natural frequencies and damping coefficient. These tests show that the structural changes in this type of steel result in slight changes in the values of natural frequencies; however, it significantly changes the damping frequencies.

Damak Hanen
The Practical Feedback Stabilization for Evolution Equations in Banach Spaces

This paper investigates the notion of practical feedback stabilization of evolution equations satisfying some relaxed conditions in infinite-dimensional Banach spaces. Moreover, sufficient conditions are presented that guarantee practical stabilizability of uncertain systems based on Lyapunov functions. These results are applied to partial differential equations.

Mohammad Javad Fotuhi, Zafer Bingul
Comparative Study of the Parallel and Angular Electrical Gripper for Industrial Applications

The aim of this paper is to study the position and power performances of an electrical lead screw-driven industrial gripper mechanism (LSDIGM). This work consists of designing and developing an electrical LSDIGM that has the potential to meet various demands in the automation industry and factories. The performances of both angular electrical gripper (AEG) and parallel electrical gripper (PEG) mechanisms were compared based on their position and power efficiency. The position efficiency of these electrical LSDIGM is computed from the position root mean square error (PRMSE) obtained from errors between the two measured positions (input incremental encoder and output linear encoder). In the experimental setup, a current sensor and a spring were employed to measure the current in the input of the system and the stiffness in the output of the system, respectively. The electrical power in the input of the electrical LSDIGM and the mechanical power in the output of the LSDIGMs were calculated using the current and the spring force, respectively. Finally, the power efficiency of these electrical LSDIGMs was examined and compared at different velocity circumstances.

Marcin Kalinowski, Zbigniew Kamiński
Measurement and Evaluation of Functional and Operational Coefficients of Hydraulic Solenoid Valve Prototypes Used for Variable Valve Timing Control in Combustion Engines

This paper describes the engineering structure and functions of a typical solenoid valve used in hydraulic mechanisms that are based on variable camshaft timing (VCT). The main operating parameters and functional utility coefficients of hydraulic solenoid valves have been defined. Tests of 10 reference and 10 prototype valves were run on a test stand for a comparative assessment of both engineering concepts based on Welch and Mann–Whitney statistical tests of the mean values of designated coefficients. The studies identified differences between both designs, and the obtained research material was used as an input to improve the performance of the engineered concept. To perform a final evaluation of the effects that arise as a result of changes introduced to some functional–operational coefficients, additional tests are required to be run on an engine testbed. The applied test methodology may then be used for control and verification tests of the valves, which can further be used in VCT technology.

Onur Şahin, Barış Erbaş, Brent Wilson
Approximate Formulation of the Rigid Body Motions of an Elastic Rectangle under Sliding Boundary Conditions

Low-frequency analysis of in-plane motion of an elastic rectangle subject to end loadings together with sliding boundary conditions is considered. A perturbation scheme is employed to analyze the dynamic response of the elastic rectangle revealing nonhomogeneous boundary-value problems for harmonic and biharmonic equations corresponding to leading and next order expansions, respectively. The solution of the biharmonic equation obtained by the separation of variables, a consequence of sliding boundary conditions, gives an asymptotic correction to the rigid body motion of the rectangle. The derived explicit approximate formulae are tested for different kinds of end loadings together with numerical examples demonstrating the comparison against the exact solutions.

Hoang Lan Ton-That
Plate Structural Analysis Based on a Double Interpolation Element with Arbitrary Meshing

This paper presents the plate structural analysis based on the finite element method (FEM) using a double interpolation element with arbitrary meshing. This element used in this research is related to the first-order shear deformation theory (FSDT) and the double interpolation procedure. The first stage of the procedure is the same with the standard FEM for the quadrilateral element, but the averaged nodal gradients must be computed for the second stage of this interpolation. Shape functions established by the double interpolation procedure exhibit more continuous nodal gradients and higher-order polynomial contrast compared to the standard FEM when analysing the same mesh. Note that the total degrees of freedom (DOFs) do not increase in this procedure, and the trial solution and its derivatives are continuous across inter-element boundaries. Besides, with controlling distortion factors, the interior nodes of a plate domain are derived from a set of regular nodes. Four practical examples with good results and small errors are considered in this study for showing excellent efficiency for this element. Last but not least, this element allows us to implement the procedure in an existing FEM computer code as well as can be used for nonlinear analysis in the near future.

Włodzimierz Balicki, Paweł Głowacki, Leszek Loroch
Birds Strike – Impact on the Safety of Civil Aircraft Operations in Poland in 2008- 2018

The authors assessed the real threat to civil aircraft traffic in Poland resulting from bird strikes. It was found that in the period 2013–2018, the probability of such events increased by four times. Data for this work were downloaded from the ECCAIRS database maintained by the Civil Aviation Authority. Air traffic events have been collected for several years in this database. An assessment of the energy of bird collision with the aircraft, resulting from the bird's mass and relative speed of movement, was also presented. Ways to minimise the risk of collision were described by introducing crew warning systems and means to scare off birds from the airport grounds. The method of testing the resistance of turbine engines to the foreign body's absorption was also shown, as well as design methods for increasing the engine resistance to bird strikes.

sciendo

DOI 10.2478/ama-2021-0008

acta mechanica et automatica, vol.15 no.2 (2021)

EXPERIMENTAL EVALUATION OF THE EFFECTS OF STRUCTURAL CHANGES ON THE VIBRATION PROPERTIES OF CK35 STEEL

Navid Moshtaghi YAZANI*

*Department of Mechanical Engineering, University of Tehran, 16th Azar St., Enghelab Sq., Tehran, Iran

navid.moshtaghi@ut.ac.ir

received 29 January 2021, revised 8 May 2021, accepted 12 May 2021

Abstract: The microstructure of some components which operate in high-temperature conditions (e.g. boiler components, turbine blades used in gas power plants, jet engines and reactors) is subjected to changes in long run, which leads to a degradation in the mechanical properties of these components and consequently, reduces their lifecycle. Therefore, it is so useful to detect the changes in the microstructure of these parts during their operation, employing an easy, fast and non-destructive method to determine their remaining life. In this study, we evaluate the effects of the microstructural changes on natural frequencies and the damping coefficient of CK35 steel, employing the experimental modal test. We aim to use the method for power plant components, if it has significant effects. To do so, we applied spheroidization heat treatment on CK35 steel samples having a primary structure of ferrite-pearlite for 24 and 48 hours. Then, we carried out the experimental modal test on samples having different metallurgical structures, but with the same dimensions and weights. According to the findings, the spherical ferrite-carbide particles in the ferrite structure increase the natural frequencies and damping coefficient. These tests show that the structural changes in this type of steel result in slight changes in the values of natural frequencies; however, it significantly changes the damping frequencies.

Keywords: microstructure, spheroidization heat treatment, modal analysis, natural frequency, damping

1. INTRODUCTION

Changes in metal microstructures can influence their macroscopic properties. A change in microstructure can be the formation of a new phase in the metal matrix, a change in the size of a grain or the size of a phase and/or sediment particles in a metal matrix. Some of the mechanical properties including toughness, yield strength and elasticity modulus, as well as some vibration properties such as natural frequencies and damping coefficient, may be influenced by changes in the metal microstructure. Numerous studies have been carried out regarding the influences of microstructure on the mechanical properties of metals. For example, Zieliński et al. (2017) evaluated the effects of ageing heat treatment on T24 steel microstructure and its mechanical properties. They concluded that as the ageing duration and its temperature increase, the steel mechanical properties degrade, which can be attributed to some reasons including the metal matrix recovery, removing the layers of bainitic structure, an increase in the size of carbides M23C6, as well as the formation of secondary sediments of M2C and M6C3 in the metal matrix. Carneiro et al. (2018) addressed the influence of ageing in the microstructural aspects in an A356 alloy and its impact in the static and damping. This study analyses the role of T6 heat treatments in the overall microstructure of A356 poured in ceramic block, associating the morphology transformations with the internal mechanisms that enhance yield strength and reduce damping. They suggested that these variables display an inverse proportionality and a linear model is determined for the design of alloys with tailored yield/damping by the use of different artificial ageing times. Carneiro, V.H., and Puga, H. (2018) investigated the influence of solution treatment in the microstructural aspects (e.g. eutectic Si spheroidization) in an A356 alloy and its impact in the static and damping. Their findings owing to eutectic Si coarsening/spheroidization, Mg2Si/π-phase dissolution and α-Al solution strengthening, the solution treatment can enhance both static (yield strength) and dynamic (damping ratio) mechanical properties. As well, several other studies can be found in the field of microstructure influences on the mechanical properties of a metal (Bhardwaj et al., 2021; Diehl et al., 2010; Yamada et al., 2006; Liu et al, 2012; Ghorbanhosseini et al., 2020; Korznikova et al., 2020; Wang et al., 2020; Ghosh et al., 2008).

Hamisi et al. (2018) studied the ageing effects on the mechanical and vibration properties of SA516 carbide steels. They suggested that an increase in the ageing duration can degrade the samples' mechanical properties, reduce their natural frequencies and increase the samples damping properties. Tsai, M. H. et al. (2011) addressed the effects of ageing heat treatment on vibration properties of an Mg-Zr alloy. They concluded that as the ageing heat-treatment temperature increases, some twin structures are formed in the alloy matrix, which plays a significant role in changing the samples' damping coefficients. El-Morsy, A. W., & Farahat, A. I (2015) investigated the effects of ageing heat-treatment duration on the damping of Mg-6Al-1Zn alloy. They found that increasing the ageing duration, the number of settled phases also increases. They showed that the ageing of this alloy up to 34 hours can increase its damping properties, and the damping value decreases, as the ageing duration increase. Carneiro, V.H., and Puga, H. (2019) studied the impact of microstructure and T6 heat treatment on Young's modulus and internal friction. Moreover, some other studies have addressed the influences of microstructure on metal vibration parameters (Lin et al., 2002; Limarga et al., 2007; Cai et al., 2005).

DOI 10.2478/ama-2021-0008

As mentioned earlier, the changes in metal structures may influence their mechanical and vibration properties. Therefore, by employing some methods to investigate the mechanical and vibration properties of metals, it is possible to find the changes in the data profile of their structure, without a need to use metallography methods. In this study, we employed a modal non-destructive test to find the data profile of metal structures. In other words, using a modal test and analysing its results, rather than employing destructive tests such as metallography and hardness measurement tests, can one discover the changes in data profiles of metal structures that operate in superheated conditions. Therefore, we chose the CK35 steel having a primary structure of ferrite-pearlite and observed that the maximum changes occurred in its structure, as spheroidization heat treatment applied. It is worth mentioning that we chose this kind of heat-treatment process to induce the maximum changes in the steel structure to conclude that how much the maximum changes in the structure will change the steel vibration properties of the steel. Then, we applied the modal experimental test and hammer test for samples having completely the same dimensions and different structures.

2. EXPERIMENTAL PROCESSES

2.1. Heat treatment

To study the effects of microstructure changes on the steel vibration properties, employing a heat-treatment process causing a significant change in the structure is considered suitable. In this study, we chose CK35 steel having the primary structure if ferrite-pearlite. The chemical composition of this steel is shown in Tab. 1, according to optical emission spectrometry test and ref. 21. The maximum change in ferrite-pearlite structure occurs when the cementite layers in the pearlite phase are dispersed spherically in the ferrite structure, which can be reached by applying the spheroidization heat-treatment process.

As the spheroidization heat-treatment process in the natural mode can be so time-consuming, the process can be much less time-consuming if the primary structure is martensite (Chandler, 1998; Totten, 2006). Therefore, the samples maintained in the furnace at an austenite temperature for enough time (about 1 hour) to reach a complete austenite structure, and immediately they were cooled, so that they reached a martensite structure. Then, the samples were heated at 700° to reach spherical structure in their matrix, 2 of which for 24 hours and the other 2 for 48 hours (Chandler, 1998). Following, the samples cooled in the furnace.

Tab. 1. Chemical properties of the CK35 steel, weight percentage (%)

	C	M	P	S
Optical emission spectrometry test	0.34	0.621	0.0121	0.018
Ref. 21	0.32–0.38	0.6–0.9	Max. 0.04	Max. 0.05

2.2. Frequency response

The modal test is an experimental technique to find the modal model for a vibration system. This theory is based on the relationship between the vibration response in a certain point of the structure and the excitation at the same point or other points as a response to the excitation frequency. The relationship that is often in a form of a mathematical complex function is called the frequency response function (FRF). The modal test includes the FRF measurements and the structure impact response. In other words, one can easily measure the FRF, exerting a (measured) force at a certain point of the structure, in the absence of other excitement forces, and measuring the vibration response in one or more points of the structure [24].

In this study, we employed the modal test, as well as the hammer test, by the help of which can one obtain the natural frequencies and damping values of the samples. As the samples' natural frequencies and the damping values are compared in this study, the samples should have as the same dimensions and weights as possible to investigate the effects of microstructure changes on the steel vibration properties. Fig. 1 shows the prepared samples for the test. The sample weights are equal to 633.33 ± 0.02 g, and their dimensions are the same in a 0.01-mm precision range (Fig. 1).

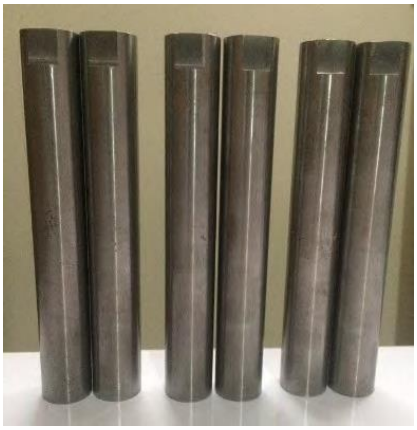

Fig. 1. Prepared samples for the modal test

Fig. 2 and Fig. 3 shows how this test is carried out and the tools used in the test. The test applied to samples in free-free boundary conditions. To obtain the samples' vibration properties, their frequency response (FRF) should be explored. To this end, a hammer (Type 8202 Bruel & Kjae) and a piezoelectric accelerometer employed to excite the samples and to measure their responses, respectively. It should be mentioned that the test was carried out in several different points of the samples. As well, applying 10 hits and averaging the responses, each sample frequency response was obtained.

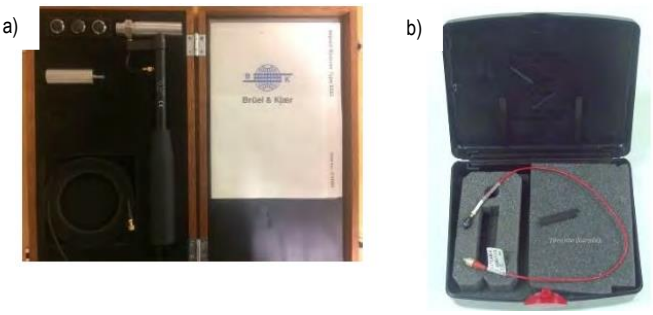

Fig. 2. Used tools in the modal test: a) Hammer and its accessories; b) piezoelectric accelerometer

Fig. 3 Four-channel data collection model, model 3560 c

Then, the damping coefficients were obtained, using frequency responses and employing the peak-peaking technique (half-power bandwidth) (Fig. 4). In this technique, the damping coefficient can be conveniently calculated, using eq. 1. In this method, the maximum amplitude (i.e. $|\alpha W_r|$) that is related to the natural frequencies of each vibration mode of the system is first obtained, and then the frequencies (W_b, W_a) are chosen at both sides of the resonance peak having an amplitude of $\frac{|\alpha W_r|}{2}$.

The damping loss factor is obtained from eq. 1, according to the peak resonance width (Fu, Z. F., & He, J, 2001).

$$\eta_r = \frac{W_b^2 - W_a^2}{2W_r^2} = \frac{W_b - W_a}{W_r} \quad (1)$$

where W_r is the maximum frequency of the diagram amplitude, and W_r and W_b are the frequencies at both sides of the peak resonance.

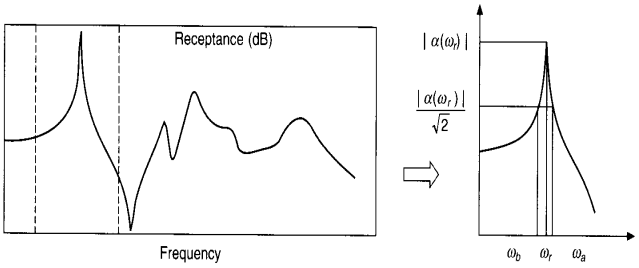

Fig. 4. Peak-peaking technique to calculate the damping loss factor

2.3. Tensile test

To study the effects of heat-treatment process on the steel elasticity modulus – that is considered as an important parameter influencing the natural frequency value – some samples were prepared according to ASTM E8/E8M. The gauge length and diameters of these samples were 25 and 6 mm, respectively, that is categorized as sub-size samples according to the standard.

3. FINDINGS AND DISCUSSIONS

3.1. Microstructure

Fig. 5a shows the steel microstructure before applying the spheroidization heat-treatment process. As can be seen, the steel structure consists of ferrite and pearlite phases; the ferrite phase is shown in white, while the pearlite phase is brown. Fig. 5b and 5c shows the steel microstructure after spheroidization heat treatment after 24 hours and 48 hours respectively. As can be observed in these figures, after applying the spheroidization heat-treatment process, the cementite phases which are placed in the pearlite structure in a layered manner will be distributed spherically and dispersedly in the ferrite matrix. According to Fig. 5b and 5c, one can conclude that there exists no significant difference between the samples heat treated for 24 hours and those processed for 48 hours. In other words, it seems that once the samples are heat treated for 24 hours, the cementite phase sizes are saturated, and increasing the heat-treatment time incurs no significant changes in the size of these phases. Therefore, according to the microstructures shown in the figures, it seems that the results of the modal test and the tensile test that was applied to samples heat treated for 24 and 48 hours have no significant differences.

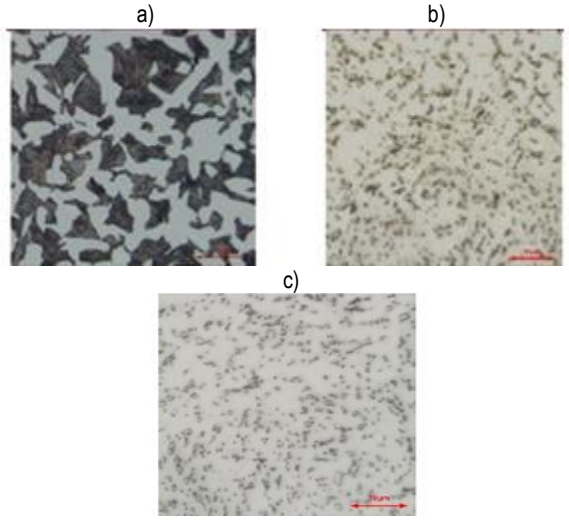

Fig. 5. Microstructures: (a) the sample before applying heat-treatment process, with a magnification factor of 200×, Nital etch solution 3%; (b) heat-treated sample for 24 hours with a magnification factor of 1000×, Picral etch solution, 4%; and (c) heat-treated sample for 48 hours with a magnification factor of 1000×, Picral etch solution, 4%

3.2. Results of the modal and tensile tests

As mentioned before, 2 samples of each heat-treatment process were prepared for the modal test. Figure 6 shows the obtained frequency response, following the sample excitation by the hammer. The results of the modal test are summarized in Table 2. It should be noted that these results are related to the case where the sensor installation and the hammer hit are both placed in the middle of the samples. According to the modal test results, it is observed that following the spheroidization process, the natural frequencies and the damping loss factor of the two modes of the first and second vibrations are increased. In other words, the dispersion of cementite particles within the ferrite matrix increases the natural frequencies, as well as damping loss factor. Moreover, the results show that although structural changes incur slight changes in natural frequencies, the phenomenon causes significant changes in the damping loss factor, so that the damping loss factor increases at least 14%, with a change in ferrite-pearlite structure to a spheroidized structure.

DOI 10.2478/ama-2021-0008

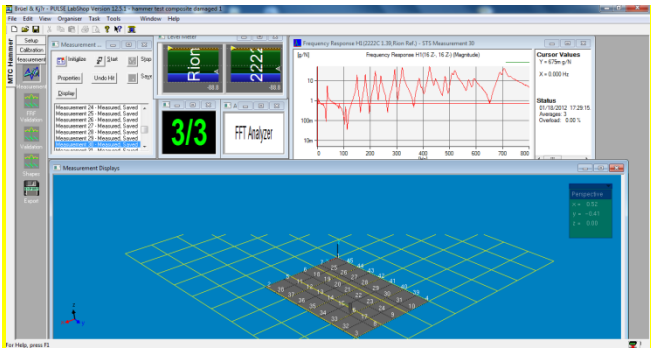

Fig. 6. Obtained frequency response following the sample excitation

Tab. 2. Results of modal test

Sample	Natural frequency (Hz)		Damping loss factor (percentage of difference compared to the non-heat-treated sample)	
	First mode	Second mode	First mode	Second mode
Non-heat treated	3722	9424	0.00204	0.00328
Heat treated for 24 hours	3735	9447	0.00257 (+0.14%)	0.00371 (+2.51%)
Heat treated for 48 hours	3734	9448	0.00280 (+0.15%)	0.00282 (+2.14%)

One can refer to the results of the tensile test (Table 3) to find a reason for the increase in natural frequencies. According to the results, the distribution of cementite particles in the ferrite phase causes the elasticity modulus to increase, which in turn leads to an increase in the natural frequency. As well, the spheroidization process can increase the phase continuity that causes an increase in damping (Visnapuu et al., 1987).

Tab. 3. Results of the tensile test

Sample	Elasticity modulus
Non-heat treated	204.80
Heat treated for 24 hours	208.50
Heat treated for 48 hours	207.29

According to the results of the modal and the tensile tests, one can see that increasing the heat-treatment duration from 24 hours to 48 hours, the natural frequencies, damping loss factor and the elasticity modulus don't change significantly. According to the microstructure similarities between samples that were heat treated for 24 hours and 48 hours, these results can be predictable.

4. CONCLUSION

This study has been carried out to find whether it is possible to use the modal test as a non-destructive test to discover the changes in metal microstructures. The experimental test results showed that the dispersion of carbide phases within the ferrite matrix increases the natural frequencies and damping loss factors. According to the results of the modal test, slight changes in the microstructure may lead to slight changes in natural frequency, while changing the structure incurs no significant changes in the damping loss factor value. According to findings, one can see that microstructure changes in this steel cause the vibration parameters to change. Therefore, the modal test – which is a cheap and fast method to obtain a system vibration data – can be employed as a non-destructive test to detect the structural changes in components that are operated in superheated conditions.

REFERENCES

1. **Abedrabbo N., Pourboghrat F., Carsley J.** (2006), Forming of AA5182-O and AA5754-O at elevated temperatures using coupled thermo-mechanical finite element models, *Internatio-nal Journal of Plasticity*, 23, 841–875.
2. **Bandara, C. S., Siriwardane, S. .C., Dissanayake, U. I., & Dissanayake, R.** (2016), Full range S–N curves for fatigue life evaluation of steels using hardness measurements, *International journal Journal of fatigueFatigue*, 82, 325-331.
3. **Akhil Bhardwaj A., Naishadh Gohil N., Amit Kumar Gupta A.K., S.S. Satheesh KumarK.S.S.** (2021), An experimental investigation on the influence of elevated-temperature constrained groove pressing on the microstructure, mechanical properties and hardening behaviour of Ti6Al4V alloy, *Materials Science and Engineering*, Volume 802., 20 January 2021, 140651
4. **Bolkowski S., Stabrowski M., Skoczylas J., Sroka J., Sikora J., Wincenciak S.** (1993), *Komputerowe metody analizy pola elektro-magnetycznego*, WNT, Warszawa.
5. **Cai, W., Lu, X. L., & Zhao, L. C**. (2005), Damping behavior of TiNi-based shape memory alloys, *Materials Science and Engineering*: A, 394 (1-2), 78-82.
6. **V.H. Carneiro V.H., H. Puga. H. (**2018), Solution Treatment Enhances Both Static and Damping Properties of Al–Si–Mg alloys, *Metall Mater Trans,* 5942–5945.
7. **V.H. Carneiro V.H., H. Puga. H.** (2019), T6 Heat Treatment Impact on the Random Frequency Vibration Stress of Al–Si–Mg Alloys. *Met. Mater. Int,* 25, 880-887.
8. **V.H. Carneiro V.H., H. Puga H., J. Meireles, J.** (2018), Heat treatment as a route to tailor the yield-damping properties in A356 alloys, *Materials Science and Engineering* 729, 1-8.
9. **Chandler, H. (Ed.).** (1994), *Heat treater's guide: practices and procedures for irons and steels*, ASM international.
10. **Diehl, A., Engel, U. &, Geiger, M.** (2010), Influence of microstructure on the mechanical properties and the forming behaviour of very thin metal foils, *Int J Adv Manuf Technol*, 47, 57-61
11. **El-Morsy, A. W., & Farahat, A. I.** (2015), Effect of aging treatment on the damping capacity and mechanical properties of Mg-6al-1Zn alloy, *The Scientific World Journal*, Volume 2015 ,pages 1-8, https://doi.org/10.1155/2015/170458
12. **Fu, Z. F., & He , J.** (2001), *Modal analysis*, Elsevier.
13. **S. Ghorbanhosseini S, ., F. Fereshteh-Saniee F., A. Sonboli. A.** (2020), An experimental investigation on the influence of elevated-temperature constrained groove pressing on the microstructure, mechanical properties, anisotropy and texture of 2024 Al sheets, *Journal of Alloys and Compounds*, 817, 152763
14. **Ghosh, S. K., & Mondal, S.** (2008), High temperature ageing behaviour of a duplex stainless steel, *Materials Characterization*, 59(12), 1776-1783.
15. **Goshima T., Hanson M.T., Keer L.M.** (1990), Three-dimensional analysis of thermal effects on surface crack propagation in rolling contact, *Journal of Thermal Stresses*, Vol. 13, 237-261.
16. **Hamisi, M.,Torshizi, S.** (2018), Experimental Study of Aging Effect on Mechanical and Vibrational Properties on Carbon Steel Sa516, *Modares Mechanical Engineering* , Vol 18, 50-55.
17. **Korznikova, G., Kabirov, R., Nazarov, K. et al.** (2020), Influence of Constrained High-Pressure Torsion on Microstructure and

Mechanical Properties of an Aluminum-Based Metal Matrix Composite, *JOM*, (72), 2898–2911.
18. **Limarga, A. M., Duong, T. L., Gregori, G., & Clarke, D. R.** (2007), High temperature vibration damping of thermal barrier coating materials. *Surface and Coatings Technology*, 202(4-7), 693-697.
19. **Lin, S. C., Lui, T. S., Chen, L. H., & Song, J. M.** (2002), Effect of pearlite on the vibration-fracture behavior of spheroidal graphite cast irons under resonantconditions, *Metallurgical and Materials Transactions A*, 33(8), 2623-2634.
20. **Shaojun LiuL., Qunying HuangH., Lei PengP., Yanfen LiL., Chunjing Li.** (2012), Microstructure and its influence on mechanical properties of CLAM stee, *Fusion Engineering and Design*: A, 89(9), 1628-1632.
21. **Totten, G. E.** (2006), *Steel Heat Treatment Handbook*, 2 Volume Set. CRC press.
22. **Tsai, M. H., Chen, M. S., Lin, L. H., Lin, M. H., Wu, C. Z., Ou, K. L., & Yu, C. H.** (2011), Effect of heat treatment on the microstructures and damping properties of biomedical Mg–Zr alloy, *Journal of Alloys and Compounds*, 509(3), 813-819.
23. **Visnapuu, A., Nash, R. W., & Turner, P. C.** (1987), *"Damping properties of elected steels and cast irons*., UNITED STATES DEPARTMENT OF THE INTERIOR
24. **Xiao-Feng Wang X-F, Tong-Ya Shi T-Y, He-Bin Wang H-B, Song-Ze Zhou S-Z, Wen-Fei Peng W-F, Yong-Gang Wang. Y-G (**2020), Effects of strain rate on mechanical properties, microstructure and texture of Al—Mg—Si—Cu alloy under tensile loading, , *Transactions of Nonferrous Metals Society of China,* 30(1), 27-40.
25. **Yamada, T., Okano, S., & Kuwano, H.** (2006), Mechanical property andmicrostructural change by thermal aging of SCS14A cast duplex stainless steel, *Journal of Nuclear Materials*, 350(1), 47-55.
26. **Zhang, Z., Zeng, X., & Ding, W.** (2005), The influence of heat treatment on damping response of AZ91D magnesium alloy, *Materials Science and Engineering*: A, 392(1-2), 150-155**.**
27. **Zieliński, A., Golański, G., & Sroka, M. (**2017), Influence of long-term ageing on the microstructure and mechanical properties of T24 steel, *Materials Science and Engineering*: A, 682, 664-672.

DOI 10.2478/ama-2021-0009

THE PRACTICAL FEEDBACK STABILIZATION FOR EVOLUTION EQUATIONS IN BANACH SPACES

Damak HANEN*

*Faculty of Sciences of Sfax, Department of Mathematics, University of Sfax, Route Soukra BP1171, 3000 Sfax, Tunisia

hanen.damak@yahoo.fr

received 28 November 2020, revised 14 May 2021, accepted 20 May 2021

Abstract: This paper investigates the notion of practical feedback stabilization of evolution equations satisfying some relaxed conditions in infinite-dimensional Banach spaces. Moreover, sufficient conditions are presented that guarantee practical stabilizability of uncertain systems based on Lyapunov functions. These results are applied to partial differential equations.

Key words: dynamical systems in control, linear operator, controllability, uncertain systems, practical stabilization, Banach spaces

1. INTRODUCTION

In the literature on control theory of time-varying dynamical systems, controllability and stabilizability are the qualitative control problems that play an important role in the systems and have attracted many researchers (Damak et al., 2016; Ikeda et al., 1972; Phat and Ha, 2008; Phat, 2001, 2002; Phat and Kiet, 2002). The theory was first introduced by Kalman et al. (1963) for the finite dimensional time-invariant systems. Furthermore, the theory which related to exponential stability was first introduced by Wonham (1967). Lyapunov function approach and the method based on spectral decomposition are the most widely used techniques for studying stabilizability of special classes of control systems, see for example Kobayashi (1989) and Tsinias (1991). In the infinite-dimensional control systems, the investigation of practical stabili-zation is more complicated and requires more sophisticated tech-niques. The practical stabilization is to find the state feedback candidate such that the solution of the closed-loop system is practically exponentially stable in the Lyapunov sense in which the origin is not necessary to be an equilibrium point. In this case, Damak et al. (2016) proved the practical feedback stabilization of the time-varying control systems in Hilbert spaces where the nominal system is a linear time-varying control system globally null controllable and the perturbation term satisfies some conditions. Kalman et al. (1963) and Wonham (1967) have shown that in the finite-dimensional autonomous control system, if the system is null controllable in finite time, then it is stabilizable. But it does not hold for the converse. Moreover, if the system is completely stabilizable, then it is null controllable in finite time. The results of stabilizability for the finite-dimensional systems can be generalized into infinite-dimensional systems. For time-invariant control systems in Banach spaces, Phat and Kiet (2002) defined an equivalence between solvability of the Lyapunov equation and exponential stability of linear system. Based on the Lyapunov theorem, a relationship between stabilizability and exact null controllability of linear time-invariant control systems is established. Moreover, they gave the exponential stabilizability of a class of nonlinear control systems. In recent years, non-autonomous differential equations on infinite-dimensional spaces have been studied by many researchers, see the references Damak and Hammami (2020), Damak (2021), Chen et al. (2020a, 2020b, 2020c, 2021) and Chen (2021) for more details. In the study by Chen et al. (2020b), sufficient conditions of existence of mild solutions and approximate controllability for the desired problem are given by introducing a new Green's function and constructing a control function involving Gramian controllability operator.

In this paper, we extend the results of Pazy (1983) and Phat and Kiet (2002) to discuss the problem of practical stabilization for evolution equations in Banach spaces. Based on the exact null controllability assumption of the linear control system, sufficient conditions for the stabilizability are established by solving a standard Lyapunov equation. Further, the nonlinear perturbation term is locally Lipschitz continuous and satisfies some appropriate growth conditions. A feedback controller that assures global practical uniform exponential stability of the closed-loop system has been proposed, that is, the solutions of the closed-loop system converge towards an arbitrary small neighbourhood of the origin.

The paper is organized as follows: Section 2 briefly introduces some notations and necessary preliminaries. Section 3 presents the required assumptions and the statement of the main results. Section 4 presents illustrative examples, which shows the importance of this study. Section 5 provides conclusion of this study.

2. PRELIMINARIES

Throughout this paper, we adopt the following notations R+ and X. R+ denotes the set of all non-negative real numbers and X denotes an infinite-dimensional Banach space with the norm ‖·‖. Let X^* be the topological dual space of X and U infinite-dimensional Banach space. Let $\langle y^*, x\rangle$ denote the value of y at x. L(X) (respectively L(X,Y)) denotes the Banach space of all linear bounded operators mapping X into X (respectively, X into Y)

endowed with the norm $\|T\|=\sup_{x\in X}\frac{\|Tx\|}{\|x\|}$.

The domain, the image, the adjoint and the inverse operator of an operator A are denoted as D(A), ImA, A^* and A−1 respectively. Everywhere below A is a linear operator in X with domain D(A), generating a strongly continuous semigroup S(t), that is:

$$A=\lim_{h\to 0}\frac{S(h)-I}{h},$$

in the strong topology. $L_2([t, s], X)$ denotes the set of all strongly measurable L_2 integrable and X valued functions on [t, s]. Let $Q\in L(X,X^*)$ be a duality operator. We recall that the operator Q is positive definite in X if $\langle Qx, x\rangle \geq 0$ for arbitrary $x\in X$ and $\langle Qx, x\rangle > 0$ for $x \neq 0$.

We will denote by $LPD(X,X^*)$ and $LSPD(X,X^*)$ the set of all linear bounded positive definite and strongly positive definite operators mapping X into X^*, respectively. Also, we define:

- $L^p(R_+, R_+)$ is the set of functions positive and integrable with pth power on R_+ where $p \geq 1$ endowed with the norm $\|\phi\|_p=(\int_0^{+\infty}\phi^p)^{\frac{1}{p}}$ for $\phi \in L^p(R_+, R_+)$.
- $L^\infty(R_+, R_+)$ is the set of all measurable functions from R_+ to R_+ which are essentially bounded endowed with the norm
- $\|\phi\|_\infty=\sup_{t\in R}\phi(t)$ for $\phi \in L^\infty(R_+, R_+)$.
- $1_{[\vartheta,\zeta]}=\begin{cases}1, & \text{si } \vartheta \leq x \leq \zeta,\\ 0, & \text{elsewhere.}\end{cases}$

We consider the following system:

$$\begin{cases}\dot{x} = F(t, x, u), \quad t \geq t_0 \geq 0,\\ x(t_0) = x_0,\end{cases} \tag{2.1}$$

where $x \in X$ is the system state, $u \in U$ is the control input and $F: R+\times X \times U \to R+$ is a given function.

Definition 2.1. System (2.1) is practically stabilizable if there exists a continuous feedback control $u : X \to U$, such that system (2.1) with u(t) = u(x(t)) satisfies the following properties.

- For any initial condition $x_0 \in X$, there exists a unique mild solution $x(t, x_0)$ defined on R_+.
- There exist positive scalars ω, k, and r, such that the solution of the system (2.1) satisfies the following:

$$\|x(t)\| \leq k\|x_0\|e^{-\omega(t-t_0)} + r, \qquad \forall t \geq t_0 \geq 0.$$

When (i) and (ii) are satisfied, we say that Eq. (2.1) with u(t) = u(x(t)) is globally practically uniformly exponentially stable.

Definition 2.2. (Diesel and Uhl Jr, 1977). A Banach X^* has the Radon-Nikodym property if:

$$L_2([0,T],X^*)= (L_2([0, T], X))^*.$$

In the proof of the mains results, we shall use the following lemmas.

Lemma 2.1. (Nonlinear generalization of Gronwall's inequality, Zhoo, 2017).

Let θ be a non-negative function on R+, that satisfies the following integral inequality:

$$\theta(t) \leq \nu+\int_{t_0}^{t}(\chi(s)\theta(s) + \sigma(s)\theta^{\alpha}(s))ds, \ \nu \geq 0,$$

$0 \leq \alpha < 1, t \geq t_0$, where χ and σ are non-negative continuous functions. Then:

$$\theta(t) \leq [\nu^{1-\alpha}e^{(1-\alpha)\int_{t_0}^{t}\chi(s)ds} + (1-\alpha)\int_{t_0}^{t}\sigma(s)e^{(1-\alpha)\int_{s}^{t}\chi(r)dr}]^{\frac{1}{1-\alpha}}$$

Lemma 2.2. (Generalized Gronwall-Bellman Inequality, Dragomir, 2002).

Let $\lambda, \rho : R_+ \to R$ be continuous functions and $\phi : R_+ \to R_+$ is a function, such that:

$\dot{\phi}(t) \leq \lambda(t)\phi(t)+\rho(t)$, $\forall t \geq t_0$.

Then, we have the following inequality:

$$\phi(t) \leq \phi(t_0)e^{\int_{t_0}^{t}\lambda(v)dv}+\int_{t_0}^{t}e^{\int_{s}^{t}\lambda(v)dv}\rho(s)ds.$$

Lemma 2.3. Let $a,b \geq 0$ and $p \geq 1$. Then:

$$(a+b)^p \leq 2^{p-1}(a^p+b^p).$$

3. MAIN RESULTS

In this section, we shall state and prove our main results.

3.1 Practical stabilization of infinite-dimensional evolution equations

The purpose of this subsection is to establish the practical stabilization of evolution equations in Banach spaces. Based on the exact null-controllability in finite time of the nominal system whose origin is an equilibrium point, a stabilizing controller for the nonlinear system is then synthesized that guarantees the uniform exponential convergence to a neighborhood of the origin. This leads us to address the problem of practical stability of time-varying perturbed systems.

Consider infinite-dimensional evolution equations of the follwing form:

$$\begin{cases}\dot{x} = Ax + Bu + F(t, x),\\ x(t_0) = x_0,\end{cases} \tag{3.1}$$

where $x \in X$ is the system state, $u \in U$ is the control input, X is a Banach space, X^* has the Radon-Nikodym property and U is a Hilbert space. The operator $A:D(A)\subset X\to X$ is assumed to be the infinitesimal generator of the C_0-semigroup S(t) on X, $B\in L(U, X)$ and the function $F: R_+\times X \to R_+$ is continuous in t and locally Lipschitz continuous in x, that is for every $t_1 \geq 0$ and constant $c \geq 0$, there is a constant $M(c, t_1)$, such that:

$\|F(t,u)-F(t,v)\| \leq M(c, t_1)\|u-v\|$

holds for all $u, v\in X$, with $\|u\| \leq c$, $\|v\| \leq c$ and $t\in [0, t_1]$.

This system is seen as a perturbation of the nominal system:

$$\begin{cases}\dot{x} = Ax + Bu,\\ x(0) = x_0,\end{cases} \tag{3.2}$$

Next, we are interested in suitable feedback of the for the following:

$$u(t) = Dx(t), \tag{3.3}$$

where $D\in L(X, U)$.

Let $x(t,x_0,u)$ denote the state of a system (3.1) at moments $t \geq t_0 \geq 0$ associated with an initial condition $x_0 \in X$ at $t=t_0$ and input $u\in U$.

Now, we recall the definition of the generator of an exponentially stable semi-group as well as that of the exponential stability (Curtain and Zwart, 1995).

DOI 10.2478/ama-2021-0009

Definition 3.1. The operator A generates an exponentially stable semigroup S(t) if the initial value problem:

$$\dot{x}=Ax, \qquad t\geq 0, \quad x(0)=x_0 \tag{3.4}$$

has a unique solution $x(t)=S(t)x_0$ and $\|S(t)\| \leq Me^{-\alpha t}$ for all $t\geq 0$ with some positive numbers M and α.

Definition 3.2. The linear control system (3.4) is exponentially stable if there exist numbers $M> 0$ and $\alpha > 0$, such that:

$$\|x(t)\|\leq Me^{-\alpha t}\|x_0\|, \quad \forall\, t \geq 0.$$

Definition 3.3. The control system (3.2) is exactly null-controllable in finite time if for every $x_0 \in X$, there exist a number $T> 0$ and an admissible control $u(t) \in U = \{u(.) \in L_2([0,\infty), U)\}$, such that:

$$S(T)x_0 + \int_0^T S(T-s)Bu(s)ds = 0.$$

If we denote by C_T the set of null-controllable points in time T of system (3.2) defined by:

$$C_T = \left\{x_0 \in X; S(T)x_0 - \int_0^T S(T-s)Bu(s)ds;\ u(.) \in U\right\},$$

the system (3.2) is exactly null-controllable in time $T> 0$ if $C_T = X$.

If A is the generator of an analytic semigroup S(t) for $T > 0$, then we can define the operator $W_T \in L(U,X)$ by:

$$W_T=\int_0^T S^{-1}(s)Bu(s)ds, u(.) \in U,$$

and we have $C_T = \mathrm{Im}\, W_T$.

We state the following well-known controllability criterion for the infinite-dimensional control system presented in Curtain and Pritchard (1978) for reflexive Banach spaces and then in Xuejiao and Zhenchao (1999) for non-reflexive Banach spaces having the Radon-Nikodym property.

Proposition 3.1. (Curtain and Pritchard, 1978 and Xuejiao and Zhenchao, 1999). Let X, U be Banach and S(t) the C_0-semigroup of A. Assume that X^*, U^* has the Radon-Nikodym property. The following conditions are equivalent.

- Control system (3.2) is exactly null-controllable in time $T> 0$.
- There exists $c> 0$, $\|W_T^* x^*\| \geq c\|x^*\|, \forall\, x^* \in X^*$.
- There exists $c> 0$, $\|B^*S^*(s)x^*\|^2 \geq \|S^*(T)x^*\|$, $\forall\, x^* \in X^*$.
- If U is a Hilbert space, the operator $W_T = \int_0^T S^{-1}(s)BB^* S^{*-1}(s)ds$ is strongly positive definite.

The operator $P\in L(X,X^*)$ is called a solution of the Lyapunov equation if the following condition hold:

$$\langle PAx, x\rangle + \langle Px, Ax\rangle = -\langle Qx, x\rangle, \forall\, x \in D(A). \tag{3.5}$$

Note that, if A is bounded, then the above Eq. (3.5) has the standard form:

$$A^*Px + PAx = -Qx, \qquad \forall\, x \in X.$$

Remark 3.1. Datko (1970) showed that if A is exponentially stable in Hilbert space, then the Lyapunov equation has a solution.

We present the equivalence between the solvability of the Lyapunov equation and the exponential stability of the linear system (3.4) in the following Proposition 3.2.

Proposition 3.2. (Phat and Kiet, 2002) If for some $Q\in LSPD(X,X^*)$, $P\in LPD(X,X^*)$, the Lyapunov equation holds, then the operator A is exponentially stable. Conversely, if the generator A is exponentially stable, then for any $Q \in LSPD(X,X^*)$, there is a solution $P\in LPD(X,X^*)$ of the Lyapunov equation:

$$A^*P + PA = -Q. \tag{3.6}$$

Definition 3.4. The linear control system (3.2) is completely stabilisable if for every $\alpha > 0$, there exists a linear bounded operator $D:X\to U$ and a number $M> 0$, such that the solution satisfies the following condition:

$$\|x(t)\|\leq Me^{-\alpha t}\|x_0\|, \quad \forall\, t \geq 0.$$

Note that, if the operator D and number M do not depend on α, then the complete stabilizability implies exponential stabilizability in usual Lyapunov sense (Zabczyk, 1992). It is known from that if the linear control system (3.2), where X and U are Hilbert spaces is completely stabilizable then it is exactly null-controllable in finite time (Megan, 1975). Also, Phat and Kiet (2002) improved this result in Banach spaces.

Proposition 3.3. If the linear control system (3.2) is completely stabilisable then it is exactly null-controllable in finite time.

In the sequel, Phat and Kiet (2002) proved that the linear control system (3.2) is exponentially stabilizable by linear feedback $D:X\to U$, if it is null-controllable in finite time.

Proposition 3.4. If the linear control system (3.2) is exactly null-controllable in finite time, then it is exponentially stabilizable.

We define the Lie derivative of a function V(x) along solutions of (3.1) as:

$$\dot{V}(x) = \lim_{t\to 0^+} \sup \frac{1}{t}(V(x(t,x,u))-V(x)).$$

Now, we suppose the following assumptions.

(H1) The linear control system (3.2) is exactly null-controllable in finite time and there exists a constant operator $D:X\to U$, such that a sufficient condition specially related to operator is presented in Phat and Kiet (2002) as the following: for any $Q\in LSPD(X,X^*)$: $\langle Qx, x\rangle \geq b_1 \|x\|^2$, $\forall\, x \in X$, there exists $P\in LPD(X,X^*)$, $b_2\|x\|^2 \leq \langle Px, x\rangle \leq \|P\|\|x\|^2$, $\forall\, x \in X$, where $b_1, b_2 > 0$, which satisfies:

$$A_D{}^*P + PA_D = -Q. \tag{3.7}$$

(H2) The perturbation $F: R+\times X \to R+$ verifies the following estimation:

$$\|F(t,x)\| \leq \varphi(t)\|x\| + \mu(t) + \eta, \forall\, t \geq 0, \forall x \in X, \eta \geq 0,$$

where φ and μ are non-negative continuous functions with $\varphi \in L^1(R+, R+)$ and $\mu \in L^p(R+, R+)$ for some $p\in [1,+\infty)$.

Next, sufficient conditions are presented to guarantee the global existence and uniqueness of solutions of systems (3.1). Further, we investigate the practical stabilizability of the evolution equation using generalised Gronwall-Bellman inequality and Lyapunov theory.

Theorem 3.1. Under assumptions (H1) and (H2) the closed-loop system (3.1)-(3.3) have a unique solution, which is globally defined for all $t\geq t_0$ and this system is globally practically uniformly exponentially stable.

Proof. We break up the proof into two steps.

Step 1: Since F is locally Lipschitz continuous in x, uniformly in t, it follows from Pazy (1983) that for every initial condition the closed-loop equation possesses a unique mild solution on some interval $[t_0, t_0 + \delta]$ with $\delta > 0$. Indeed, integrating (3.1) , we obtain the following for $t\in[t_0, t_0 + \delta]$:

$x(t)=S(t-t_0)x_0+\int_{t_0}^{t} S(t-s)\big[Bu(s)+F\big(s,x(s)\big)\big]ds.$

Since $B\in L(U,X)$, then:

$$\|x(t)\| \le M_1\|x_0\| + M_1\Big(\int_{t_0}^{t} \|B\|\|D\|\|x(s)\| + M_2\|x(s)\| + M_3 + \eta ds\Big), \quad (3.8)$$

where: $M_1=\sup\{\|S(t-s)\|: 0\le t_0\le s\le t\le t+\delta\}$, $M_2=\sup_{t\in[t_{0,}t_0+\delta]}\|\varphi(t)\|$ and $M_3=\sup_{t\in[t_{0,}t_0+\delta]}\|\mu(t)\|$.

By applying Gronwall inequality (Tsinias, 1991, Lemma 2.7, p42) to inequality (3.8), any solution of this equation is uniformly bounded $\|x(t)\|\le M_1(\|x_0\|+M_3+\eta)$ on an arbitrary time interval $[t_0,t_0+\delta]$. Then, using Theorem 1.4 of Pazy (1983), we have $t_0+\delta=\infty$, and so we get global existence.

Step 2: Consider a Lyapunov function: $V(x)=\langle Px,x\rangle$. Let us compute the Lie derivative of V with respect to system (3.1) in a closed-loop with the controller (3.3). For $x\in D(A)$, we have $\dot V(x)=\langle P\dot x,x\rangle+\langle Px,\dot x\rangle$. From $\langle P(Ax),x\rangle=\langle Ax,Px\rangle$ and (3.7) with the help of Cauchy-Schawtz inequality, we obtain the following:

$$\begin{aligned}\dot V(x) &\le -\langle Qx,x\rangle + 2\|P\|\|F(t,x)\|x\| \\ &\le -b_1\|x\|^2 + 2\|P\|(\varphi(t)\|x\|+\mu(t)+\eta)\|x\| \\ &\le \Big(\frac{b_1}{\|P\|}+\frac{2\|P\|(\varphi(t)}{b_2}\Big)V(x)+\frac{2\|P\|}{\sqrt{b_2}}(\mu(t)+\eta)\sqrt{V(x)}\,.\end{aligned}$$

Let $z(x)=\sqrt{V(x)}$, which implies that:

$$\dot z(x)\le \Big(-\frac{b_1}{2\|P\|}+\frac{2\|P\|\varphi(t)}{b_2}\Big)z(x)+\frac{\|P\|}{\sqrt{b_2}}(\mu(t)+\eta). \quad (3.9)$$

These derivations hold for $x\in D(A)\subset X$. If $x\notin D(A)$, then the solution $x(t)\in D(A)$ and $t\to z(x(t))$ is a continuously differentiable function for all $t\ge t_0$ (for these properties of solutions, see Theorem 3.3.3 in Henry (1981)). Thus, by the mean value theorem we obtain that Eq.(3.9) holds for all $x\in X$. Using Lemma 2.2, we have for all $t\ge t_0$

$z(x)\le z(x_0)\exp\big(\frac{\|P\|M_\varphi}{b_2}\big)\exp\big(-\frac{b_1}{2\|P\|}(t-t_0)\big)+\exp\big(\frac{\|P\|M_\varphi}{b_2}\big)\int_{t_0}^{t}\frac{\|P\|}{\sqrt{b_2}}(\mu(s)+\eta)\exp\big(-\frac{b_1}{2\|P\|}(t-s)\big)ds$, where $M_\varphi=\int_0^\infty\varphi(s)ds$. We descriminate three cases:

1. If p=1, we get $\int_{t_0}^{t}(\mu(s)+\eta)\exp\big(-\frac{b_1}{2\|P\|}(t-s)\big)ds\le \|\mu\|_1+\frac{2\|P\|\eta}{b_1}$.

   Then, for all $t\ge t_0$, $\|x(t)\|\le\sqrt{\frac{\|P\|}{b_2}}\exp\big(\frac{\|P\|M_\varphi}{b_2}\big)\|x_0\|\exp\big(-\frac{b_1}{2\|P\|}(t-t_0)\big)+\frac{\|P\|}{b_2}\exp\big(\frac{\|P\|M_\varphi}{b_2}\big)\big(\|\mu\|_1+\frac{2\|P\|\eta}{b_1}\big)$.

2. If $p\in(1,+\infty)$ and $q>0$, such that $\frac{1}{P}+\frac{1}{q}=1$, we have by applying Hölder inequality $\int_{t_0}^{t}(\mu(s)+\eta)\exp\big(-\frac{b_1}{2\|P\|}(t-s)\big)ds\le\big(\frac{2\|P\|}{b_1q}\big)^{\frac{1}{q}}\|\mu\|_p+\frac{2\|P\|\eta}{b_1}$.

   Therefore, for all $t\ge t_0$, the solution x(t) verifies the estimation $\|x(t)\|\le\sqrt{\frac{\|P\|}{b_2}}\exp\big(\frac{\|P\|M_\varphi}{b_2}\big)\|x_0\|\exp\big(-\frac{b_1}{2\|P\|}(t-t_0)\big)+\frac{\|P\|}{b_2}\exp\big(\frac{\|P\|M_\varphi}{b_2}\big)\big(\big(\frac{2\|P\|}{b_1q}\big)^{\frac{1}{q}}\|\mu\|_p+\frac{2\|P\|\eta}{b_1}\big)$.

3. If p=+∞. Then, we have $\int_{t_0}^{t}\mu(s)\exp\big(-\frac{b_1}{2\|P\|}(t-s)\big)ds\le\frac{2\|P\|\eta}{b_1}\|\mu\|_\infty$.

   One can get, for all $t\ge t_0$ $\|x(t)\|\le\sqrt{\frac{\|P\|}{b_2}}\exp\big(\frac{\|P\|M_\varphi}{b_2}\big)\|x_0\|\exp\big(-\frac{b_1}{2\|P\|}(t-t_0)\big)+\frac{\|P\|}{b_2}\exp\big(\frac{\|P\|M_\varphi}{b_2}\big)\big(\frac{2\|P\|}{b_1}\|\mu\|_\infty+\frac{2\|P\|\eta}{b_1}\big)$.

We conclude that, the system (3.1) in closed-loop with the controller (3.3) is globally practically uniformly exponentially stable. This completes the proof. ■

As a consequence of Theorem 3.1, we have the following corollary.

Corollary 3.1. We consider the dynamical system (3.1). Assume that (H1) is fulfilled and there exists a continuous function $\mu: R+\to R+$ with $\mu\in L^p(R+,R+)$ for some $p\in[1,+\infty)$, such that $\|F(t,x)\|\le\mu(t),\ \forall\, t\ge 0,\forall x\in X$. Then, the system (3.1) in a closed-loop with the controller (3.3) is globally practically uniformly exponentially stable.

We can state other assumptions to obtain the global existence, uniqueness and the practical stabilizability for the evolution Eq. (3.1) under a restriction about the perturbed term bounded by the sum of Hölder continuous function and a Lipschitz function.

(H3) There exists a non-negative constant $0<\alpha<1$, such that the perturbation term $F: R+\times X\to R+$ satisfies the following condition: $\|F(t,x)\|\le\varphi(t)\|x\|^\alpha+\sigma(t)\|x\|, \forall\, t\ge 0,\forall x\in X$, where φ and μ are non-negative continuous functions with $\sigma\in L^1(R+,R+)$ and $\varphi\in L^p(R+,R+)$ for some $p\in[1,+\infty)$.

Then, one has the following theorem.

Theorem 3.2. If assumptions (H1) and (H3) are fulfilled, then the closed-loop system (3.1)-(3.3) have a unique solution, which is globally defined for all $t\ge t_0$ and this system is globally practically uniformly exponentially stable.

Proof. We break up the proof into two steps.

Step 1: Since F is locally Lipschitz continuous in x, uniformly in t, it follows from Pazy (1983) that for every initial condition the closed-loop equation possesses a unique mild solution on some interval $[t_0,t_0+\delta]$ with $\delta>0$. Indeed, integrating Eq.(3.1), we obtain the following for $t\in[t_0,t_0+\delta]$:

$x(t)=S(t-t_0)x_0+\int_{t_0}^{t} S(t-s)\big[Bu(s)+F\big(s,x(s)\big)\big]ds.$

Since $B\in L(U,X)$, then:

$$\|x(t)\| \le M_1\|x_0\| + M_1\Big(\int_{t_0}^{t} \|B\|\|D\|\|x(s)\| + M_2\|x(s)\|^\alpha + M_3\|x(s)\| ds\Big), \quad (3.10)$$

where: $M_1=\{\|S(t-s)\|: 0\le t_0\le s\le t\le t+\delta\}$, $M_2=\sup_{t\in[t_{0,}t_0+\delta]}\|\varphi(t)\|$ and $M_3=\sup_{t\in[t_{0,}t_0+\delta]}\|\sigma(t)\|$.

By applying Lemmas 2.1 and 2.3 to inequality (3.10), any solution of this equation is unifomly bounded: $\|x(t)\|\le 2^{\frac{\alpha}{1-\alpha}}e^{M_1\delta(\|B\|\|D\|+M_3)}\big(M_1\|x_0\|+\big(M_1M_2\delta(1-\alpha)\big)^{\frac{1}{1-\alpha}}\big)$, on an arbitrary time interval $[t_0,t_0+\delta]$. Applying Theorem 1.4 of Pazy (1983), we have $t_0+\delta=\infty$, and so we obtain global existence.

Step 2: Define the function $V:D(A)\to R+$ by $V(x)=\langle Px,x\rangle$. Then, the Lie derivative of V in t along the solution of the system (3.1) in a closed-loop system with the controller (3.3) leads to $V(x)=\langle P\dot x,x\rangle+\langle Px,\dot x\rangle\le-\langle Qx,x\rangle+2\|P\|\|F(t,x)\|x\|$. Using assumptions ($H_1$) and ($H_3$) we get the following estimation:

$$\dot V(x)\le\Big(-\frac{b_1}{\|P\|}+\frac{2\|P\|\sigma(t)}{b_2}\Big)V(x)+\frac{2\|P\|\varphi(t)}{\sqrt{b_2}^{\alpha+1}}V(x)^{\frac{\alpha+1}{2}}.$$

Let $\vartheta(x)=V(x)^{\frac{1-\alpha}{2}}$, which implies that:

$$\dot\vartheta(x)\le-\frac{(1-\alpha)}{2}\Big(\frac{b_1}{\|P\|}-\frac{2\|P\|\sigma(t)}{b_2}\Big)\vartheta(x)+\frac{\|P\|(1-\alpha)\varphi(t)}{\sqrt{b_2}^{\alpha+1}},$$

DOI 10.2478/ama-2021-0009

Using Lemma 2.2 , we get:

$$\vartheta(x) \le e^{\frac{\|P\|(1-\alpha)N_\sigma}{b_2}}(\vartheta(x_0)\exp(-\frac{b_1(1-\alpha)}{2\|P\|}(t-t_0)+\frac{\|P\|(1-\alpha)}{\sqrt{b_2}^{\alpha+1}}\int_{t_0}^{t}\exp\left(-\frac{b_1(1-\alpha)}{2\|P\|}(t-s)\right)\varphi(s)ds),$$

where $N_\sigma = \int_0^\infty \sigma(s)ds$. We discriminate three cases:

1. If p=1, we get:

$$\vartheta(x) \le e^{\frac{\|P\|(1-\alpha)N_\sigma}{b_2}}(\vartheta(x_0)\exp(-\frac{b_1(1-\alpha)}{2\|P\|}(t-t_0)+\frac{\|P\|(1-\alpha)}{\sqrt{b_2}^{\alpha+1}}\|\varphi\|_1).$$

From Lemma 2.3, it follows that:

$$\|x(t)\| \le 2^{\frac{\alpha}{1-\alpha}}e^{\frac{\|P\|N_\sigma}{b_2}}\left(\sqrt{\frac{\|P\|}{b_2}}\|x_0\|\exp\left(-\frac{b_1}{2\|P\|}(t-t_0)\right)+\frac{1}{\sqrt{b_2}}\left(\frac{\|P\|(1-\alpha)}{\sqrt{b_2}^{\alpha+1}}\|\varphi\|_1\right)^{\frac{1}{1-\alpha}}\right).$$

2. If p$\in(1,+\infty)$ and q>0, such that $\frac{1}{p}+\frac{1}{q}=1$, we have by applying / inequality:

$$\vartheta(x) \le e^{\frac{\|P\|(1-\alpha)N_\sigma}{b_2}}(\vartheta(x_0)\exp\left(-\frac{b_1(1-\alpha)}{2\|P\|}(t-t_0)\right)+\frac{\|P\|(1-\alpha)}{\sqrt{b_2}^{\alpha+1}}\|\varphi\|_p(\frac{2\|P\|}{q(1-\alpha)b_1})^{\frac{1}{q}}).$$

Then, using Lemma 2.3, we have:

$$\|x(t)\| \le 2^{\frac{\alpha}{1-\alpha}}e^{\frac{\|P\|N_\sigma}{b_2}}\sqrt{\frac{\|P\|}{b_2}}\|x_0\|\exp\left(-\frac{b_1}{2\|P\|}(t-t_0)\right)+\frac{2^{\frac{\alpha}{1-\alpha}}e^{\frac{\|P\|N_\sigma}{b_2}}}{\sqrt{b_2}}(\frac{\|P\|(1-\alpha)\|\varphi\|_p}{\sqrt{b_2}^{\alpha+1}})^{\frac{1}{1-\alpha}}\left(\frac{2\|P\|}{q(1-\alpha)b_1}\right)^{\frac{1}{q(1-\alpha)}}.$$

3. If p=+∞. Then, one has the following estimate:

$$\|x(t)\| \le 2^{\frac{\alpha}{1-\alpha}}e^{\frac{\|P\|N_\sigma}{b_2}}(\sqrt{\frac{\|P\|}{b_2}}\|x_0\|\exp\left(-\frac{b_1}{2\|P\|}(t-t_0)\right)+\frac{1}{\sqrt{b_2}}(\frac{2\|P\|^2}{b_1\sqrt{b_2}^{\alpha+1}}\|\varphi\|_\infty)^{\frac{1}{1-\alpha}}).$$

We deduce that, the system (3.1) in a closed-loop with the controller (3.3) is globally practically uniformly exponentially stable. This ends the proof. ■

For perturbed time-varying systems (3.1) in finite-dimensional spaces, we also have the following consequence.

Corollary 3.2. (Ellouze, 2019) Assume that $X=R^n$, $U=R^m$ and the assumptions (H1) and (H3) are satisfied, then the system (3.1) with the controller (3.3) is globally practically uniformly exponentially stable.

3.2 Feedback control of uncertain systems

Let X be a Banach space, X^* has the Radon-Nikodym property and U is a Hilbert space.

We consider the uncertain dynamical system:

$$\begin{cases}\dot{x} = Ax + Bu + G(t,x,u), \ t \ge t_0,\\ x(t_0) = x_0,\end{cases} \tag{3.11}$$

where x$\in$ X is the system state, u$\in$ U is the control input, A is the infinitesimal generator of the C_0-semigroup S(t) on a Banach space X, B$\in L(U,X)$ and G: R+$\times$ X $\times$ U $\to$ R+ is continuous in t and locally Lipschitz continuous in x uniformly in t on bounded intervals, that is, for every $t_1 \ge 0$ and constant c≥ 0, there is a constant M(c, t_1), such that for all x, y$\in$ X: $\|x\| \le c$, $\|y\| \le c$ and for all t$\in[0,t_1]$, u $\in$ U with $\|u\| \le c$ it holds that:

$$\|G(t,x,u) - G(t,y,u)\| \le M(c,t_1)\|x-y\|.$$

Let x(t,x_0,u) denote the state of a system (3.11) at moment t$\ge t_0$ associated with an initial condition $x_0 \in X$ at t=t_0 and input u$\in$ U.

We suppose the following assumption relating to system (3.11).

(H4) The perturbation term G: R+$\times$ X $\times$ U $\to$ R+ satisfies the following condition:

$$\exists a,b>0,\ \|G(t,x,u)\| \le a\|x\| + b\|u\| + d(t) + \varepsilon, \forall t \ge 0, \forall x \in X, \epsilon \ge 0. \tag{3.12}$$

where d is a non-negative continuous function with $d \in L^p(R+, R+)$ for some p$\in[1,+\infty)$.

The following lemma proved sufficient conditions for the global existence and uniqueness of solutions of system (3.11).

Lemma 3.1. Under assumption (H4), the closed-loop system (3.3)- (3.11) have a unique solution which is globally defined for all t$\ge t_0$.

Proof. As G is locally Lipschitz continuous in x, uniformly in t, it follows from Pazy (1983) that for every initial condition the closed-loop equation possesses a unique mild solution on some interval $[t_0, t_0+\delta]$ with $\delta > 0$. Indeed, integrating (3.11), we obtain the following for t$\in[t_0, t_0+\delta]$:

$$x(t)=S(t-t_0)x_0+\int_{t_0}^{t}S(t-s)[Bu(s)+G(s,x(s),u(s))]ds.$$

Since B$\in L(U,X)$, then by applying Gronwall inequality (Teschl, 2012, Lemma 2.7, p42), we have the following:

$$\|x(t)\| \le M_1(\|x_0\| + M_2\,\delta + \varepsilon)e^{M_1\delta(\|B\|\,\|D\|+a+b\|D\|)},$$

where: M_1= $\sup\{\|S(t-s)\|: 0 \le t_0 \le s \le t \le t+\delta\}$ and $M_2 = \sup_{t\in[t_0,t_0+\delta]}\|d(t)\|$ on an arbitrary time interval $[t_0, t_0+\delta]$. Now, Pazy (1983, Theorem 1.4) gives that and so we have global existence. The proof is completed. ■

The next theorem shows the practical stabilization of the system (3.11) using the Lyapunov indirect method and Gronwall-Bellman inequality.

Theorem 3.3. Assume that A is exponentially stable and the assumption (H4) is satisfied. Let P, Q$\in LPD(X,X^*)$ be the operators satisfying the Lyapunov Eq. (3.6) where $P=P^*$ and $\langle Qx,x\rangle \ge \lambda\|x\|^2$ for all x$\in$ X, $\lambda > 0$.Then, the nonlinear control system is practically stabilizable by the feedback control $u(t)=-\rho B^*Px(t)$ if:

$$\rho < \frac{\lambda - 2a\|P\|}{2b\|B\|\|P\|^2}. \quad (3.13)$$

Proof. Let $P \in LPD(X, X^*)$ be an operator which is a solution of the Lyapunov Eq. (3.6). Define the Lyapunov function $V:D(A) \to R+$ by $V(x)=\langle Px, x\rangle$. Noting that, there exists $\alpha > 0$ such that:

$$\alpha\|x\|^2 \le V(x) \le \|P\|\|x\|^2 .$$

Then, the derivative of V in t along the trajectories of system (3.11) and using the chosen feedback control and the Lyapunov equation is given as follows

$$\dot{V}(x)=\langle P\dot{x}, x\rangle + \langle Px, \dot{x}\rangle = -\langle Qx, x\rangle - \rho\langle PBB^*Px, x\rangle - \rho\langle Px, BB^*Px\rangle + \langle PG(t, x, u), x\rangle + \langle Px, G(t, x, u)\rangle.$$

Since P is self-adjoint, by assumption (H4) and condition (3.13), we have for all $t \ge t_0$:

$$\dot{V}(x) \le -kV(x) + \frac{2\|P\|}{\sqrt{\alpha}}(d(t) + \epsilon)\sqrt{V(x)},$$

where $k=\frac{\lambda - 2b\rho\|B\|\|P\|^2 - 2a\|P\|}{\|P\|} > 0$.

Let $\vartheta(x)=\sqrt{V(x)}$. Then, $\dot{\vartheta}(x) \le -\frac{k}{2}\vartheta(x) + \frac{\|P\|}{\sqrt{\alpha}}(d(t) + \varepsilon), \forall x \in X, \forall t \ge t_0$. Applying Lemma 2.2, we obtain the following:

$$\vartheta(x) \le \vartheta(x_0)e^{-\frac{k}{2}(t-t_0)} + \frac{\|P\|}{\sqrt{\alpha}}\int_{t_0}^{t} \exp\left(\frac{k}{2}(s-t)\right)(d(s) + \varepsilon)\, ds, \forall t \ge t_0.$$

We distinguish three cases:

1. If p=1, we get:

$$\|x(t)\| \le \sqrt{\frac{\|P\|}{\alpha}}\|x_0\|e^{-\frac{k}{2}(t-t_0)} + \frac{\|P\|}{\alpha}\left(\|d\|_1 + \frac{2\varepsilon}{k}\right), \forall t \ge t_0$$

2. If $p \in (1,+\infty)$ and $q > 0$, such that $\frac{1}{p} + \frac{1}{q} = 1$, we have by applying Hölder inequality:

$$\|x(t)\| \le \sqrt{\frac{\|P\|}{\alpha}}\|x_0\|e^{-\frac{k}{2}(t-t_0)} + \frac{\|P\|}{\alpha}\left(\left(\frac{2}{qk}\right)^{\frac{1}{q}}\|d\|_p + \frac{2\varepsilon}{k}\right), \forall t \ge t_0 .$$

3. 3. If $p=+\infty$. Then, we obtain the following:

$$\|x(t)\| \le \sqrt{\frac{\|P\|}{\alpha}}\|x_0\|e^{-\frac{k}{2}(t-t_0)} + \frac{2\|P\|}{\alpha k}\left(\|d\|_\infty + \frac{2\varepsilon}{k}\right), \forall t \ge t_0$$

We deduce that, the system (3.11) is practically stabilizable. This ends the proof. ■

In the following, we derive some sufficient conditions that guarantee practical stabilizability of system (3.11) in the case A is not exponentially stable and it is a generator of bounded C_0-semigroup, but the associated linear control system (3.2) is exactly null-controllable in finite time and the nonlinear perturbation satisfies a condition.

Theorem 3.4. Assume that the linear control system (3.2) is exactly null-controllable in finite time, then the system (3.11) is practically stabilizable for some appropriate numbers a, b satisfying the condition (3.12).

Proof. The linear control system is exactly null-controllable in finite time, then from Proposition 3.4 there is an operator $D \in L(X, U)$, such the operator $W_L=A+BD$ is exponentially stable. Let $P, Q \in LPD(X, X^*)$ be the operators satisfying the Lyapunov Eq. (3.6) where $P=P^*$ and $\langle Qx, x\rangle \ge \lambda\|x\|^2$ for all $x \in X$ and $\lambda > 0$. Consider the Lyaunov function $V(x)=\langle Px, x\rangle$. We have:

$$\alpha\|x\|^2 \le V(x) \le \|P\|\|x\|^2, \alpha > 0.$$

The Lie derivative of V along the trajectories of system (3.11) is given as follows:

$$\dot{V}(x) \le -\lambda\|x\|^2 + 2\langle PG(t, x, Dx), x\rangle \le -\eta\|x\|^2 + 2\|P\|(d(t) + \varepsilon),$$

where $\eta = \lambda - 2(a\|P\| + b\|D\|)$. We take a, b> 0, such that $\eta > 0$, that is, $a\|P\| + b\|D\| < \frac{\lambda}{2}$.

Let $\vartheta(x)=\sqrt{V(x)}$. Then:

$$\dot{\vartheta}(x) \le -\frac{\eta}{2\|P\|}\vartheta(x) + \frac{\|P\|}{\sqrt{\alpha}}(d(t) + \varepsilon), \forall x \in X, \forall t \ge t_0.$$

Using Lemma 2.2, we have:

$$\vartheta(x) \le \vartheta(x_0)e^{-\frac{\eta}{2\|P\|}(t-t_0)} + \frac{\|P\|}{\sqrt{\alpha}}\int_{t_0}^{t} \exp\left(\frac{\eta}{2\|P\|}(s-t)\right)(d(s) + \varepsilon)\, ds, \forall t \ge t_0.$$

We distinguish three cases:

1. If p=1, we have for all $t \ge t_0$:

$$\|x(t)\| \le \sqrt{\frac{\|P\|}{\alpha}}\|x_0\|e^{-\frac{\eta}{2\|P\|}(t-t_0)} + \frac{\|P\|}{\alpha}\left(\|d\|_1 + \frac{2\|P\|\varepsilon}{\eta}\right), \forall t \ge t_0 .$$

2. If $p \in (1,+\infty)$ and $q > 0$, such that $\frac{1}{p} + \frac{1}{q} = 1$, we obtain by applying Hölder inequality:

$$\|x(t)\| \le \sqrt{\frac{\|P\|}{\alpha}}\|x_0\|e^{-\frac{\eta}{2\|P\|}(t-t_0)} + \frac{\|P\|}{\alpha}\left(\left(\frac{2\|P\|}{q\eta}\right)^{\frac{1}{q}}\|d\|_p + \frac{2\|P\|\varepsilon}{\eta}\right), \forall t \ge t_0 .$$

3. If $p=+\infty$. Then, we have:

$$\|x(t)\| \le \sqrt{\frac{\|P\|}{\alpha}}\|x_0\|e^{-\frac{\eta}{2\|P\|}(t-t_0)} + \frac{2\|P\|^2}{\alpha\eta}(\|d\|_\infty + \varepsilon), \forall t \ge t_0 .$$

We deduce that, the system (3.11) is practically stabilizable. This finishes the proof. ■

Remark 3.2. The above results generalise theorems of stabilizability in Phat and Kiet (2002) with $d(t)=\varepsilon=0$.

4. EXAMPLES

In this section, we give some examples to illustrate the effectiveness of the results obtained in the present paper.

Example 4.1. We consider the controlled metal bar:

DOI 10.2478/ama-2021-0009

$$\begin{cases} \frac{\partial x(\zeta,t)}{\partial t} = \frac{\partial^2 x(\zeta,t)}{\partial^2 \zeta} + \mathbf{1}_{[\frac{1}{2},1]} u(t) + \frac{1}{1+t^2} x(\zeta,t) + \\ \qquad \frac{1+t}{(1+t^2)(1+\|x(\zeta,t)\|}, \\ \frac{\partial x}{\partial \zeta}(0,t) = 0 = \frac{\partial x}{\partial \zeta}(1,t),\ x(\zeta,0) = x_0(\zeta),\ t \geq 0, \end{cases} \quad (4.1.)$$

where $x(\zeta,t)$ represents the temperature at positionζ at time t and $x_0(\zeta)$ represents the initial temperature profile and u(t) represents the addition of heat along the bar. The two boundary conditions state that there is no heat flow at the boundary, and thus the bar is insulated. Let X=$L^2(0,1)$ and U=C. Equation (4.1) can be rewritten as (3.1), where A=$\frac{\partial^2 x(\zeta,t)}{\partial^2 \zeta}$ with D(A)={h∈ $L^2(0,1)$, h, $\frac{\partial h}{\partial \zeta}$ is absolutely continuous, $\frac{\partial^2 h}{\partial^2 \zeta} \in L^2(0,1)$ and $\frac{\partial h}{\partial \zeta}(0) = 0 = \frac{\partial h}{\partial \zeta}(1)\}$, B=$\mathbf{1}_{[\frac{1}{2},1]}$ and F(t,x)=$\frac{1}{1+t^2} x(\zeta,t) + \frac{1+t}{(1+t^2)(1+\|x(\zeta,t)\|}$.

A possesses an orthonormal basis of eigenvector $\varphi_0(\zeta) = 1$ and $\varphi_n(\zeta) = \sqrt{2}$ cos (n$\pi\zeta$), $n \geq 1$. Furthermore, the semigroup $(S(t))_{t\geq t_0}$ generated by A is given by:

S(t)x= $\sum_{n=0}^{\infty} e^{-n^2\pi^2 t} \langle x, \varphi_n \rangle \varphi_n$.

Using Proposition 3.1, it is easy to see that the nominal system of (4.1) is exactly null-controllable in finite time. Moreover, the assumption (H2) is satisfied with η=0 and $\varphi(t) = \frac{1}{1+t^2}$ and $\mu(t) = \frac{1+t}{1+t^2}$ are non-negative functions with $\varphi \in L^1(R+,R+)$ and $\mu \in L^p(R+,R+)$ for some p∈ $[1,+\infty)$. Then, all hypotheses of Theorem 3.1 are satisfied and the controlled heat Eq. (4.1) is practically stabilizable.

Example 4.2. We consider the controlled perturbed heat equation:

$$\begin{cases} \frac{\partial x(\zeta,t)}{\partial t} = \frac{\partial^2 x(\zeta,t)}{\partial^2 \zeta} + \frac{2+t^2}{1+t^2} u(t) + x(\zeta,t) + e^{-t}\mathbf{1}_{[0,\frac{\pi}{2}]} \\ x(0,t) = 0 = x(\pi,t),\ x(\zeta,0) = x_0(\zeta),\ t \geq 0, \end{cases} \quad (4.2)$$

where $x(\zeta,t)$ represents the temperature at position $\zeta \in [0,\pi]$ time t and $x_0(\zeta)$ represents the initial temperature profile.
Let X=$L^2(0,\pi)$ and U=C. It is useful to formulate the equation (4.2) as an abstract differential equation of the form (3.11), where A=$\frac{\partial^2 x(\zeta,t)}{\partial^2 \zeta}$ with D(A) ={ $h \in L^2(0,\pi), \frac{\partial h}{\partial \zeta}$ is absolutely continuous $\frac{\partial^2 h}{\partial^2 \zeta} \in L^2(0,\pi)$ and $h(0) = 0 = h(\pi)\}$, B=I and G(t, x(ζ, t)u)=x(ζ, t) + $\frac{1}{1+t^2}$u(t)+ $e^{-t}\mathbf{1}_{[0,\frac{\pi}{2}]}$.

A possesses an orthonormal basis of eigenvector $\varphi_n(\zeta) = \sqrt{\frac{2}{\pi}}\sin(n\zeta)$, n≥ 0. Furthermore, the semigroup $(S(t))_{t\geq t_0}$ generated by A is given by:

S(t)=$\sum_{n=1}^{\infty} e^{-n^2 t} \langle x, \varphi_n \rangle \varphi_n$.

Obviously, S(t) is exponentially stable. Therefore, A is exponentially stable. Moreover, G satisfies the assumption (H4), just take a=1, b=1, ε = 0 and d (t) =$\frac{\pi}{2} e^{-t}$, is a non-negative continuous function, with d∈ $L^p(R+,R+)$ for some p∈ $[1,+\infty)$. Consequently, by applying Theorem 3.3, the controlled heat Eq. (4.2) is practically stabilizable.

5. CONCLUSION

Practical stabilization of infinite-dimensional evolution equations in Banach spaces has been investigated. Moreover, sufficient conditions have been derived to guarantee the practical stabilization of a class of uncertain systems in Banach spaces. Illustrative examples are given to indicate significant improvements and the application of the results.

REFERENCES

1. **Chen P.** (2021), Periodic solutions to non-autonomous evolution equations with multi-delays, *Discrete and Continuous Dynamical Systems,* 26(6), 2921–2939.
2. **Chen P., Zhang X., Li Y.** (2020a), Cauchy problem for fractional non-autonomous evolution equations, *Banach Journal of Mathematical Analysis,* 14(2), 559–584.
3. **Chen P., Zhang X., Li Y.** (2020b), Existence approximate controllability of fractional evolution equations with nonlocal conditions via resolvent operators, *Fractional Calculus Applied Analysis,* 23(1), 268–291.
4. **Chen P., Zhang X., Li Y.** (2020c), Approximate Controllability of Non-autonomous Evolution System with Nonlocal Conditions, *Journal of Dynamical Control Systems,* 26(1), 1–16.
5. **Chen P., Zhang X., Li Y.** (2021), Cauchy problem for stochastic non-autonomous evolution equations governed by noncompact evolution families, *Discrete and Continuous Dynamical Systems,* 26(3), 1531–1547.
6. **Curtain R.F., Pritchard A.J.** (1978), *Infinite Dimensional Linear Systems Theory*, Lecture Notes in Control Information Sciences, Springer Verlag, Berlin.
7. **Curtain R.F., Zwart H.J.** (1995), *An Introduction to Infinite Dimensional Linear Systems Theory*, Lecture Notes in Control Information Sciences, Springer Verlag, New York.
8. **Damak H.** (2020), Asymptotic stability of a perturbed abstract differential equations in Banach spaces, *Operators matrices,* 14, 129–138.
9. **Damak H.** (2021), Input-to-state stabilty integral input-to-state stability of non-autonomous infinite-dimensional systems, *International Journal of Systems Sciences.* https://doi.org/10.1080/00207721.2021.1879306.
10. **Damak H., Ellouze I., Hammami M.A.** (2013), A separation principle of a class of time-varying nonlinear systems, *Nonlinear Dynamics Systems Theory,* 13, 133–143.
11. **Damak H., Hammami M.A.** (2016), Stabilization Practical Asymptotic Stability of Abstract Differential Equations, *Numerical Functional Analysis Optimization,* 37, 1235–1247.
12. **Datko R.** (1970), Extending a theorem of A.M. Lyapunov to Hilbert spaces, *Journal of Mathematical Analysis Applications,* 32, 610–616.
13. **Diesel J., Uhl Jr. J.J** (1977), Vector Measures, Mathematical surveys, American Mathematical Society , Rhode Isl.
14. **Dragomir S.S.** (2002), Some Gronwall Type Inequalities Applications, School of Communications Informatics, Victoria University of Technology.
15. **Ellouze I.** (2019), On the practical separation principle of time-varying perturbed systems, *IMA Journal of Mathematical Control Information,* 00, 1–16.
16. **Henry D.** (1981), *Geometric Theory of Semilinear Parabolic Equations of Lecture Notes in Mathematics*, Springer Verlag, Berlin.
17. **Ikeda M., Maed H., Kodama S.** (1972), Stabilization of linear systems, *SIAM Journal on Control,* 10, 716–729.
18. **Kalman R.E., Ho Y.C., Narenda K.S.** (1963), Controllability of Linear Dynamical Systems, *Differential Equations,* 1, 189–213.

19. **Kobayashi T.** (1989), Feedback stabilization of parabolic distributed parameter systems by discrete-time input-output data, *SIAM Journal on Control Optimization,* 22, 509–522.
20. **Lakshmikantham V., Leela S., Martynuk A.A.** (1998), *Practical Stability of Nonlinear Systems*, World Scientific, Singapore.
21. **Megan G.** (1975), *On the stabilizability Controllability of Linear Dissipative Systems in Hilbert spaces*, 32 S.E.F, Universitate din Timisoara.
22. **Pazy A.** (1983), *Semigroups of Linear Operators Applications to Partial Differential Equations*, Springer, New York.
23. **Phat V.N.** (2001), Stabilization of linear continuous time-varying systems with state delays in Hilbert spaces, *Electronic Journal of Differential Equations,* 2001, 1–13.
24. **Phat V.N.** (2002), New Stabilization criteria for linear time-varying systems with state delays norm-bounded uncertainties, *in IEEE Transactions on Automatic Control,* 12, 2095–2098.
25. **Phat V.N., Ha Q.P.** (2008), New characterization of stabilizability via Riccati equations for LTV systems, *IMA Journal of Mathematical Control Information,* 25, 419–429.
26. **Phat V.N., Kiet T.T.** (2002), On the Lyapunov equation in Banach spaces applications to control problems, *International Journal of Mathematics Mathematical Sciences,* 29, 155–166.
27. **Teschl G.** (2012), *Ordinary Differential Equations Dynamicals Systems, Graduate studies in mathematics*, American Mathematical Society.
28. **Tsinias J.** (1991), Existence of control Lyapunov functions its applications to state feedback stabilizability of nonlinear systems , *SIAM Journal on Control Optimization,* 29, 457–473
29. **Wonham W.M.** (1967), On Pole assignment in Multi-Input Controlable Linear Systems, *IEEE Transactions on Automatic Control,* 12(6), 660–665.
30. **Xuejiao H., Zhenchao C.** (1999), Controllability of linear systems in non-reflexive Banach spaces, *Northeastern Mathematical Journal,* 15, 459–464.
31. **Zabczyk J.** (1992), *Mathematical Control Theory:An introduction*, Birkhauser.
32. **Zhoo B.** (2017), Stability analysis of nonlinear time-varying systems by Lyapunov functions with indefinite derivatives, *IET Control Theory Applications,* 11, 1434–1442.

Acknowledgement: The author would like to thank the anonymous reviewers for valuable comments to improve the paper.

DOI 10.2478/ama-2021-0010

COMPARATIVE STUDY OF THE PARALLEL AND ANGULAR ELECTRICAL GRIPPER FOR INDUSTRIAL APPLICATIONS

Mohammad Javad FOTUHI[*], Zafer BINGUL[**]

[*]Research and Development, Keramik Makina Sanayi ve Ticaret A.S,
Güzeller Organize Sanayi Bölgesi İnönü Mah. Nursultan Nazarbayev Sok. No:21 41400 Gebze, Kocaeli, Turkey
[**]Automation and Robotics Lab, Department of Mechatronics Engineering, Kocaeli University,
Kabaoğlu, Baki Komsuoğlu bulvarı No:515, Umuttepe, 41001 İzmit/Kocaeli, Turkey

mohammad.fotuhi@keramik.com.tr, zaferb@kocaeli.edu.tr

received 22 October 2020, revised 25 May 2021, accepted 31 May 2021

Abstract: The aim of this paper is to study the position and power performances of an electrical lead screw-driven industrial gripper mechanism (LSDIGM). This work consists of designing and developing an electrical LSDIGM that has the potential to meet various demands in the automation industry and factories. The performances of both angular electrical gripper (AEG) and parallel electrical gripper (PEG) mechanisms were compared based on their position and power efficiency. The position efficiency of these electrical LSDIGM is computed from the position root mean square error (PRMSE) obtained from errors between the two measured positions (input incremental encoder and output linear encoder). In the experimental setup, a current sensor and a spring were employed to measure the current in the input of the system and the stiffness in the output of the system, respectively. The electrical power in the input of the electrical LSDIGM and the mechanical power in the output of the LSDIGMs were calculated using the current and the spring force, respectively. Finally, the power efficiency of these electrical LSDIGMs was examined and compared at different velocity circumstances.

Key words: Electrical lead screw-driven industrial gripper mechanism (LSDIGM), Efficiency, Position root mean square error (PRMSE), Parallel electrical gripper (PEG), Angular electrical gripper (AEG)

1. INTRODUCTION

Nowadays, designing and developing an inexpensive and reliable electric gripper mechanism in factories is very important in the robotic manufacturing revolution. In robotic systems, the gripper is like the human hand that allows one to grab and place any particular object. Grippers have been used in factories to facilitate various operations and for tasks that are dangerous and difficult for humans to perform, such as logistics, underwater welding, material handling, sensitive surgery, detecting and defusing bombs, and industrial furnaces (Birglen and Schlicht, 2018). The basic requirements of the gripper system design should be characterized as follows: high power/weight ratio giving the lowest machine mass, high torque/inertia ratio giving the best acceleration possible, the smooth trajectory of torque particularly at low speeds to minimize speed variation and achieve good positional accuracy, controlled torque at zero-speed, high maximum speed of operation, high efficiency and power factor to minimize drive requirement, compact integrated design with the application, good frequency response, low backlash, and low cost (Liu et al, 2020). To develop an industry interesting product, there is a need for inexpensive, simple, and robust solutions. Industrial robotic grippers have an effective role in modern automation as they constitute the end-of-arm of robotic manipulators and then, they are in direct contact with the work piece (Honarpardaz et al, 2017; Lu et al., 2019). Also, with the development of series elastic actuators and control methods, flexible grippers can be developed; flexible grippers have more accuracy of control and gripping force (Li et al., 2017). With the advent of modeling and simulation technology, design and development studies are increasingly focusing on robotics research. The key challenge in these problems is to find the right balance between all the conflicting goals. The perfect solution to an optimal design problem of a given gripper system is to develop a set of solutions by analyzing the system parameters that accomplish all the goals simultaneously (Kuang et al., 2017; Hu et al, 2019).

In a variety of industrial applications, hydraulic and pneumatic grippers are used to create a holding force according to specific specifications, depending on the load. However, hydraulic and pneumatic methods are not flexible and cannot be used in the manufacture of modern systems (Kumar et al., 2017). Today, a mechanical gripper in the system and mechatronics engineering are increasingly being replaced by electrically controlled drives called the electrical actuator (Tai et al., 2016). The electrical gripper is a mechanism used to perform linear motion electrically similar to that achieved with hydraulic and pneumatic grippers. In the main component of the electrical gripper, the classical mechanical gripper is replaced with an electrical motor and reprogrammable controller. Compared to the mechanical grippers, the electrical gripper improves accuracy and repeatability (Shin et al., 2012). The servomotors used in modern electrical grippers are well suited for complex motions because they are easy to control by changing the voltage and current, speed, and torque in the servomotors. However, motion systems using the feedback feature in these motors are expensive and quite complex. This is one of the main reasons why a stepper motor is used as an actuator

in a proposed electronic gripper system while considering the low price and easy usage (Datta et al., 2015). A stepper motor is a motor that converts digital electric pulses into stepping mechanical movements. The most important advantage of a stepper motor is its use in an accurately open-loop control system. This type of control eliminates the need for expensive detection and feedback devices such as sensitive encoders. Its position is simply determined by tracking the input electrical pulses (Shaw and Dubey, 2016). The stepper motor can be a good selection for open-loop motion control. Stepper motors can be used in projects where rotation angle, speed, position, and synchronization must be controlled. Stepper motors can be used in many different projects (Su and Zhong, 2018). Because of these main advantages, a stepper motor is selected as an actuator for electromechanical gripper movement output in this paper. In this paper, the application of the lead screw-driven industrial gripper mechanism (LSDIGM) was developed from the switching of the existing pneumatic cylinder. The main goal of such a system is to avoid force overshoots in the contact stage while keeping stress force error in the high-sensitive tracking stage, where traditional pneumatic cylinders are not competent. The proposed method of the ratio of the maximum force (RMF) has been used to prove the appropriate force rate. In this study, the lead screw and electrical motor-driven industrial gripper mechanism model was developed to have a flexible and reprogrammable system. First, the design and modeling of electrical LSDIGM are briefly introduced. Then, the overall behavior structure of the system is proposed. The position and power efficiency of these electrical LSDIGMs were examined and compared at different velocity circumstances.

2. MATERIALS AND METHODS

In the case of rotational actuators, first, the movement forms have to be converted from rotational to linear movement. This can be achieved by a connecting lead screw to the actuator and a linear guide the diagram of the electrical LSDIGM is illustrated in Fig.1. For the electrical gripper, a model was developed in Li et al. (2011) and Chen et al. (2014). The mathematical model is based on two movements: the movement angle, θ, to the motor angle and the movement distance to the load movement. The θ angle is linked by a lead-screw mechanism to the *d* distance. The resultant angular motion and linear motion produce two respective forces: a lead-screw torsional torque τ_{ls} applied at the input of the system and a gripper linear force F_g applied at the output of the system.

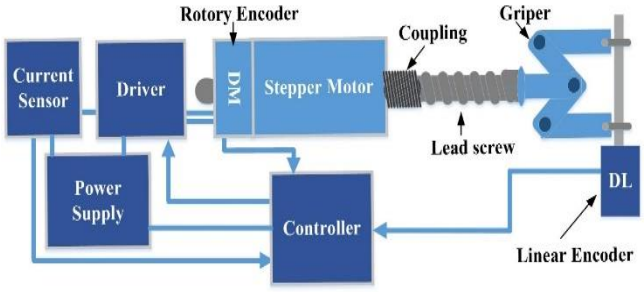

Fig. 1. Block diagram of the LSDIGM

In order to evaluate the performance of position errors, in general, the square root of the mean of all square errors (PRMSE) is calculated between the stepper motor position and the measured load signal based on equation 1 (Chen et al., 2014; Nanda, 2010). The equations (2, 3, 4, 5) are used to illustrate the effect of time and position error in equation 1.

$$\mathrm{PRMSE} = \sqrt{\frac{1}{N}\sum_{i=1}^{N}(p_i - \hat{p}_i)^2} \quad (1)$$

Integral of the absolute value of the error (IAE):

$$\mathrm{IAE} = \sum_{i=1}^{N}|(p_i - \hat{p}_i)| \quad (2)$$

Integral of the square value of the error (ISE):

$$\mathrm{ISE} = \sum_{i=1}^{N}(p_i - \hat{p}_i)^2 \quad (3)$$

Integral of the time-weighted absolute value of the error (ITAE):

$$\mathrm{ITAE} = \sum_{i=1}^{N} t|(p_i - \hat{p}_i)| \quad (4)$$

Integral of the time-weighted square value of the error (ITSE):

$$\mathrm{ITSE} = \sum_{i=1}^{N} t(p_i - \hat{p}_i)^2 \quad (5)$$

where p_i is the output position, $\hat{p}_i$ is the input position, *t* is the sampling time, and *N* is the sampling number (Najjari et al., 2014).

In this paper, a standard algorithm using a C++ programming language is implemented in a Googoltech industrial PC to run the LSDIGM system. The stepper motor can be programmed and controlled in real-time by using this software via the output port of an industrial PC. In order to perform the gripper movement, the proposed method uses a lead screw for converting the rotary movement of the stepper motor into the linear movement.

2.1. Mechanical Design

To obtain a simple and inexpensive design, we minimized the amount of mechanical and electronic parts (Fig. 2). It was, therefore, decided to use a normal stepper motor and lead screw. Also, angular gripper and parallel gripper can be both opened and closed by only one HANPOSE 17HS3401S T8x8 Nema stepper motor with a PK6M05N lead screw driven by the stepper motor driver model CWD556 (Fig. 3). When a voltage of 24 V is applied to the motor, this results in a constant actuation torque of 0.5 Nm applied at the base of the finger and 0.25 Nm on each of the opposite fingers as defined (Park et al., 2016). First, it is required to determine the torque of the motor relative to the system's output force, the torque due to the force the load applies to the gripper finger called gripper force F_g(N), and it is introduced through function F_g. The gripper force is given in equation (6) as mentioned before; for rotational actuators, the movement has to be converted from rotational to linear. To calculate the velocity of the motor, the linear speed of the gripper finger can be converted to rotational speed using equation (7).

$$F_g = \frac{2\pi\,\eta\,\tau_{ls}}{\ell} \quad (6)$$

$$v = \frac{\ell\omega}{2\pi} \quad (7)$$

where F_g is the force/load applied (N), η is the efficiency factor, ω is the rotational speed (rad/sec), and *v* is the linear speed (mm/sec) (Liu et al., 2016). Torque τ_{ls} is the lead-screw acting on the shaft caused by forces (see Fig. 4). It can be based on the following equations (8):

DOI 10.2478/ama-2021-0010

$$\tau_{ls} = \frac{F_a D_x}{2}\left(\frac{\ell+\mu\pi D_x}{\pi D_x-\mu L}\right)\left(\frac{1}{\eta}\right) \quad (8)$$

where:

$$D_x = D_p - \left(\frac{P_B}{2}\right) \ , \quad \ell = n_s P_B \quad (9)$$

F_a is the moving force in the direction of the lead screw, and θ is the tilt angle (Xu et al., 2018; Hassan and Abomoharam, 2017). The parameters of the lead-screw model are given in Table 1.

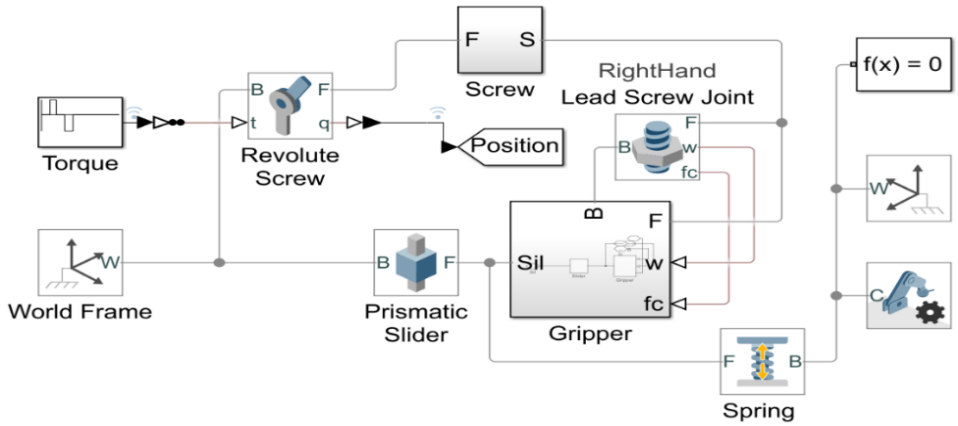

Fig. 2. Simscape model of the electrical LSDIGM actuator

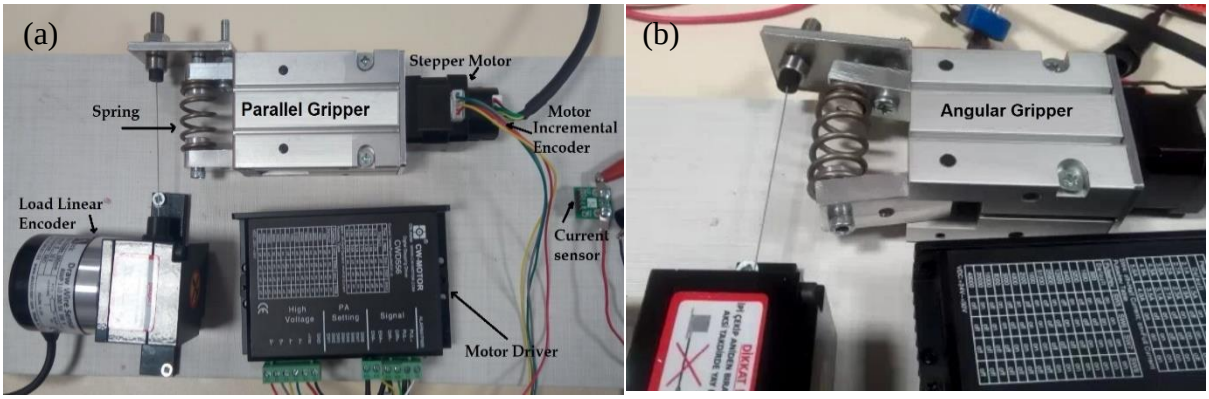

Fig. 3. Experimental setup of LSDIGM (a) parallel gripper and (b) angular gripper

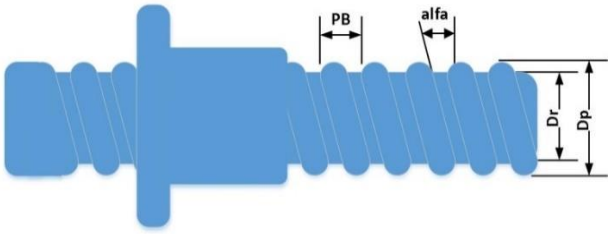

Fig. 4. Model of the lead screw

Tab. 1. Parameters of lead-screw model-PK6M05N

Parameter	Symbol	Value
Pitch circle diameter	D_p	9.5 mm
Screw pitch	P_B	5 mm
Lead of the thread	ℓ	5 mm
The starts number	n_s	1
Friction coefficient of sliding surface	μ	0.15
Thread angle	A	30 degree

2.2. Modeling of Electromechanical System

To analyze the dynamic characteristics after the completion of the development of the electromechanical system, an electrical LSDIGM actuator model was created in SIMULINK™ (Fig. 2).

Contributions from the different system variables were combined to simplify the model. The motor rotor inertia, screw nut inertia, and carrier inertia were combined, along with the referred inertial contribution from the linear motion parts and were represented by equation (10).

$$J_{tot} = J_{motor} + J_{nut} + J_{carrier} + m\left(\frac{L}{2\pi}\right)^2 \quad (10)$$

where *m* is the mass of the linear components, and ℓ is the screw lead. This leads to

$$J_{tot}\alpha = \tau_{motor} - (\tau_{load} + \tau_{viscous} + \tau_{Coulomb}) \quad (11)$$

$$J_{tot}\frac{d^2\theta}{dt^2} = \tau_{motor} - \left(F_g X + \beta\frac{d\theta}{dt} - F_c\frac{\frac{d\theta}{dt}}{\left|\frac{d\theta}{dt}\right|}\right) \quad (12)$$

where F_g is the force on the gripper fingers, *j* represents the gear ratio and linear conversion, β represents the viscous damping coefficient, and *Fc* represents the Coulomb force component.

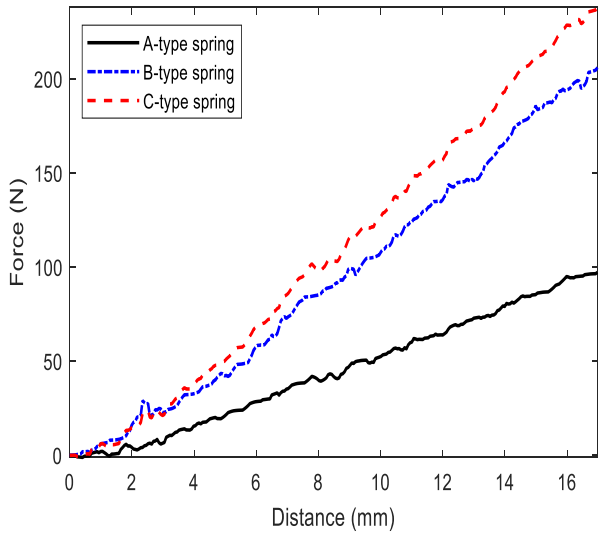

Fig. 5. Force–distance (stiffness) characteristic of the springs given in Table 3

3. RESULTS AND DISCUSSION

There are several methods for analyzing and measuring force, three springs with different stiffness coefficient values (Fig. 5 and Table 3) have been used to analyze the dynamic behavior of the system (Fotuhi et al., 2020). To analyze the gripper, two sensors were used to measure data. Sensors are incremental encoders of motor and linear encoders of load (Fotuhi and Bingul, 2021; Wang et al., 2016). Motor incremental encoder gives a pulse output of 0.17578125 (degrees/pulse), and load linear encoder gives a voltage output of 0.5 (mV/mm). Over the range 0–20 mm, this is amplified by an amplifier with a voltage gain of 20, sampled, and applied to a 10-bit analog-to-digital converter with voltage range 0–5 V. The resolution of the measurement is 1024 (digital value/mm). The experimental setup of electrical LSDIGM is shown in Fig. 3. The position and current analog signals are converted to physical parameters by using sensor gains (equations 13, 14, and 15). They are given in Table 2.

$$\mathrm{D_L(mm)} = (\mathrm{V_L} - \mathrm{o_v}) * (\mathrm{c_V}) \tag{13}$$

$$\mathrm{D_M(mm)} = (\mathrm{P_M} - \mathrm{o_p}) * (\mathrm{c_P}^{-1}) \tag{14}$$

$$\mathrm{C_s(Amper)} = (\mathrm{V_c} - \mathrm{o_c}) * (\mathrm{c_c}^{-1}) \tag{15}$$

here, D_L is the distance of load (mm), D_M is the distance of linear movement of motor (mm), $C_s$is the equation of current sensing, V_L is the digitized voltage from analog to digital using an ADC (analog-to-digital converter) value of voltage output of the load linear encoder (digital value), P_M is the pulse number of the motor incremental encoder (pulse), and V_c is the discrete voltage (ADC value of voltage) output of the current sensor.

Tab. 2. Position and current sensor gains

Parameter	Symbol	Value
Voltage coefficient of the linear encoder	c_V	1.427428571
Pulse coefficient of the incremental encoder	c_P	1.0058
Current coefficient of the current sensor	c_c	29.457
Offset of voltage	o_v	779.7638571
Offset of pulse	o_p	62.41924891
Offset of current	o_c	17.92554531

Tab. 3. Technical specification of springs

Spring type	Stiffness (*Ks* = N/mm)	Free length (mm)	Full compression (mm)	Total coil
A	5.735	42.1	25.3	7
B	11.764	42.5	25.2	7
C	13.823	42.2	25.6	7

Tab. 4. Velocity profile (maximum speed = 30 mm/sec)

Speed mode	Speed	Speed (mm/sec)
Low speed (LS)	5% Max	1.5
Medium speed (MS)	20% Max	6
High speed (HS)	65% Max	19.5
Very high speed (VHS)	85% Max	25.5

To avoid repetition of showing the same behavior in the paper, the movement profile of a parallel and angular gripper A-type of the spring in the low-speed case is only illustrated in Fig. 6. The results of the medium, high, and very high speed of B-type and C-type of springs for parallel and angular gripper are given also in Tables 5 and 6. The velocity profile is shown in Table 4.

According to Table 5, for the A-type spring, the maximal force of 106.4 N and the maximum linear movement of 18.55 mm are obtained by the high velocity of 5.892 mm/sec. For the B-type spring, the maximal force of 100 N and the maximum linear movement of 9 mm are obtained by the high velocity of 1.375 mm/sec. For the C-type spring, the maximal force of 105 N and the maximum linear movement of 8.013 mm are obtained by the high velocity of 1.375 mm/sec. According to Table 6, for the A-type spring, the maximal force of 65.36 N and the maximum linear movement of 11.55 mm are obtained by the high velocity of 1.378 mm/sec. For the B-type spring, the maximal force of 84.86 N and the maximum linear movement of 6.966 mm are obtained by the high velocity of 1.375 mm/sec. For the C-type spring, the maximal force of 103.7 N and the maximum linear movement of 7.504 mm are obtained by the high velocity of 1.371 mm/sec.

According to Table 7, equations (2, 3, 4, and 5) are used to illustrate the effect of time and position error in equation (1).

DOI 10.2478/ama-2021-0010

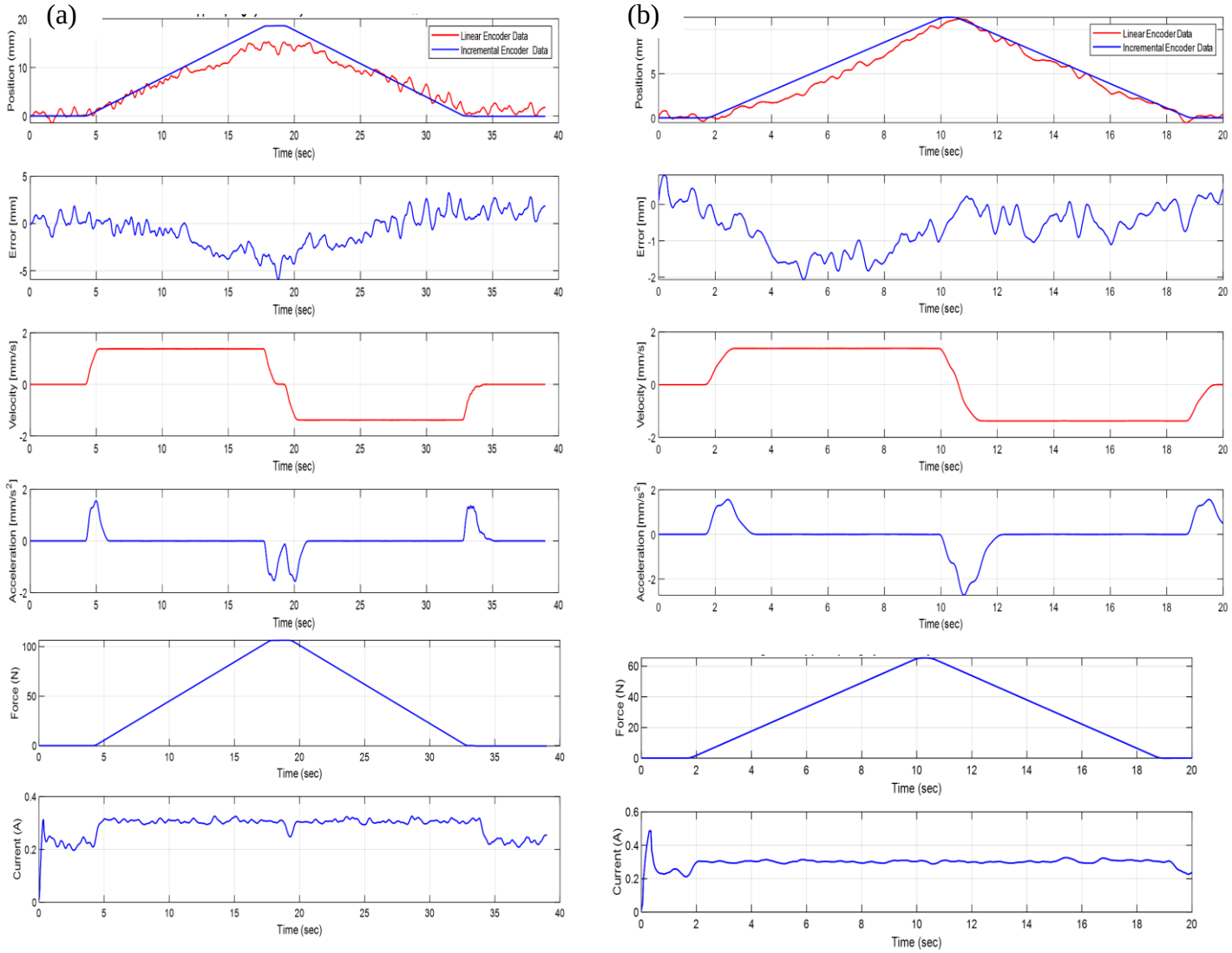

Fig. 6. The motion profile of a (a) parallel gripper and (b) angular gripper A-type spring in the LS mode

Tab. 5. Parallel gripper and spring motion analysis

Spring type	*Speed mode*	*Maximum linear movement (mm)*	*Maximum force (N)*	*Time (sec)*	*Maximum current (A)*	*Maximum velocity (mm/sec)*	*Maximum acceleration (mm/sec²)*
A	LS	18.54	106.4	28.869	0.3155	1.376	1.547
	MS	18.51	106.3	8.79	0.3150	5.892	6.598
	HS	17.26	103.73	3.735	0.3399	18.88	22.24
	VHS	6.085	34.9	4.26	0.3106	9.991	19.75
B	LS	9.09	106	13.49	0.7168	1.375	1.523
	MS	8.934	105.1	9.675	0.3161	5.889	6.336
	HS	8.934	105.1	4.59	0.3228	12.34	18.22
	VHS	2.827	33.26	6.21	0.3088	5.179	9.689
C	LS	8.013	105	14.45	0.3129	1.376	1.553
	MS	8.0	104	7.755	0.3045	5.887	6.667
	HS	7.864	101.1	3.38	0.3203	11.12	17.82
	VHS	1.935	25.39	69.08	0.2786	3.25	4.675

Tab. 6. Angular gripper and spring motion analysis

Spring type	Speed mode	Maximum linear movement (mm)	Maximum force (N)	Time (sec)	Maximum current (A)	Maximum velocity (mm/sec)	Maximum acceleration (mm/sec²)
A	LS	11.4	65.36	17.525	0.4862	1.378	1.561
	MS	11.4	65.36	8.04	0.3203	5.887	6.682
	HS	7.28	55.1	4.275	0.3176	11.74	17.94
	VHS	5.047	28.94	2.565	0.2941	8.848	16.75
B	LS	6.966	84.86	14.355	0.3765	1.375	1.528
	MS	6.611	79.27	3.51	0.3105	5.883	7.712
	HS	6.362	74.84	2.37	0.322	9.028	15.96
	VHS	4.137	48.67	44.087	0.3099	13.24	53.43
C	LS	7.504	103.7	20.7	0.3033	1.371	1.495
	MS	7.144	101.7	5.13	0.3094	5.886	6.586
	HS	6.847	98.21	3.386	0.3081	10.763	17.16
	VHS	3.714	51.32	2.40	0.3071	6.264	11.45

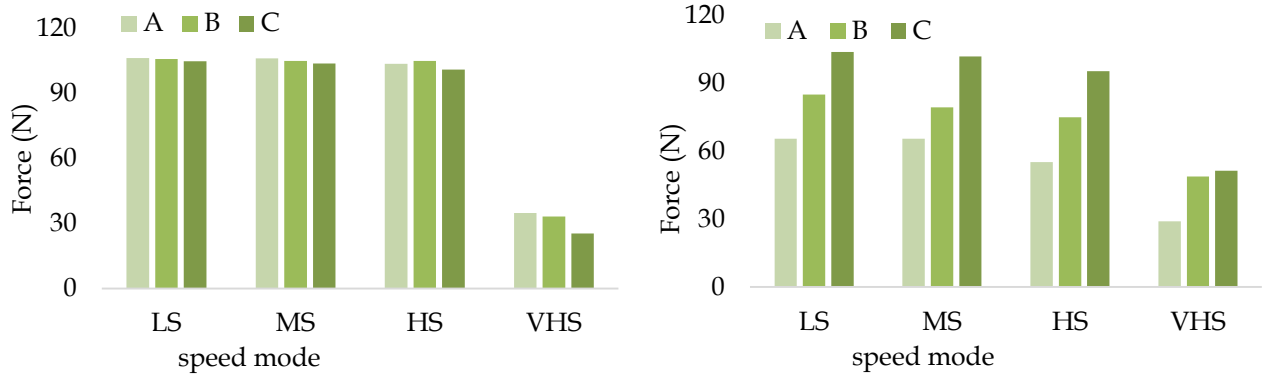

Fig. 7. (a) Parallel and (b) angular gripper spring force analysis. Note: A-type, B-type, and C-type spring

Tab. 7. RMS position error (ISE method) comparison of different speed cases (unit: mm). Note: A-type, B-type and C-type spring

Speed mode	Parallel gripper			Angular gripper		
	A	B	C	A	B	C
LS	0.0113	0.0199	0.0110	0.0557	0.0350	0.0117
MS	0.0146	0.0323	0.0151	0.0784	0.0554	0.0354
HS	0.0266	0.0379	0.0273	0.1177	0.0847	0.0473
VHS	0.0260	0.0140	0.0085	0.0280	0.3765	0.0610

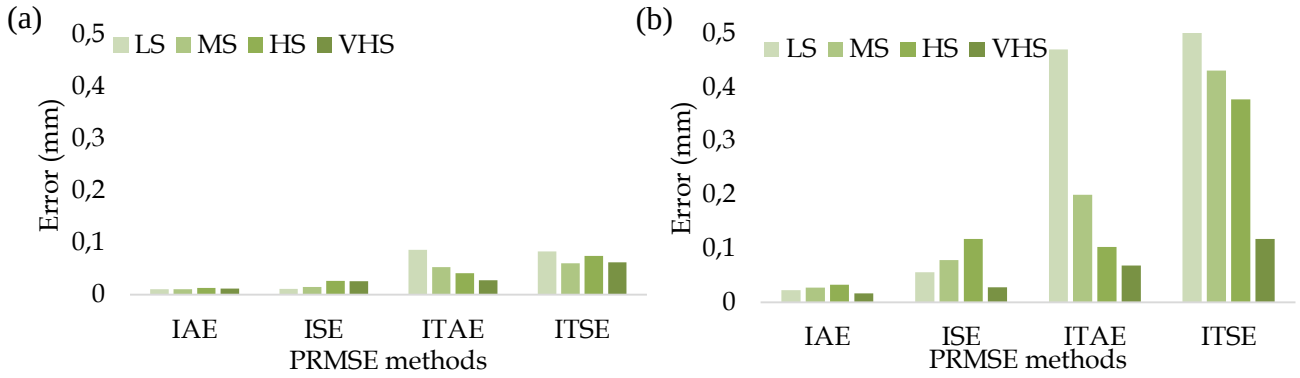

Fig. 8. The PRMSEs of different speed cases with A-type spring: (a) parallel gripper and (b) angular gripper

DOI 10.2478/ama-2021-0010

To evaluate the performance of the maximum force of the electrical LSDIGM, the ratio of the maximum force (RMF) between the desirable force (F_d) and the measured force (F_m) of the system is calculated based on the following equation (16) (Varanasi and Nayfeh, 2004). These ratios are given in Tables 8 and 9. The RMF is the highest ratio of the force applied by the system to the spring.

$$\mathrm{RMF} = \left(1 - \left(\frac{F_d - F_m}{F_d}\right)\right) * 100 \tag{16}$$

Tab. 8. The highest ratio of the force applied-PEG

Speed mode	Spring type		
	A	B	C
LS	92.52	92.17	92.45
MS	92.43	91.39	92.27
HS	90.20	91.39	86.55
VHS	30.35	44.25	46.65

The highest ratio of the force applied by the system to the A-type spring is 92.52% obtained by the low velocity of 1.376 mm/s. It can be seen that in Table 8 the lowest values are related to the fourth row of speeds (VHS) that are less than 50% and the values are unacceptable, indicating that the system did not respond correctly at this speed (Heilala et al., 1992; Pham and Yeo, 1991).

Tab. 9. The highest ratio of the force applied-AEG

Speed mode	Spring type		
	A	B	C
LS	59.42	77.15	91.30
MS	59.42	72.06	90.43
HS	50.09	68.04	87.91
VHS	26.31	28.92	22.07

The highest ratio of the force applied by the system to the C-type spring is 92.45% obtained by the low velocities of 1.495 mm/s. It can be seen that in Table 9 the lowest values are related to the fourth row of speeds (VHS) that are less than 50% and the values are unacceptable, indicating that the system did not respond correctly at this speed. According to Tables 4 and 5, and applying speeds from Tables 8 and 9, the highest power for the parallel gripper is 1.96 watt (A- HS) and for the angular gripper is 1.06 watt (C- HS), respectively.

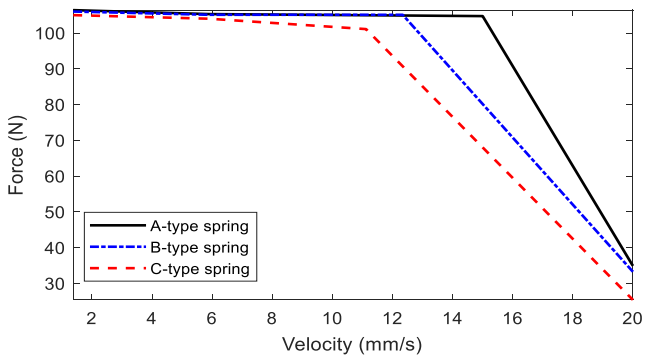

Fig. 9. Velocity–force characteristics

For three springs with different stiffness coefficient values, the force analysis of two different grippers (parallel and angular) is illustrated in Fig. 7. Fig. 8 shows comparison of the position error of the grippers with A-type spring in different speed cases. As can be seen in Fig. 9 (taken from the data in Table 5), the output force of the parallel gripper is nearly constant with 105 N at the velocities of between 1.5 and 12 mm/sec.This relationship between force and speed can be seen in Figs. 7, 8 and 9. The best angular gripper efficiency with a spring stiffness of 11.764 at a velocity of 1.5 mm/sec, which is 29%, and the best parallel gripper efficiency with a spring stiffness of 5.735 at a velocity of 1.5 mm/s, which is 52%.

4. CONCLUSION

In this paper, design and force–velocity performance analysis of the electrical gripper mechanism were examined. In this work, a stepper motor and a lead-screw mechanism were used for an inexpensive gripper as an industrial product. In order to test the performance of the system, an analysis of the LSDIGM, experimental setup with springs and encoders were arranged. The performance of the grippers is dependent on position and power efficiency. The LSDIGMs were tested with different springs and velocity profiles to obtain these efficiencies. The results show that the electrical parallel gripper performed better than the electrical angular gripper, and the highest ratio of the force applied by the proposed parallel gripper is 92.52% at 1.376 mm/sec. Although the proposed method has a very small (low) position error (accuracy) due to the operating characteristics of the stepper motor, it is simpler and less expensive than its counterparts. Therefore, it may be preferred for some applications where minor position errors are not important. Using the proper stepper motor (high power and high position accuracy) and the lead screw, these position errors occurred here may be eliminated very easily.

REFERENCES

1. **Birglen L., Schlicht, T.** (2018), A statistical review of industrial robotic grippers. , *Robotics and Computer-Integrated Manufacturing*, *49*, 88-97.
2. **Chen Z., Xu J., Yu L., Xiong Y., Zhu H.** (2014, May), Design and implementation of the electric gripper control system based on the DSP. In *The 26th Chinese Control and Decision Conference (2014 CCDC)*, (pp. 3513-3517,). IEEE.
3. **Datta R., Pradhan S., Bhattacharya B.** (2015), Analysis and design optimization of a robotic gripper using multiobjective genetic algorithm. , *IEEE Transactions on Systems, Man, and Cybernetics: Systems*, *46*(1), 16-26.
4. **Fotuhi M. J., Bingul Z.** (2021), Fuzzy torque trajectory control of a rotary series elastic actuator with nonlinear friction compensation. , *ISA transactions*.
5. **Fotuhi M. J., & Bingul Z.** (2021), Novel fractional hybrid impedance control of series elastic muscle-tendon actuator. , *Industrial Robot: the international journal of robotics research and application*.
6. **Fotuhi M. J., Yılmaz O., Bingul Z.** (2020), Human postural ankle torque control model during standing posture with a series elastic muscle-tendon actuator. , *SN Applied Sciences*, *2*(2), 1-8.
7. **Hassan A., Abomoharam M.** (2017), Modeling and design optimization of a robot gripper mechanism. , *Robotics and Computer-Integrated Manufacturing*, *46*, 94-103.
8. **Heilala J., Ropponen T., & Airila M.** (1992), Mechatronic design for industrial grippers. , *Mechatronics*, *2*(3), 239-255.

9. **Honarpardaz M., Tarkian M., Ölvander J., Feng X.** (2017), Finger design automation for industrial robot grippers: A review. , *Robotics and Autonomous Systems*, *87*, 104-119.
10. **Hu Z., Wan W., Harada K.** (2019), Designing a mechanical tool for robots with two-finger parallel grippers. , *IEEE Robotics and Automation Letters*, *4*(3), 2981-2988.
11. **Kuang L., Lou Y., Song S.** (2017), Design and fabrication of a novel force sensor for robot grippers. , *IEEE Sensors Journal*, *18*(4), 1410-1418.
12. **Kumar R., Mehta U., Chand P.** (2017), A low cost linear force feedback control system for a two-fingered parallel configuration gripper. , *Procedia computer science*, *105*, 264-269.
13. **Li Q. M., Qin Q. H., Zhang S. W., Deng H.** (2011), Optimal design for heavy forging robot grippers. , In *Applied Mechanics and Materials* (Vol. , 44, pp. 743-747). , Trans Tech Publications Ltd.
14. **Li X., Chen W., Lin W., Low K. H.** (2017), A variable stiffness robotic gripper based on structure-controlled principle. , *IEEE Transactions on Automation Science and Engineering*, *15*(3), 1104-1113.
15. **Liu C. H., Chung F. M., Chen Y., Chiu C. H., Chen T. L.** (2020), Optimal Design of a Motor-Driven Three-Finger Soft Robotic Gripper. , *IEEE/ASME Transactions on Mechatronics*, *25*(4), 1830-1840.
16. **Liu Y., Zhang Y., Xu Q.** (2016), Design and control of a novel compliant constant-force gripper based on buckled fixed-guided beams. , *IEEE/ASME Transactions on Mechatronics*, *22*(1), 476-486.
17. **Lu, Y., Xie , Z., Wang, J., Yue, H., Wu, M., & Liu, Y.** (2019), A novel design of a parallel gripper actuated by a large-stroke shape memory alloy actuator. , *International Journal of Mechanical Sciences*, *159*, 74-80.
18. **Najjari B., Barakati S. M., Mohammadi A., Futohi M. J., Bostanian M.** (2014), Position control of an electro-pneumatic system based on PWM technique and FLC. , *ISA transactions*, *53*(2), 647-657.
19. **Nanda A. P.** (2010), *Design & Development of a Two-jaw parallel Pneumatic Gripper for Robotic Manipulation* (Doctoral dissertation).
20. **Park T. M., Won S. Y., Lee S. R., Sziebig G.** (2016, June), Force feedback based gripper control on a robotic arm. In, *2016 IEEE 20th Jubilee International Conference on Intelligent Engineering Systems (INES)*, (pp. 107-112,). IEEE.
21. **Pham D. T., Yeo S. H.** (1991), Strategies for gripper design and selection in robotic assembly. , *The International Journal of Production Research*, *29*(2), 303-316.
22. **Shaw J. S., Dubey V.** (2016, August), Design of servo actuated robotic gripper using force control for range of objects. , In *2016 International Conference on Advanced Robotics and Intelligent Systems (ARIS)* (pp. 1-6).), IEEE.
23. **Shin D. H., Park T. S., Jeong C. P., Kim Y. G., An J. N**. (2012), Study of torsion spring's parameters with angular type grippers. , In *Advanced Materials Research* (Vol. , 502, pp. 355-359). .Trans Tech Publications Ltd.
24. **Su K. H., Zhong Y. H.** (2018, July), Design of Handling Gripper and its Application to Smart Pet Robot. , In *2018 International Conference on Machine Learning and Cybernetics (ICMLC)* (Vol. , 1, pp. 105-108). IEEE..
25. **Tai K., El-Sayed A. R., Shahriari M., Biglarbegian M., Mahmud S.** (2016), State of the art robotic grippers and applications. , *Robotics*, *5*(2), 11.
26. **Varanasi K. K., & Nayfeh S. A.** (2004), The dynamics of lead-screw drives: low-order modeling and experiments. , *J. Dyn. Sys., Meas., Control*, *126*(2), 388-396.
27. **Wang X., Xiao Y., Fan X., & Zhao Y.** (2016, May), Design and grip force control of dual-motor drive electric gripper with parallel fingers. , In *2016 IEEE Information Technology, Networking, Electronic and Automation Control Conference*, (pp. 696-700,). IEEE.
28. **Xu F., Wang B., Shen J., Hu J., Jiang G.** (2018), Design and realization of the claw gripper system of a climbing robot. , *Journal of Intelligent & Robotic Systems*, *89*(3), 301-317.

MEASUREMENT AND EVALUATION OF FUNCTIONAL AND OPERATIONAL COEFFICIENTS OF HYDRAULIC SOLENOID VALVE PROTOTYPES USED FOR VARIABLE VALVE TIMING CONTROL IN COMBUSTION ENGINES

Marcin KALINOWSKI*, Zbigniew KAMIŃSKI*

*Faculty of Mechanical Engineering, Bialystok University of Technology, ul. Wiejska 45C, 15-351 Białystok, Poland

marcin8891@o2.pl, z.kaminski@pb.edu.pl

received 7 May 2020, revised 26 May 2021, accepted 2 June 2021

Abstract: This paper describes the engineering structure and functions of a typical solenoid valve used in hydraulic mechanisms that are based on variable camshaft timing (VCT). The main operating parameters and functional utility coefficients of hydraulic solenoid valves have been defined. Tests of 10 reference and 10 prototype valves were run on a test stand for a comparative assessment of both engineering concepts based on Welch and Mann–Whitney statistical tests of the mean values of designated coefficients. The studies identified differences between both designs, and the obtained research material was used as an input to improve the performance of the engineered concept. To perform a final evaluation of the effects that arise as a result of changes introduced to some functional–operational coefficients, additional tests are required to be run on an engine testbed. The applied test methodology may then be used for control and verification tests of the valves, which can further be used in VCT technology.

Key words: variable valve timing, hydraulic solenoid valve, prototype verification

1. INTRODUCTION

The variable valve timing (VVT) system allows for selecting valve timing parameters that are optimal for the actual load and speed of a combustion engine (Jankovic and Magner, 2002). The variable settings of camshaft phases change filling parameters of an engine cylinder, which adapt to time-varying loads (Jankovic and Magner, 2002). As a result, depending on the engine design and the number (1, 2 or 4) of mounted valve timing control mechanisms, it is possible to reduce fuel consumption and exhaust emissions (HC and NOx), as well as to increase the engine's power and torque (Chauvin and Petit, 2007; Gray, 1988; Stein et al., 1995).

Certain mechanism designs allow for control of the valve opening angle, valve lift or both (Dresner and Barkan, 1989; Ren, 2011; Stein et al., 1995). More advanced solutions include variable camshaft timing (VCT) mechanisms, using electronically controlled hydraulic actuators for the infinitely variable control of inlet and outlet time of the exhalation valve vs. the crankshaft. With the application of VVT technology, it is possible to control valve stroke, phase and valve timing at any point of the engine map, with the result of enhancing overall engine performance (Hong et al., 2004).

In the hydraulic subsystem of a typical VCT solution, it is a 4-way, 3-position hydraulic solenoid valve that is responsible for appropriate engine timing. The electromagnet of a solenoid valve with infinitely variable opening changes is supplied with a pulse-width modulation (PWM) voltage signal. The electronically controlled solenoid valve redirects pressurised oil from the engine lubrication system to the actuator to move or retract the camshaft angles (rotation of a chain or belt pulley) vs. the crankshaft (Gray, 1988).

Proper action of the hydraulic solenoid valve is highly significant for VCT operation and thus for engine performance. Therefore, at the final stage of the production process, solenoid valves are submitted to control tests (Kosuke et al., 2006) to verify the compliance of features and parameters of a pre-determined number of valves with the requirements set in the standard. In the case of prototype solenoid valves, they become subject to qualification tests (ISO-16750-1, 2006), the goal of which is a comprehensive overview and evaluation of technical and operational features of the product to make a decision concerning either the manufacture of an informative or sample batch or the release of series production of a new solenoid valve.

This paper describes the engineering structure and functions of a typical solenoid valve used in hydraulic mechanisms of VCT, discussing its major operational parameters and functional–operational indices. The method and the test stand used for the measurement and assessment of the indices are also presented with regards to necessary control and qualification tests. The tests run on the test stand have been used for a comparative evaluation of the prototype design of a hydraulic solenoid valve offered for Aftermarket customers, designed and assembled in SMP Poland company and a reference solenoid valve that is used, for example, in Ford V8 combustion engines with 5.4 L capacity in 2004–2010.

DOI 10.2478/ama-2021-0011

2. THE OPERATING PRINCIPLE OF SOLENOID VALVE PARAMETERS AND FUNCTIONAL-OPERATIONAL COEFFICIENTS

A solenoid valve consists of two main sub-assemblies (shown in Fig. 1): an electromagnet (an electromagnetic subsystem) and a hydraulic directional spool valve (a mechanical hydraulic subsystem). The solenoid valve controls the oil stream at its outlet, depending on the supplied voltage signal U_{PWM}, which is determined by PWM during the period in which the electric energy is supplied to the electromagnet. The coil in the electric circuit induces current, i(t), which is directly transformed into force, $F_M(t)$, generated in the electromagnetic circuit and pushing out the valve piston.

To ensure simultaneous motion of the electromagnet piston and the valve spool, a spring is mounted in the solenoid valve, and it performs the function of pushing the piston face to the slide face. Depending on the applied forces acting on the mechanical subsystem (piston, spool and spring), there is movement, x(t), of the spool of the 4-way, 3-position hydraulic directional valve. The movement of the spool in the valve body changes the direction and flows of volumetric oil streams, $q_{vA}(t)$ and $q_{vB}(t)$, supplied from the engine's oil system, on the hydraulic valve outlets.

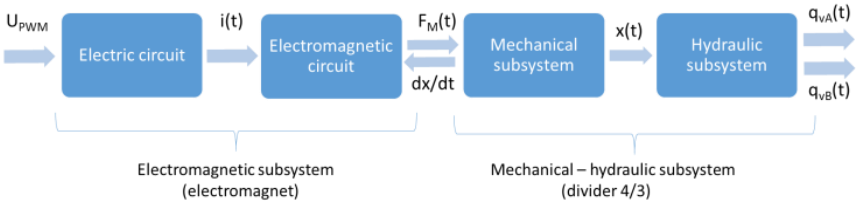

Fig. 1. Flowchart of a hydraulic solenoid valve

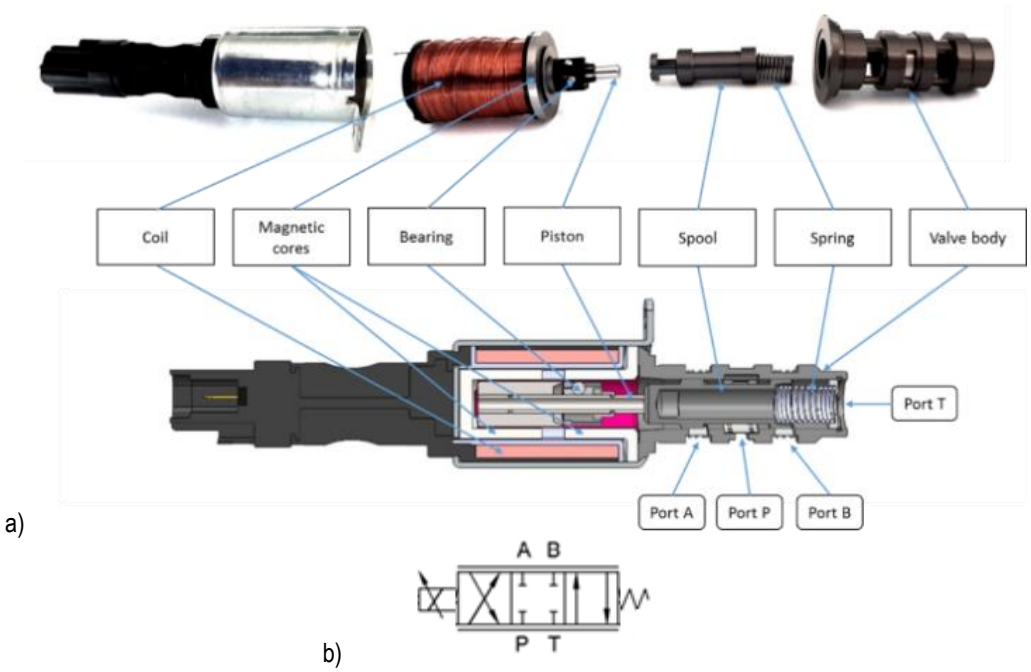

Fig. 2. A cross-section, illustrating the solenoid valve structure (a) and graphic representationl of the proportional electrohydraulic solenoid valve (b)

A cross section of a typical solenoid valve used in VCT systems is shown in Fig. 2. In the initial state, when the current induced in the coil is not so high as to generate a force capable of shifting the electromagnet piston, the spool of the hydraulic solenoid valve is located on the left extreme position, pushed by the force of the return spring. In this case, ports P and A and B and T are connected, and their order is shown in Fig. 2. A maximum oil stream, q_{vA}, flows under pressure from the supply port P to the outlet port A, connected with the actuator's chamber (outflow), while oil from the actuator's other chamber flows to port B and, farther, to port T, connected with the engine's oil sump (runoff).

Increasing the fill factor in the PWM signal brings an increase of coil current and a proportional decrease of flows $q_{vA}(t)$ and $q_{vB}(t)$ until their complete disappearance. In this state, corresponding to the valve spool neutral position, ports A and B are cut off from ports P and T, while the angular position of the camshaft vs. the engine's crankshaft is not changed. This situation is observed at a constant load for a combustion engine, e.g. when constant crankshaft speed is observed. Regarding the valve design, when the valve spool is in a neutral position, there is positive overlap. Further increases of PWM signal fill factor open the passage between ports P and B and A and T (a change of the flow direction to the actuator's chambers)

to the upper control limit, in which the generated electromagnetic force is large enough for the piston to move the spool of the solenoid valve to the other extreme position, where maximum q_{vB} flow value can be obtained. When the solenoid valve is checked on test stands, the outlet ports, A and B, are usually connected.

The main functional–operational parameters, which are important for the assessment of correct solenoid valve operation, include the following:

- The values of volumetric flow, q_{vLC} and q_{vHiC}, in extreme spool positions, are expressed in l/min; for q_{vLC}, it is (P→A→B→T) flow at low control current, while for q_{vHiC}, it is (P→B→A→T) flow at high control current (see Fig. 3a):

$$q_{vLC} = q_V(I = 0.1A) \tag{1}$$

$$q_{vHiC} = q_V(I = 1.3\ A) \tag{2}$$

- The values of pressure, p_{LC} and p_{HiC}, at port P inlet in extreme spool positions, for p_{LC}; it is the pressure value at low control current to the solenoid valve, (I=0.1A) for p_{LC} and (I=1,3A) for p_{HiC} (see Fig. 3e):

$$p_{LC} = p(I = 0.1A) \tag{3}$$

$$p_{HiC} = p(I = 1.3\ A) \tag{4}$$

- The width of the neutral spool shift, defined as the absolute difference of current values at the time when flow drops to 0.5 l/min and at the time when flow rises above 0.5 l/min, is another parameter. This parameter is measured both with increasing, ΔI_{Hinc}, and decreasing, ΔI_{Hdec}, control current (see Fig. 3b):

$$\Delta I_{Hinc} = I_2 - I_1 \tag{5}$$

$$\Delta I_{Hdec} = I_3 - I_4 \tag{6}$$

- The mean current value, I_H, needed to maintain the neutral spool position, is another parameter, which is calculated as an arithmetic mean of the current as flow drops below 0.5 l/min and flow increases above 0.5 l/min, with current increase, I_{Hinc}, and current decrease, I_{Hdec}, respectively (see Fig. 3b):

$$I_{Hinc} = \frac{I_1+I_2}{2} \tag{7}$$

$$I_{Hdec} = \frac{I_3+I_4}{2} \tag{8}$$

- The value of volumetric flow, q_{MLF}, at the current level, which maintains the neutral spool position, is another parameter that functions as a measure of leakage flow; this is measured increase, q_{MLFinc}, and decrease, q_{MLFdec}, in control current (see Fig. 3b):

$$q_{MLFinc} = q_V(I_{Hinc}) \tag{9}$$

$$q_{MLFdec} = q_V(I_{Hdec}) \tag{10}$$

- The value of pressure, p_{MLF}, at the current level, which maintains the neutral spool position, is another parameter that functions as the measure of leakage; this is measured with increase, q_{MLFinc}, and decrease, q_{MLFdec}, in control current (see Fig. 3e):

$$p_{MLFinc} = p(I_{Hinc}) \tag{11}$$

$$p_{MLFdec} = p(I_{Hdec}) \tag{12}$$

- The ΔI_{Hist} parameter functions as the hysteresis, i.e. the difference of current values with the spool moving to the left, ΔI_{HistL}, or to the right, ΔI_{HistR}, for the same flow value of 2 l/min. (see Figure 3c):

$$\Delta I_{HistL} = I_6 - I_5 \tag{13}$$

$$\Delta I_{HistR} = I_8 - I_7 \tag{14}$$

- The slope of the flow characteristic curve during changes of the directional valve state, defined as directional coefficients K_A and K_B of the regression line equation q_v=K·I+C for flows in the range from 0.8 l/min to 2.8 l/min, during increase (inc) and decrease (dec) of the control current I (see Fig. 3d):

$$q_{vAinc} = K_{Ainc}I + C_{Ainc}\ from\ 0.8\ l/min\ < q_{vinc} < 2.8\ l/min\ for\ I < 0.5\ A \tag{15}$$

$$q_{vBinc} = K_{Binc}I + C_{Binc}\ from\ 0.8\ l/min\ < q_{vinc} < 2.8\ l/min\ for\ I > 0.5\ A \tag{16}$$

$$q_{vAdec} = K_{Adec}I + C_{Adec}\ from\ 0.8\ l/min\ < q_{vinc} < 2.8\ l/min\ for\ I > 0.5\ A \tag{17}$$

$$q_{vBdec} = K_{Bdec}I + C_{Bdec}\ from\ 0.8\ l/min\ < q_{vinc} < 2.8\ l/min\ for\ I < 0.5\ A \tag{18}$$

The adequacy of the linear regression model can be tested by the coefficient of determination (Walpole et al., 2012), computed both when the control current is increased, R^2_{Ainc}, R^2_{Binc}, and decreased, R^2_{Adec}, R^2_{Bdec}, respectively, for ports A and B.

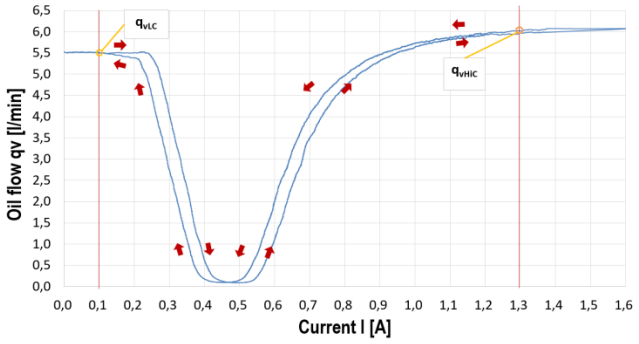

a)

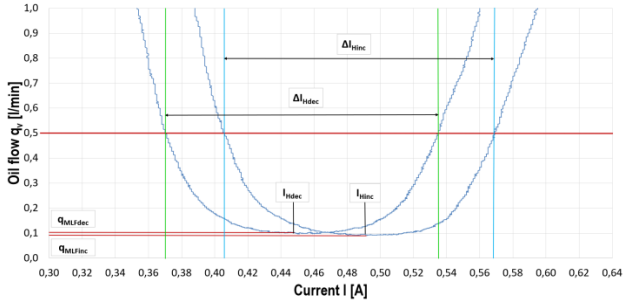

b)

DOI 10.2478/ama-2021-0011

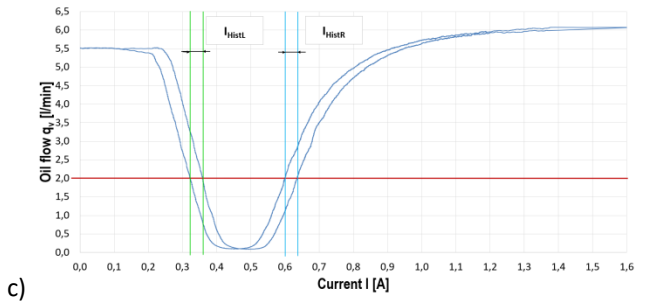

c)

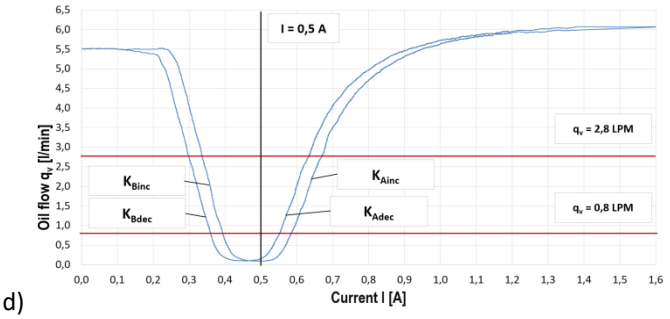

d)

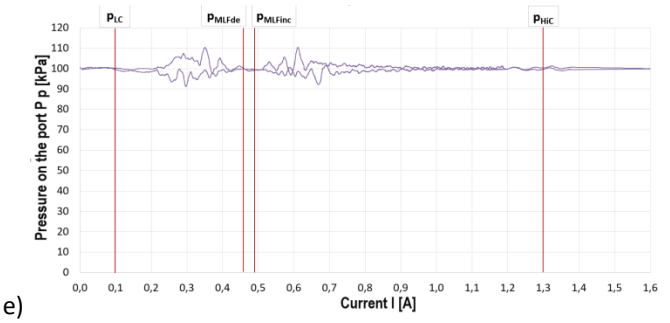

e)

Fig. 3. Oil flow and pressure characteristics in the function of current graphical interpretation of measured parameters

3. TEST STAND AND TEST PROCEDURE

Test stands for hydraulic solenoid valves are types of equipment with various purposes and they differ in their complexities. To check the correct operation of VCT systems, they use simplified models of an internal combustion engine, imitating the target operating conditions. This type of tester uses original combustion engine heads, in which the camshaft is driven by an electric motor and the solenoid valve is connected to a hydraulic power supply, mapping the operating parameters of the lubrication system (Ren, 2011). By simulating the operation of a hydraulic solenoid valve through appropriate control, feedback is obtained about the correct operation of the entire VCT system on which the solenoid valve acts.

Specialist testers are used to check the functional and operational parameters of the hydraulic solenoid valves themselves; the tested valve is mounted to a socket reflecting the original socket in the engine body. By setting oil pressure and controlling the PWM signal, parameters describing valve operation in steady and transient states can be determined. The tester manufactured by INA [8] is an example of such a device. The following parameters can be measured:

- Coil resistance
- Coil inductance
- Insulation resistance
- Magnet force
- Magnet stroke
- Oil pressures
- Oil temperatures
- Oil flow rates
- Duty cycle
- Electrical current.

The following characteristics are determined from the measured parameters:

- Maximum magnet stroke
- Magnet force vs. magnet stroke for a given electrical current
- Magnetic force hysteresis
- Oil volumetric flow in the end positions
- Oil volumetric flow in a closed position (leakage)
- Electrical current in a closed position
- Hysteresis
- Pressure differences

Hydraulic solenoid valves were examined on a test stand manufactured by a US supplier on a special order (see Fig. 4). The test stand has similar functionality to the INA stand, except for the possibility to measure a magnet force.

Fig. 5 presents a schematic diagram of the experimental device. The device consists of a VCT solenoid valve controller, a data acquisition system and a hydraulic driving unit. The hydraulic system is supplied with oil from the gear pump (1), with a capacity of 17.4 l/min; the pressure is set using the relief valve (2) (2700 kPa max.). The proportional reduction valve (3) is intended to reduce pressure in the hydraulic circuit of the tested VCT solenoid valve (6) in the 103–620 kPa range. Directly before the solenoid valve (6), mounted in the test seat, a 3-way, 2-position directional control valve is mounted (5). During tests, the directional control valve redirects oil to port P of the tested solenoid valve and, when the test is completed, oil is redirected to the tank. Oil flow through the tested solenoid valve is measured using a flowmeter (4), with a 0.1–15 l/min scale range and 0.3% accuracy. Oil pressure at selected areas of the hydraulic system is measured using pressure transducers (8 and 9), with a measurement scope to 1000 kPa and 0.1% accuracy. Oil temperature is measured using a transducer (7), with a PT100 sensor with a ±0.33°C accuracy.

Fig. 4. Test stand for testing hydraulic solenoid valves

The coil of the tested solenoid valve is connected to a PWM generator (12), controlled by a control unit (13), integrated with the acquisition system of output signals from the pressure transducers (8 and 9), temperature transducer (7), current transducers (11) and coil resistance transducers (10). Test conditions and parameters can be changed from the control panel (14).

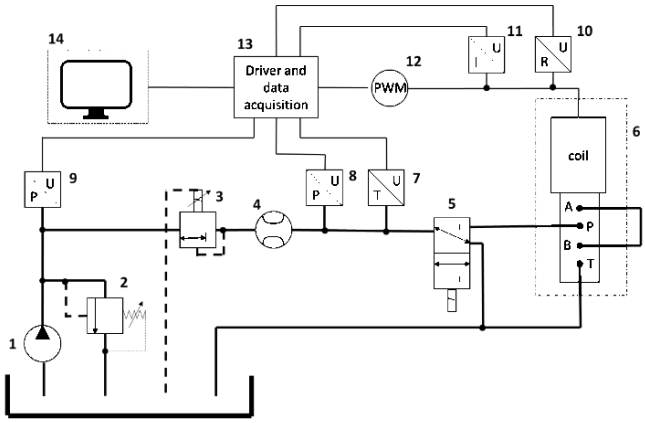

Fig. 5. Schematic diagram of hydraulic solenoid valve test stand:
1 – hydraulic pump, 2 – relief valve, 3 – reduction valve, 4 – flowmeter, 5 – 3-way 2-position directional control valve, 6 – tested hydraulic
solenoid valve, 7 – transducer with PT100 temperature sensor,
8 and 9 – pressure transducers, 10 – coil resistance transducer,
11 – current transducer, 12 – PWM generator, 13 – control unit,
14 – operator panel

When the solenoid valve is checked on test stands, the outlet ports, A and B, are connected. The control unit enables the performance of measurement tests in the automatic mode, in which the full operational cycle of a VCT solenoid valve is run with variable control. The control unit provides a PWM signal with a variable PWM fill factor, causing a change in the current induced in the valve coil. Initially, the PWM fill factor grows in such a way that the current value changes from 0A to 1.6A and then it decreases again. The rate of increasing coil current is specified in the test station programme. To change the current from 0A to 1.6A, the test stand has 11 s, and thereafter it has the subsequent 11 s to decrease from 1.6A to 0A. Depending on the rise time, we can observe different flow characteristics in the part where the valve is closing or opening port A or B. The heat conditions during the test are close to real solenoid valve application conditions, i.e. the temperature of the mounting seat for the solenoid valve and of the flowing oil is 90 ± 5°C. Changes and control of settings are possible by the addition of input data to the device's control software via the control panel.

An integrated part of the test stand is control unit software, designed by the manufacturer of the unit. Based on recorded time histories of oil pressure and flow through the studied solenoid valve, it is possible to determine its proper operating condition, verify whether the valve responds properly to variable control and check if there are no unwanted leaks on the valve. The control unit software also calculates the required functional–operational parameters, defined in Section 2. The advantage of this test stand and software is their universality, i.e. the ability to test solenoid valves with various designs, ease of defining parameters and their tolerance fields, visibility of results and the ability to automate quality control.

An example screenshot presenting measured pressure characteristics of port P (celadon green), with oil flows (yellow) as a function of current and the window with measured results for key solenoid valve coefficients, is shown in Fig. 6.

a)

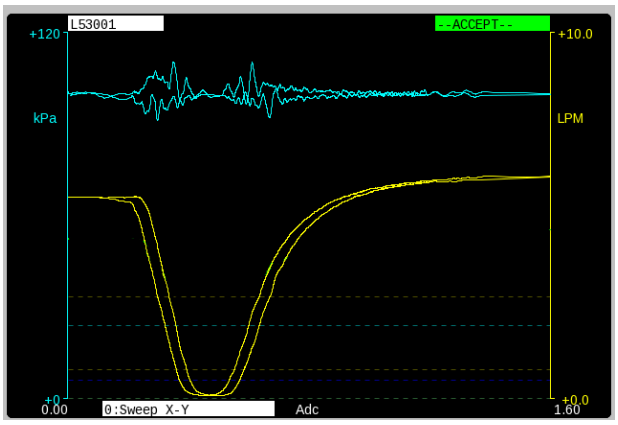

b)

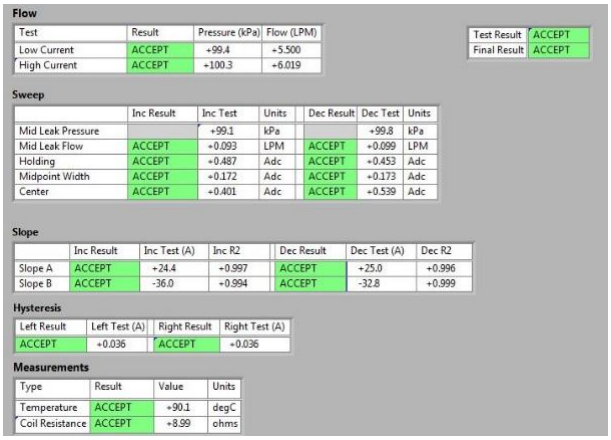

Fig. 6. Examples of hydraulic solenoid valve runs, measured by a tester (a) and the measured results of key solenoid valve parameters (b)

4. TEST COURSE AND RESULTS

Reference hydraulic solenoid valves, operating in the variable cam timing (VCT) system, manufactured by Ford, original equipment (OE) and prototype valves, for which the design is based on the reference products, were selected for tests. See Fig. 7 for the photos of both solenoid valves. The main difference between them is that they use different materials and process parameters. The electromagnet designs that have been selected as prototypes have different number of turns in coil and varying core properties.

The goal of the tests was to evaluate the technical and operational features of the new product. The study programme included automatic tests, runs on a test stand described in the previous section and comprises the reference and prototype solenoid valves.

The results of the tests, performed for 10 of each solenoid valve type enabled us to develop values of functional–operational coefficients.

DOI 10.2478/ama-2021-0011

a)

b)

Fig. 7. A comparison of hydraulic solenoid valves. Ford's design (a) and a prototype solenoid valve design (b)

Then mean values and standard deviations were calculated for particular coefficients. The D`Agostino bilateral skewness test (D'Agostino et al., 1990), recommended for low-number samples (n>8), was applied to check the normality of the distribution of particular coefficients. p-values were computed based on the test statistic s $Z(\sqrt{b_1})$, which is the normal approximation to sample skewness, $\sqrt{b_1}$ [14]. In the majority of cases (Tab. 1), no reasons were found to reject the hypothesis of distribution normality at the α=0.05 (p-value >0.05) significance level.

Tab. 1. The results from tests and D'Agostino normality test for 10 reference solenoid valves from Ford and 10 solenoid valve prototypes

Functional charasteristics			Unit	Reference valves				Prototype valves			
				Average	Standard deviation	Normality test D'Agostino		Average	Standard deviation	Normality test D'Agostino	
						p-value	Normal distribution			p-value	Normal distribution
Flow	Pressure at Low Current	p_{LC}	kPa	100.1	0.400	0.12102	YES	100.3	0.320	0.47581	YES
	Flow at Low Current	q_{vLC}	l/min	5.531	0.069	0.28146	YES	6.061	0.263	0.16469	YES
	Pressure at High Current	p_{HiC}	kPa	100.2	0.271	0.22068	YES	100.3	0.369	0.02372	NO
	Flow at High Current	q_{HiC}	l/min	6.019	0.201	0.19119	YES	6.521	0.207	0.18439	YES
Sweep during increasing current	Mid Leak Pressure	p_{MLPinc}	kPa	99.5	0.504	0.30709	YES	99.5	0.126	0.50000	YES
	Mid Leak Flow	q_{MLFinc}	l/min	0.113	0.019	0.22871	YES	0.169	0.041	0.04255	NO
	Holding current	I_{HCinc}	Adc	0.490	0.004	0.34267	YES	0.524	0.018	0.12583	YES
	Midpoint Width	ΔI_{HCinc}	Adc	0.174	0.009	0.09657	YES	0.211	0.018	0.37345	YES
Sweep during decreasing current	Mid Leak Pressure	p_{MLPdec}	kPa	100.0	0.359	0.00658	NO	100.1	0.322	0.35549	YES
	Mid Leak Flow	q_{MLFdec}	l/min	0.117	0.021	0.19481	YES	0.173	0.040	0.07439	YES
	Holding current	I_{HCdec}	Adc	0.455	0.005	0.21737	YES	0.488	0.016	0.21529	YES
	Midpoint Width	ΔI_{HCdec}	Adc	0.177	0.010	0.26571	YES	0.213	0.020	0.31029	YES
Slope during increasing current	Slope A	K_{Ainc}	l/(min·Adc)	26.0	1.146	0.37679	YES	33.6	3.715	0.22474	YES
		C_{Ainc}	l/min	14.70	0.631	0.48243	YES	14.4	0.681	0.47579	YES
	R2 - slope A	R^2_{KAinc}	-	0.995				0.990			
	Slope B	K_{Binc}	l/(min·Adc)	35.8	0.986	0.28271	YES	30.1	3.587	0.46642	YES
		C_{Binc}	l/min	-13.4	0.559	0.50000	YES	-19.8	0.694	0.45970	YES
	R2 - slope B	R^2_{KBinc}	-	0.995				0.996			
Slope during decreasing current	Slope A	K_{Adec}	l/(min·Adc)	27.9	1.926	0.40153	YES	40.9	5.959	0.25523	YES
		C_{Adec}	l/min	12.6	0.704	0.50000	YES	11.9	0.702	0.47762	YES
	R2 - slope A	R^2_{KAdec}	-	0.995				0.989			
	Slope B	K_{Bdec}	l/(min·Adc)	33.3	1.066	0.31149	YES	27.0	2.922	0.44216	YES
		C_{Bdec}	l/min	-13.1	0.694	0.45536	YES	-21.8	0.681	0.28707	YES
	R2 - slope B	R^2_{KBdec}	-	0.997				0.996			
Hysteresis	Left	ΔI_{HistL}	Adc	0.037	0.001	0.26538	YES	0.038	0.004	0.35467	YES
	Right	ΔI_{HistR}	Adc	0.037	0.003	0.37865	YES	0.042	0.006	0.43033	YES
Temperature			degC	90.5	0.236	0.00975	NO	90.7	0.136	0.09773	YES
Coil resistance			Ohms	8.854	0.077	0.02911	NO	9.144	0.408	0.00497	NO

Significance studies of mean value differences were performed for the same coefficient to achieve a comparative assessment of both solenoid valve designs. Due to ambiguous normality test results, both the Welch's t-test (for population of normal distribution and different variances) (Kanji, 2006; Welch, 1947) and the non-parametric Mann–Whitney U-test, also called the Mann–Whitney–Wilcoxon test (MWW) (Kanji, 2006; Marks et al., 2016), were used for tests of equality of means. Test statistical values and their critical values were designated for both t-test and the U-test, respectively. The test statistics enables calculating the associated probability p-values, which were then compared with the α=0.05 significance level. If p> α, then it was assumed that there were no reasons to reject the null hypothesis, H_0, about the equality of means. If p≤ α, an alternative hypothesis, H_1, was assumed concerning the significance of the differences between the means of particular coefficients. Tab. 2 presents the results of probability calculations (p-values) and test results.

The results of both tests demonstrated statistically significant differences between the coefficients obtained for both groups of solenoid valves, i.e. reference and prototype products. The Welch test enabled identifying 14 differences out of 20 analysed coefficients. On the other hand, the MWW test, besides the same 14 coefficients, also demonstrated a significant difference in solenoid resistance.

Tab. 2. Statistical analysis for 10 reference solenoid valves from Ford and 10 prototype solenoid valves

Functional charasteristics			Unit	Reference	Prototype	Analysis results			
						Welch test		Mann-Whitney U test	
				Average	Average	p-value	Signifcance of difference	p-value	Signifcance of difference
Flow	Pressure at Low Current	p_{LC}	kPa	100.1	100.3	0.1177	NO	0.50286	NO
	Flow at Low Current	q_{vLC}	l/min	5.531	6.061	0.0001	YES	0.00018	YES
	Pressure at High Current	p_{HiC}	kPa	100.2	100.3	0.6984	NO	0.79486	NO
	Flow at High Current	q_{HiC}	l/min	6.019	6.521	0.0000	YES	0.00018	YES
Sweep during increasing current	Mid Leak Pressure	p_{MLPinc}	kPa	99.5	99.5	0.9101	NO	0.56868	NO
	Mid Leak Flow	q_{MLFinc}	l/min	0.113	0.169	0.0024	YES	0.00100	YES
	Holding current	I_{HCinc}	Adc	0.490	0.524	0.0001	YES	0.00018	YES
	Midpoint Width	ΔI_{HCinc}	Adc	0.174	0.211	0.0001	YES	0.00058	YES
Sweep during decreasing current	Mid Leak Pressure	p_{MLPdec}	kPa	100.0	100.1	0.6244	NO	0.30772	NO
	Mid Leak Flow	q_{MLFdec}	l/min	0.117	0.173	0.0021	YES	0.00168	YES
	Holding current	I_{HCdec}	Adc	0.455	0.488	0.0001	YES	0.00018	YES
	Midpoint Width	ΔI_{HCdec}	Adc	0.177	0.213	0.0002	YES	0.00058	YES
Slope during increasing current	Slope A	K_{Ainc}	l/(min·Adc)	26.0	33.6	0.0001	YES	0.00018	YES
		C_{Ainc}	l/min	14.7	14.4	0.2366	NO	0.00018	YES
	R2 - slope A	R^2_{KAinc}	-	0.995	0.990				
	Slope B	K_{Binc}	l/(min·Adc)	35.8	30.1	0.0008	YES	0.00058	YES
		C_{Binc}	l/min	-13.4	-19.8	0.0000	YES	0.00058	YES
	R2 - slope B	R^2_{KBinc}	-	0.995	0.996				
Slope during decreasing current	Slope A	K_{Adec}	l/(min·Adc)	27.9	40.9	0.0000	YES	0.00424	YES
		C_{Adec}	l/min	12.6	11.9	0.0234	YES	0.00424	YES
	R2 - slope A	R^2_{KAdec}	-	0.995	0.989				
	Slope B	K_{Bdec}	l/(min·Adc)	33.3	27.0	0.0001	YES	0.00018	YES
		C_{Bdec}	l/min	-13.1	-21.8	0.0000	YES	0.00018	YES
	R2 - slope B	R^2_{KBdec}	-	0.997	0.996				
Hysteresis	Left	ΔI_{HistL}	Adc	0.037	0.038	0.4258	NO	0.56868	NO
	Right	ΔI_{HistR}	Adc	0.037	0.042	0.0260	YES	0.02574	YES
Temperature			degC	90.5	90.7	0.0423	YES	0.02574	YES
Coil resistance			Ohms	8.854	9.144	0.0627	NO	0.01140	YES

The measurements of volumetric flows, q_{vLC}, at low current levels and q_{vLC} at high current levels (Fig. 8a), demonstrated the flows to be higher for the prototype valves by >0.5 l/min. vs. the flows for the OE valves (by 9.58% and 8.34%, respectively). Since, during the tests, the oil pressures supplied to port P (Fig. 8b) were almost identical (approximately 100 kPa), it could be concluded that the prototype valves were characterised by lower flow resistance in comparison with the OE valves, which is their beneficial feature. A disadvantageous feature is the higher leaks of the prototype valves (Fig. 8c) in their neutral position (when ports A and B are cut off), both during control current increase, q_{MLFinc}, and decrease, q_{MLFdec}, by 49.6% and 47.7%, respectively, when compared with the OE valves. However, comparing the leak values to flow, when a given port is open, the leak in the reference valve constitutes 2.2% of the full volumetric flow, while it is 2.8% in the prototype solenoid valve. This difference should not affect the proper operation of the VVTcontrol system. In addition, the prototype valves demonstrated higher current values necessary to maintain the neutral spool position both during control current increase, I_{Hinc}, and decrease, I_{Hdec}, which results in an extended width of the neutral spool position, ΔI_{Hinc} and ΔI_{Hde}c, by >20%.

The comparative studies also indicated statistically significant differences in the values of directional coefficients for slopes A (when port A is opened) and B (when port B is opened), both directions of control current change. However, the directional coefficients for slope A were higher in the group of prototype valves than in the group of OE reference valves; the situation was reversed for slope B. The reference valves demonstrated lower divergences between the values of directional coefficients. The maximum difference value for OE valves is 7.6 l/(min·A), while for the prototype valves, the maximum difference was 13.9 l/(min·A). Higher differences in directional coefficient values may affect the quality of VVTcontrol. The prototype valves also had a bigger hysteresis on the 'right side' of flow; thus, they needed a bigger difference in the control current to change the state from opened port B to neutral position. There may be a few reasons for the above-mentioned divergences: a difference in the resistance or inductance of the electromagnet coil (solenoid), different stiffness levels of the return springs or differences in the hydraulic solenoid valve geometry (a different overlap degree). The slight difference of approximately 0.3 Ω in solenoid resistance indicates that it was caused by differences in wire diameter and the number of turns in the coil.

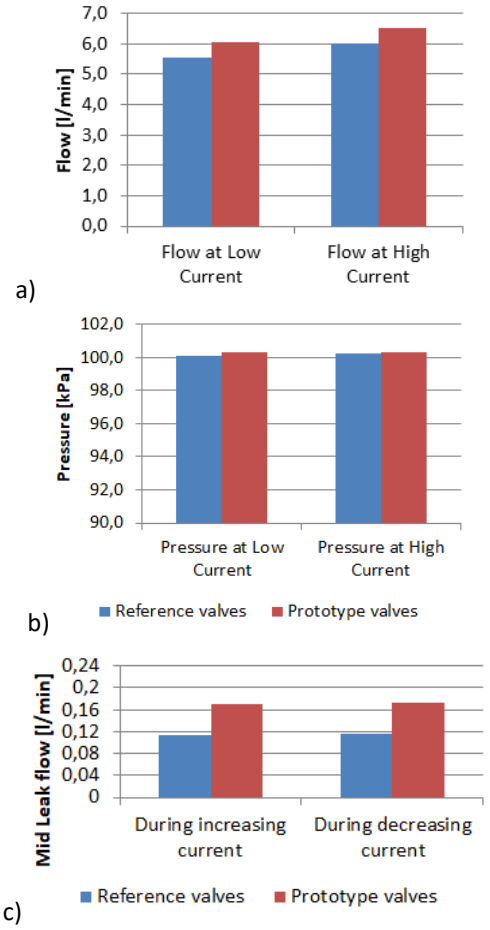

Fig. 8. Comparison of main coefficients: a) flow at low and high current levels, b) pressure at low and high current levels, c) oil leaks at neutral position

5. SUMMARY

The applied method of comparative studies of solenoid valve, based on two sample mean statistical tests, enabled a quality assessment of the engineering project by highlighting significant differences in functional–structural coefficients between 10 prototype products and 10 original solenoid valves; the latter were approached as benchmark products. The tests revealed several statistically significant differences in the coefficients between both groups of solenoid valves; nevertheless, the operational parameters of the prototype products fell within the tolerance limits, approved in the design objectives.

A significant flow resistance reduction, achieved in extreme solenoid valve spool positions and resulting in volumetric flow values >8.5% higher, was a beneficial feature of the prototype design. The less advantageous features, identified during the statistical evaluation, may include higher leaks in the neutral spool position, higher divergences between the values of directional slope coefficients or increased hysteresis in the current required to maintain the neutral spool position. The differences identified among the parameters of tested valves constitute a valuable input research material for studies on design improvements of prototype VCT solenoid valves.

The performed tests demonstrated the suitability of the test stand for measurements and precise designation of operational parameters to meet the needs of control tests and quality assessments of solenoid valves used in VVT technology. However, it should be emphasised that a final evaluation of the effects exerted on combustion engine operation, resulting from changes, introduced to some functional utility coefficients of the solenoid valve, as of a sub-assembly of the control system, requires additional tests to be run on an engine testbed.

REFERENCES

1. **Boguszewicz P., Czyż S.** (2016), Influence of Valves Timing and Valves Lifts on Piston Engine Cylinder Filling (in Polish), *Prace Instytutu Lotnictwa*, 2016,3, 329-345.
2. **Chauvin J., Petit N.** (2007), Experimental control of variable cam timing actuators, *IFAC Proceedings Volumes*, Vol. 40, 10, 95-101.
3. **D'Agostino R. B., Belanger A., D'Agostino R. B. Jr.** (1990), A suggestion for using powerful and informative tests of normality, *The American Statistician*, Vol. 44, 4, 316-321.
4. **Dresner T.,Barkan P.** (1989), A review and classification of variable valve timing mechanisms, *SAE Technical Paper* 890674.
5. **Gray C.** (1988), A review of variable engine valve timing, *SAE Technical Paper* 880386,
6. **Hong H., Parvate-Patil G. B., Gordon B.** (2004), Review and analysis of variable valve timing strategies - eight ways to approach, Proceedings of the Institution of Mechanical Engineers, Part D: *Journal of Automobile Engineering*, Vol. 218, 10, 1179–1200.
7. **IATF 16949: 2016**. Quality management system for organizations in the automotive industry.
8. **INA-Schaeffler KG** (2004), Testing Cam Phaser Systems, Technical publication, Germany
9. **ISO-16750-1: 2006**. Road vehicles - Environmental conditions and testing for electrical and electronic equipment, Part 1: General.
10. **Jankovic M., Magner S. W.** (2002), Variable cam timing: Consequences to automotive engine control design, *IFAC Proceedings Volumes*, Vol. 35, 1, 271-276.
11. **Kanji G.P.** (2006), 100 Statistical Tests, third ed., *Sage Publications*, London,
12. **Kosuke N., Hiroyuki K.. Kazuya K.** (2006), Valve timing and valve lift control mechanism for engines, *Mechatronics*, Vol. 16, 2, 121-129.
13. **Marx A., Backes C., Meese E., Lenhof H. P., Keller A.** (2016), EDISON-WMW: Exact dynamic programming solution of the Wilcoxon-Mann-Whitney test, *Genomics Proteomics Bioinformatics*, Vol. 14, 1, 55-61.
14. **Real statistics using Excel**. http://www.real-statistics.com/tests-normality-and-symmetry/statistical-tests-normality-symmetry/dagostino-pearson-test/ (accessed 29 July 2019)
15. **Ren Z.** (2011), System identification and control design for internal combustion engine variable valve timing systems, PhD Thesis, Michigan State University, Mechanical Engineering
16. **Stein R., Galietti K., Leone T.** (1995), Dual equal VCT – a variable camshaft timing strategy for improved fuel economy and emissions, *SAE Technical Paper* 950975.
17. **Walpole R. E., Myers R. H., Myers S. L.** (2012), Probability end statistics for engineers and scientists, ninth ed., Boston, Prentice-Hall.
18. **Welch B. L.** (1947), The generalization of "Student's" problem when several different population variances are involved, Biometrika, Vol. 34, 1-2, 28-35.

DOI 10.2478/ama-2021-0012

APPROXIMATE FORMULATION OF THE RIGID BODY MOTIONS OF AN ELASTIC RECTANGLE UNDER SLIDING BOUNDARY CONDITIONS

Onur ŞAHİN[*], Barış ERBAŞ[**], Brent WILSON[***],

[*]Department of Mathematics, Giresun University, Gaziler, Prof. Ahmet Taner Kışlalı Cd., 28200 Giresun Turkey
[**]Department of Mathematics, Eskişehir Technical University, 2 Eylül Kampüsü, 26555 Eskişehir, Turkey
[***] HUM Industrial Technology, INC, 911 Washington Ave, Suite 501 St. Louis, Missouri, USA

onur.sahin@giresun.edu.tr, berbas@eskisehir.edu.tr, bwilson@humindustrial.com

received 15 February 2021, revised 31 May 2021, accepted 7 June 2021

Abstract: Low-frequency analysis of in-plane motion of an elastic rectangle subject to end loadings together with sliding boundary conditions is considered. A perturbation scheme is employed to analyze the dynamic response of the elastic rectangle revealing nonhomogeneous boundary-value problems for harmonic and biharmonic equations corresponding to leading and next order expansions, respectively. The solution of the biharmonic equation obtained by the separation of variables, a consequence of sliding boundary conditions, gives an asymptotic correction to the rigid body motion of the rectangle. The derived explicit approximate formulae are tested for different kinds of end loadings together with numerical examples demonstrating the comparison against the exact solutions.

Key words: elastic rectangle, low-frequency, rigid body motion, perturbation scheme, sliding boundary conditions

1. INTRODUCTION

Dynamics of elastic structures, an important branch of solid mechanics, is of interest in several studies encountered in modern industrial applications (see Qin et al., 2008; Martin et al., 2012; Wang, 2014; Kudaibergenov et al., 2016; Viverge et al., 2016). Because most efforts in determining the exact formulations for displacement components and frequencies of such structures generally result in intricate transcendental relations, developing mathematical models that reveal the eigenfrequencies of the system from the traditional equations of rigid body dynamics has become an important endeavor in this area. A considerable number of studies in recent years, therefore, have focused on developing perturbation approaches allowing further insight into the dynamic response of considered elastic structures, e.g., (Kaplunov et al., 2019) and (Kaplunov and Şahin, 2020). It is well known that the conventional equations of rigid body motion are also an application of Newtonian mechanics to elastic solids. We mention (Milton and Willis, 2007) that suggest a new methodology leading to a better approximation of Newton's second law of motion for macroscopic rigid bodies. A distinguished elastodynamic homogenization theory for periodic and random inhomogeneous media was presented in (Srivastava and Nemat-Nasser, 2012; Willis, 1981a; Willis, 1981b), including effective constitutive relations that are nonlocal in space and time.

The self-equilibrated loading, the effect of which is generally omitted by classical rigid body dynamics may be important for various applications, e.g., longitudinal railway dynamics (see Kaplunov et al., 2015). Here, the self-equilibrium is not meant in the sense of Saint-Venant's principle for elastic structures, e.g., (Vigak and Tokovyi, 2002), see also (Gregory and Wan, 1985), and (Kaplunov et al., 2021) adapting this principle for deriving boundary conditions in thin plate theory, but for the setup in which the end forces applied have the resultants of the same amplitude but different direction. A low-frequency analysis of a viscoelastic inhomogeneous bar under the action of end loads, also inspired by modeling of railcar dynamics, is considered in (Kaplunov et al., 2015), and explicit asymptotic corrections to the conventional equations of rigid body motion are presented. We also mention almost rigid body motions of a system consisting of strongly inhomogeneous elastic beams considered in (Şahin, 2019) and (Şahin et al., 2020).

In this paper, we construct a correction to Newton's second law for an elastic rectangle subject to sliding boundary conditions in case of low-frequency motion related to a typical time scale that is assumed to be much greater than the time elastic waves that take the distance between the opposite sides of the rectangle. A perturbation scheme developed in terms of a small parameter associated with low-frequency is used to obtain a generalized formulation for displacements of the elastic rectangle under the influence of edge loadings. The asymptotic study of similar boundary-value problems, such as response of a semi-infinite rectangle to end loadings, usually agree with the Saint-Venant's principle that states that statically self-equilibrated loads cause only local disturbances that do not propagate far away from a loaded area (see Babenkova and Kaplunov, 2004 and Babenkova et al., 2005).

The paper is organized as follows. In Section 2, the statement of in-plane dynamic problem for an elastic rectangle subject to sliding boundary conditions is presented. The governing equations and scaling of the parameters are given. Section 3 contains a perturbation procedure that formulates the problem with the help of a small parameter arising from the definition of the low-frequency of the rectangle. In Section 4, illustrative examples for

the developed model are given, and numerical computations comparing the exact and approximate formulations are presented. Conclusions are given in the last section.

2. STATEMENT OF THE PROBLEM

The in-plane dynamic problem for a linear, isotropic elastic rectangle under the action of edge loads and subject to sliding boundary conditions is considered in the framework of linear elasticity, see Fig. 1.

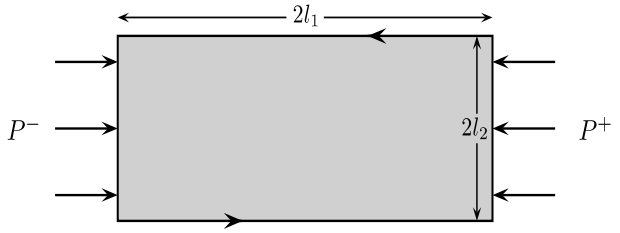

Fig. 1. An elastic rectangle under the considered edge loading and sliding support

In-plane motions of the isotropic rectangle are governed by the equations of two-dimensional elasticity:

$$\sigma_{ij,j} = \rho u_{i,tt} \ , \quad i,j = 1,2 \tag{1}$$

where u_i are in-plane displacement components, σ_{ij} are stress tensor components, t is time, and ρ is mass density. The edge loadings and the sliding boundary conditions on the faces of rectangle are written, respectively, as:

$$\begin{aligned} &\sigma_{11}(\pm l_1, x_2, t) = P^{\pm}, \quad \sigma_{12}(\pm l_1, x_2, t) = 0, \\ &\sigma_{21}(x_1, \pm l_2, t) = 0, \quad\ \ u_2(x_1, \pm l_2, t) = 0. \end{aligned} \tag{2}$$

It is natural to separate the solution in symmetric and antisymmetric parts. For simplicity, we consider only the symmetric part whereas the antisymmetric part may be investigated similarly. Therefore, it is assumed that $P^{\pm} = P^{\pm}(x_2, t)$ are even in x_2. The constitutive equations relating the stress and displacement components are expressed through:

$$\begin{aligned} &\sigma_{ii} = \frac{E(1-\nu)}{(1+\nu)(1-2\nu)}\, u_{i,i} + \frac{E\nu}{(1+\nu)(1-2\nu)} u_{j,j}, \\ &\sigma_{ij} = \frac{E}{2(1+\nu)}(u_{i,j} + u_{j,i}), \quad i \neq j = 1,2. \end{aligned} \tag{3}$$

where E is Young's modulus and ν is Poisson's ratio.

Our main concern is the low-frequency motions of the rectangle under plane strain conditions that suggest introducing the small parameter η defined by:

$$\eta = \frac{l_1}{T c_2} \ll 1, \tag{4}$$

and rescaling the problem in the nondimensional quantities introduced in the form:

$$\begin{aligned} &\sigma_{ij}^* = \frac{\sigma_{ij}}{\eta^2 \rho\, c_2^2}, \quad u_i^* = \frac{u_i}{l_1}, \quad P_*^{\pm} = \frac{P^{\pm}}{\eta^2 \rho\, c_2^2}, \\ &y_i = \frac{x_i}{l_i}, \quad \tau = \frac{t}{T}, \quad i,j = 1,2. \end{aligned} \tag{5}$$

Here, $c_2 = \sqrt{E/2\rho(1+\nu)}$ denotes the transverse wave speed and T is a typical time scale grater than the longitudinal and transverse waves to propagate the distance equal to the thickness of the body.

Formulae (1) and (3) may, therefore, be rewritten as:

$$\begin{aligned} &\sigma_{11,1}^* + \delta \sigma_{12,2}^* = u_{1,\tau\tau}^*, \\ &\sigma_{12,1}^* + \delta \sigma_{22,2}^* = u_{2,\tau\tau}^*, \end{aligned} \tag{6}$$

and:

$$\begin{aligned} &\eta^2 \sigma_{11}^* = \kappa^2\, u_{1,1}^* + \delta\, (\kappa^2 - 2) u_{2,2}^*, \\ &\eta^2 \sigma_{12}^* = \delta\, u_{1,2}^* + u_{2,1}^*, \\ &\eta^2 \sigma_{22}^* = \delta\, \kappa^2\, u_{2,2}^* + (\kappa^2 - 2)\, u_{1,1}^* \end{aligned} \tag{7}$$

where $\delta = l_1/l_2$ and $\kappa^2 = 2(1-\nu)/(1-2\nu)$.

3. PERTURBATION PROCEDURE

We seek the solution $\{u_i, \sigma_{ij}\}$ of the boundary-value problems (6) to (7) in the form of the following asymptotic series:

$$\begin{aligned} &u_i^* = u_i^{(0)} + \eta^2 u_i^{(1)} + \cdots, \\ &\sigma_{ii}^* = \sigma_{ii}^{(0)} + \eta^2 \sigma_{ii}^{(1)} + \cdots, \\ &\sigma_{ij}^* = \sigma_{ij}^{(0)} + \eta^2 \sigma_{ij}^{(1)} + \cdots, \quad i \neq j = 1,2. \end{aligned} \tag{8}$$

On substituting expansions (8) into the governing equations (6) and the constitutive relations (7), the leading order displacements, that is the first components in expansions (8) independent of the powers of η are governed by the boundary-value problem given by:

$$\begin{aligned} &\sigma_{11,1}^{(0)} + \delta \sigma_{12,2}^{(0)} = u_{1,\tau\tau}^{(0)}, \\ &\sigma_{12,1}^{(0)} + \delta \sigma_{22,2}^{(0)} = u_{2,\tau\tau}^{(0)}, \end{aligned} \tag{9}$$

with:

$$\begin{aligned} &\kappa^2\, u_{1,1}^{(0)} + \delta\, (\kappa^2 - 2)\, u_{2,2}^{(0)} = 0, \\ &\delta\, u_{1,2}^{(0)} + u_{2,1}^{(0)} = 0, \\ &\delta\, \kappa^2\, u_{2,2}^{(0)} + (\kappa^2 - 2)\, u_{1,1}^{(0)} = 0, \end{aligned} \tag{10}$$

and:

$$\begin{aligned} &\sigma_{11}^{(0)}\big|_{y_1 = \pm 1} = P_*^{\pm}, \qquad \sigma_{12}^{(0)}\big|_{y_1 = \pm 1} = 0 \\ &\sigma_{21}^{(0)}\big|_{y_2 = \pm 1} = 0, \qquad\ \ u_2^{(0)}\big|_{y_2 = \pm 1} = 0. \end{aligned} \tag{11}$$

Eqns. (10_1) and (10_3) yield that:

$$u_{i,i}^{(0)} = 0, \quad i = 1,2 \tag{12}$$

resulting in:

$$u_1^{(0)} = u_1^{(0)}(y_2, \tau), \quad u_2^{(0)} = u_2^{(0)}(y_1, \tau). \tag{13}$$

Substituting (13) into the second equation of (10) gives the final form of the leading order displacements, that is:

$$u_i^{(0)} = U_i(\tau), \quad i = 1,2. \tag{14}$$

Due to boundary condition (10_3), the second component of

leading order displacement vanishes, i.e.,

$$u_2^{(0)} = 0. \tag{15}$$

Thus, equations (9_1) and (9_2) become:

$$\begin{aligned} &\sigma_{11,1}^{(0)} + \delta\sigma_{12,2}^{(0)} = U_{1,\tau\tau}, \\ &\sigma_{12,1}^{(0)} + \delta\sigma_{22,2}^{(0)} = 0. \end{aligned} \tag{16}$$

Integrating (16_1) over the rectangular region we derive, employing boundary conditions (11):

$$\begin{aligned} &\int_{-1}^{1}\int_{-1}^{1} \frac{\partial\sigma_{11}^{(0)}}{\partial y_1} dy_1 dy_2 + \delta \int_{-1}^{1}\int_{-1}^{1} \frac{\partial\sigma_{12}^{(0)}}{\partial y_2} dy_2 dy_1 = \\ &= \int_{-1}^{1} \left(\sigma_{11}^{(0)}\big|_{y_1=1} - \sigma_{11}^{(0)}\big|_{y_1=-1}\right) dy_2 \\ &+\delta \int_{-1}^{1} \left(\sigma_{12}^{(0)}\big|_{y_2=1} - \sigma_{12}^{(0)}\big|_{y_2=-1}\right) dy_1 \\ &= \int_{-1}^{1} (P_*^+ - P_*^-) dy_2 = 4U_{1,\tau\tau}. \end{aligned} \tag{17}$$

We, therefore, have at leading order:

$$u_{1,\tau\tau}^{(0)} = \frac{1}{4}\int_{-1}^{1} (P_*^+ - P_*^-) dy_2 \tag{18}$$

which is in agreement with Newton's second law:

$$m\, u_{1,\tau\tau} = \frac{1}{4}\int_{-l_2}^{l_2} (\mathrm{P}^+ - \mathrm{P}^-) dx_2 \tag{19}$$

where $m = l_1 l_2 \rho$, see (Kaplunov and Şahin, 2020).

Next order boundary-value problem may be expressed through the pseudo-static equations given by:

$$\begin{aligned} &\kappa^2 \frac{\partial^2 u_1^{(1)}}{\partial y_1^2} + \delta^2 \frac{\partial^2 u_1^{(1)}}{\partial y_2^2} + \delta(\kappa^2 - 1)\frac{\partial^2 u_2^{(1)}}{\partial y_1 \partial y_2} = u_{1,\tau\tau,}^{(0)} \\ &\delta^2\kappa^2 \frac{\partial^2 u_2^{(1)}}{\partial y_2^2} + \frac{\partial^2 u_2^{(1)}}{\partial y_1^2} + \delta(\kappa^2 - 1)\frac{\partial^2 u_1^{(1)}}{\partial y_1 \partial y_2} = 0 \end{aligned} \tag{20}$$

with:

$$\begin{aligned} &\kappa^2\, u_{1,1}^{(1)} + \delta\,(\kappa^2 - 2) u_{2,2}^{(1)}\big|_{y_1=\pm 1} = P_*^{\pm}, \\ &\delta\, u_{1,2}^{(1)} + u_{2,1}^{(1)}\big|_{y_1=\pm 1} = 0, \\ &\delta\, u_{1,2}^{(1)} + u_{2,1}^{(1)}\big|_{y_2=\pm 1} = 0, \\ &u_2^{(1)}\big|_{y_2=\pm 1} = 0. \end{aligned} \tag{21}$$

Let us consider solutions of eqn. (20) in the form:

$$u_1^{(1)} = X_{10}(y_1) + \sum_{n=1}^{\infty} X_{1n}(y_1)\cos n\pi y_2, \tag{22}$$

$$u_2^{(1)} = \sum_{n=1}^{\infty} X_{2n}(y_1)\sin n\pi y_2.$$

Substituting the assumed form of the next order displacements (22) into the governing equations (20) yield:

$$\begin{aligned} &\kappa^2\left(X_{10}'' + \sum_{n=1}^{\infty} X_{1n}''\cos n\pi y_2\right) - \\ &-\delta^2 \sum_{n=1}^{\infty} (n\pi)^2 X_{1n}\cos n\pi y_2 + \\ &+\delta(\kappa^2 - 1)\sum_{n=1}^{\infty} (n\pi) X_{2n}'\cos n\pi y_2 = \\ &= \frac{a_0}{2} + \sum_{n=1}^{\infty} a_n\cos n\pi y_2 + b_n\cos n\pi y_2, \end{aligned} \tag{23}$$

and:

$$\begin{aligned} &-\delta^2\kappa^2 \sum_{n=1}^{\infty} (n\pi)^2 X_{2n}\sin n\pi y_2 + \\ &+\sum_{n=1}^{\infty} X_{2n}''\sin n\pi y_2 - \\ &-\delta(\kappa^2 - 1)\sum_{n=1}^{\infty} (n\pi) X_{1n}'\sin n\pi y_2 = 0 \end{aligned} \tag{24}$$

where:

$$\begin{aligned} &\mathrm{a}_0 = \int_{-1}^{1} p\, dy_2 = 2p, \\ &\mathrm{a}_n = \int_{-1}^{1} p\cos n\pi y_2\, dy_2, \\ &b_n = \int_{-1}^{1} p\sin n\pi y_2\, dy_2, \end{aligned} \tag{25}$$

with:

$$p = \frac{1}{4}\int_{-1}^{1} (P_*^+ - P_*^-) dy_2 \tag{26}$$

which is a constant function. Equations (23) and (24) may be reduced, on using (25) and (26), to the differential equations:

$$\kappa^2 X_{10}'' = \frac{a_0}{2} = p \tag{27}$$

and:

$$\begin{aligned} &\kappa^2 X_{1n}'' - \delta^2 (n\pi)^2 X_{1n} + \delta(\kappa^2 - 1)(n\pi) X_{2n}' = 0, \\ &-\delta^2\kappa^2 (n\pi)^2 X_{2n} + X_{2n}'' - \delta(\kappa^2 - 1)(n\pi) X_{1n}' = 0, \end{aligned} \tag{28}$$

where the term-wise equality of Fourier series is utilized.

The solution of eqn. (27) may clearly be written as:

$$X_{10} = \frac{p}{\kappa^2} A_{10} y_1^2 + A_{20} y_1 + A_{30}. \tag{29}$$

It can also be seen from (28_1) that:

$$X_{2n}{}' = -\frac{\kappa^2}{\delta(\kappa^2-1)(n\pi)} X_{1n}{}'' + \frac{\delta^2 (n\pi)^2}{\delta(\kappa^2-1)(n\pi)} X_{1n}. \tag{30}$$

Taking the derivative of (28_2) with respect to y_1 and using (30) we obtain:

$$X_{1n}^{(\mathrm{iv})} - 2(\delta n\pi)^2 X_{1n}{}'' + (\delta n\pi)^4 X_{1n} = 0 \tag{31}$$

The solution of which may be written as:

$$X_{1n} = (A_1 + \delta n\pi y_1 A_2)\sinh\delta n\pi y_1 + \\ +(A_3 + \delta n\pi y_1 A_4)\cosh\delta n\pi y_1. \tag{32}$$

Substituting (32) into the differential relation (30) results in:

$$X_{2n}' = -\delta n\pi \sinh(\delta n\pi y_1) A_1 - \delta n\pi \cosh(\delta n\pi y_1) A_3 - \\ - \frac{\delta n\pi (2\kappa^2 \cosh(\delta n\pi y_1) + \delta n\pi y_1 (\kappa^2-1)\sinh(\delta n\pi y_1))}{\kappa^2-1} \\ - \frac{\delta n\pi (2\kappa^2 \sinh(\delta n\pi y_1) + \delta n\pi y_1 (\kappa^2-1)\cosh(\delta n\pi y_1))}{\kappa^2-1}$$

which yields:

$$X_{2n} = -\cosh(\delta n\pi y_1) A_1 - \sinh(\delta n\pi y_1) A_3 - \\ - \left(\delta n\pi y_1 \cosh(\delta n\pi y_1) + \frac{(\kappa^2+1)\sinh(\delta n\pi y_1)}{\kappa^2-1} \right) A_2 - \\ - \left(\delta n\pi y_1 \sinh(\delta n\pi y_1) + \frac{(\kappa^2+1)\cosh(\delta n\pi y_1)}{\kappa^2-1} \right) A_4. \tag{33}$$

The displacements may consequently be written as:

$$u_1^{(1)} = \frac{p}{\kappa^2} A_{10} y_1^2 + A_{20} y_1 + A_{30} + \\ + \sum_{n=1}^{\infty} \{(A_1 + \delta n\pi y_1 A_2)\sinh\delta n\pi y_1 + \\ +(A_3 + \delta n\pi y_1 A_4)\cosh\delta n\pi y_1\} \cos n\pi y_2 \tag{34}$$

and:

$$u_2^{(1)} = \sum_{n=1}^{\infty} -\cosh(\delta n\pi y_1) A_1 - \sinh(\delta n\pi y_1) A_3 - \\ - \left(\delta n\pi y_1 \cosh(\delta n\pi y_1) + \frac{(\kappa^2+1)\sinh(\delta n\pi y_1)}{\kappa^2-1} \right) A_2 - \\ - \left(\delta n\pi y_1 \sinh(\delta n\pi y_1) + \frac{(\kappa^2+1)\cosh(\delta n\pi y_1)}{\kappa^2-1} \right) A_4 \} \sin n\pi y_2. \tag{35}$$

Boundary condition (21) may be written as:

$$\kappa^2 u_{1,1}^{(1)} + \delta(\kappa^2-2) u_{2,2}^{(1)}\big|_{y_1=\pm 1} = \frac{B_0^{\pm}}{2} + \\ + \sum_{n=1}^{\infty} B_n^{\pm} \cos n\pi y_2 + C_n^{\pm} \sin n\pi y_2, \\ \delta u_{1,2}^{(1)} + u_{2,1}^{(1)}\big|_{y_1=\pm 1} = 0, \\ \delta u_{1,2}^{(1)} + u_{2,1}^{(1)}\big|_{y_2=\pm 1} = 0, \\ u_2^{(1)}\big|_{y_2=\pm 1} = 0 \tag{36}$$

where:

$$B_0^{\pm} = \int_{-1}^{1} P_*^{\pm} dy_2, \\ B_n^{\pm} = \int_{-1}^{1} P_*^{\pm} \cos n\pi y_2 \, dy_2, \\ C_n^{\pm} = \int_{-1}^{1} P_*^{\pm} \sin n\pi y_2 \, dy_2. \tag{37}$$

On employing, the displacements (34) and (35) in the boundary conditions (36) yield, respectively, the following equations for X_{10}, X_1 and X_2:

$$\kappa^2 \frac{\partial X_{10}}{\partial y_1}\Big|_{y_1=\pm 1} = \frac{1}{2} \int_{-1}^{1} P_*^{\pm} dy_2 \tag{38}$$

and:

$$\kappa^2 \sum_{n=1}^{\infty} X_{1n}'(y_1) \cos n\pi y_2 + \\ + \delta(\kappa^2-2) n\pi \sum_{n=1}^{\infty} X_{2n}(y_1) \cos n\pi y_2 |_{y_1=\pm 1} = \\ = \sum_{n=1}^{\infty} B_n^{\pm} \cos n\pi y_2 + C_n^{\pm} \sin n\pi y_2, \\ - \delta\kappa^2 n\pi \sum_{n=1}^{\infty} X_{1n}(y_1) \sin n\pi y_2 + \\ + \sum_{n=1}^{\infty} X_{2n}'(y_1) \sin n\pi y_2 |_{y_1=\pm 1} = 0 \tag{39}$$

resulting in:

$$\kappa^2 X_{1n}'(y_1) + \delta(\kappa^2-2) n\pi X_{2n}(y_1)|_{y_1=\pm 1} \\ = \int_{-1}^{1} P_*^{\pm} \cos n\pi y_2 \, dy_2, \\ -\delta \kappa^2 n\pi X_{1n}(y_1) + X_{2n}{}'(y_1)|_{y_1=\pm 1} = 0. \tag{40}$$

All coefficients appearing in the displacements $u_1^{(1)}$ and $u_2^{(1)}$, see (34) and (56), may be calculated substituting expressions (29), (32) and (33) into equation (40), which gives:

$$A_{10} = \frac{1}{2}, \tag{41}$$

$$A_{20} = \frac{1}{4\kappa^2}\int_{-1}^{1}(P_*^+ + P_*^-)dy_2,$$

and:

$$A_1 = \frac{\cosh(\delta n\pi)(\delta n\pi(\kappa^2-1)+\kappa^2\tanh(\delta n\pi))}{2\delta n\pi(\kappa^2-1)(2\delta n\pi+\sinh(2\delta n\pi))}I_1,$$
$$A_2 = \frac{\cosh(\delta n\pi)}{2\delta n\pi(2\delta n\pi-\sinh(2\delta n\pi))}\ I_2,$$
$$A_3 = -\frac{\cosh(\delta n\pi)\ (\kappa^2+\delta n\pi(\kappa^2-1)\tanh(\delta n\pi))}{2\delta n\pi(\kappa^2-1)(2\delta n\pi-\sinh(2\delta n\pi))}\ I_2, \quad (42)$$
$$A_4 = -\frac{\sinh(\delta n\pi)}{2\delta n\pi(2\delta n\pi+\sinh(2\delta n\pi))}\ I_1,$$

where:

$$\mathrm{I}_1 = \int_{-1}^{1}(P_*^+ + P_*^-)\ \cos n\pi y_2\ dy_2,$$
$$\mathrm{I}_2 = \int_{-1}^{1}(P_*^+ - P_*^-)\ \cos n\pi y_2\ dy_2. \quad (43)$$

A higher order approximation is still needed to determine the coefficient A_{30}. To this end, starting from (6) and (34), we write:

$$\sigma_{11,1}^{(1)} + \delta\sigma_{12,2}^{(1)} = u_{1,\tau\tau}^{(1)} \quad (44)$$

with:

$$\sigma_{11}^{(1)}\big|_{y_1=\pm1} = \sigma_{12}^{(1)}\big|_{y_2=\pm1} = 0. \quad (45)$$

Integrating equation (44) over the rectangular region and using boundary condition (45), we obtain:

$$A_{30} = -\frac{p}{6\kappa^2}. \quad (46)$$

Thus, the expressions for the next order displacements $u_1^{(1)}$ and $u_2^{(1)}$ are fully established. The following section aims to present demonstrative examples.

4. ILLUSTRATIVE EXAMPLES

4.1. Time-Harmonic Loadings of Parabolic Types

First, we consider time-harmonic, parabolic type end loadings given by:

$$P^{\pm} = M^{\pm}(1 - x_2^2/l_2^2)e^{-i\omega t} \quad (47)$$

where $M^{\pm}$ is a constant amplitude. Below, we utilize the scaling introduced in (5) and also omit the time-harmonic factor $e^{-i\omega t}$. It is, therefore, an easy matter to obtain the tangential displacement using (18), which is:

$$u_1^{(0)} = -\frac{M_*^+ - M_*^-}{3} \quad (48)$$

where $M_*^{\pm}$ is scaled as in (5).

The solution of the next order problem may be written from eqns. (34) and (35) as:

$$u_1^{(1)} = \frac{M_*^+ - M_*^-}{6\kappa^2}y_1^2 + \frac{M_*^+ + M_*^-}{3\kappa^2}y_1 - \frac{M_*^+ - M_*^-}{18\kappa^2} + \\ + \sum_{n=1}^{\infty}\{(D_1 + \delta n\pi y_1 D_2)\sinh\delta n\pi y_1 + \\ +(D_3 + \delta n\pi y_1 D_4)\cosh\delta n\pi y_1\}\cos n\pi y_2 \quad (49)$$

and:

$$u_2^{(1)} = \sum_{n=1}^{\infty}\{-\cosh(\delta n\pi y_1)D_1 - \sinh(\delta n\pi y_1)D_3 - \\ -\left(\delta n\pi y_1\cosh(\delta n\pi y_1) + \frac{(\kappa^2+1)\sinh(\delta n\pi y_1)}{\kappa^2-1}\right)D_2 - \\ -\left(\delta n\pi y_1\sinh(\delta n\pi y_1) + \frac{(\kappa^2+1)\cosh(\delta n\pi y_1)}{\kappa^2-1}\right)D_4\Big\}\sin n\pi y_2 \quad (50)$$

where:

$$D_1 = \frac{(-1)^{n+1}2(M_*^+ + M_*^-)\cosh(\delta n\pi)}{\delta n^3\pi^3(\kappa^2-1)(2\delta n\pi+\sinh(2\delta n\pi))}\times \\ \times(\delta n\pi(\kappa^2-1)+\kappa^2\tanh(\delta n\pi)),$$
$$D_2 = \frac{(-1)^{n+1}2(M_*^+ - M_*^-)\cosh(\delta n\pi)),}{\delta n^3\pi^3(2\delta n\pi-\sinh(2\delta n\pi))}$$
$$D_3 = \frac{(-1)^{n}2(M_*^+ - M_*^-)\cosh(\delta n\pi))}{\delta n^3\pi^3(\kappa^2-1)(2\delta n\pi-\sinh(2\delta n\pi))}\times \\ \times(\kappa^2+\delta n\pi(\kappa^2-1)\tanh(\delta n\pi)), \quad (51)$$
$$D_4 = \frac{(-1)^{n}2(M_*^+ + M_*^-)\sinh(\delta n\pi)}{\delta n^3\pi^3(2\delta n\pi+\sinh(2\delta n\pi))}.$$

In the following figures, we illustrate the comparisons of approximate and exact longitudinal displacement u_1 given, respectively, by formulas (49) and (60). Here, we set the Poisson ratio $\nu = 0.25$ together with $\delta = 1$. Figures 2 and 3 illustrate the behavior of the approximate and exact displacement component u_1 along the longitudinal coordinate y_1 under the action of self-equilibrated and non-self-equilibrated loads, that is, we take $M_*^+ = M_*^- = 1$ and $M_*^+ = -M_*^- = 1$, respectively. An excellent agreement is evident for the parameter η, even when its value is not very small.

In both of these figures, we consider only positive y_2-values due to the intrinsic symmetry. The largest displacements occur along the y_1-axis, while they decrease in the y_2-direction due to the form of the applied loads. However, for a self-equilibrated load, Fig. 2, there is no displacement along the y_2-axis, i.e., at $y_1 = 0$, which is not observed in the case of a non-self-equilibrated load, see Fig 3.

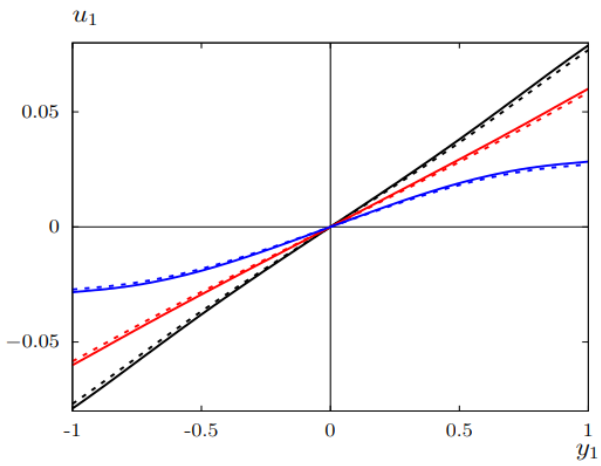

Fig. 2. Comparison of exact (solid lines) and approximate (dotted lines) displacements u_1 versus y_1 for $y_2 = 0$ (black), $y_2 = 0.5$ (red), and $y_2 = 1$ (blue) in case of a self-equilibrated load at $\eta = 0.5$

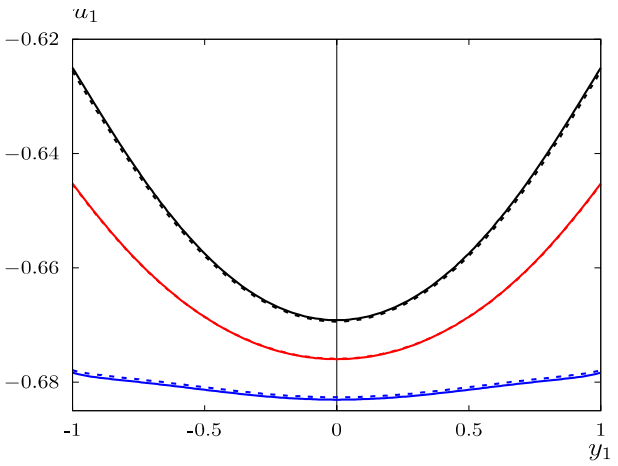

Fig. 3. Comparison of exact (solid lines) and approximate (dotted lines) displacements u_1 versus y_1 for $y_2 = 0$ (black), $y_2 = 0.5$ (red), and $y_2 = 1$ (blue) in case of a non-self-equilibrated load at $\eta = 0.5$

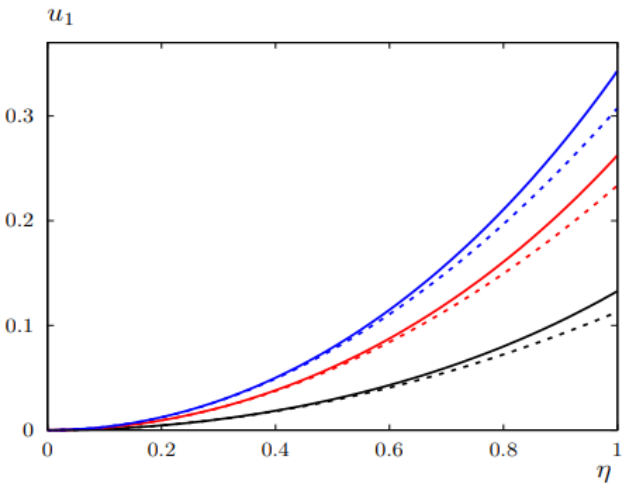

Fig. 4. Comparison of exact (solid lines) and approximate (dotted lines) displacements u_1 versus η for $y_1 = y_2 = 0.5$ (black), $y_1 = 1$, $y_2 = 0.5$ (red), and $y_1 = 1$, $y_2 = 0$ (blue) in case of a self-equilibrated load

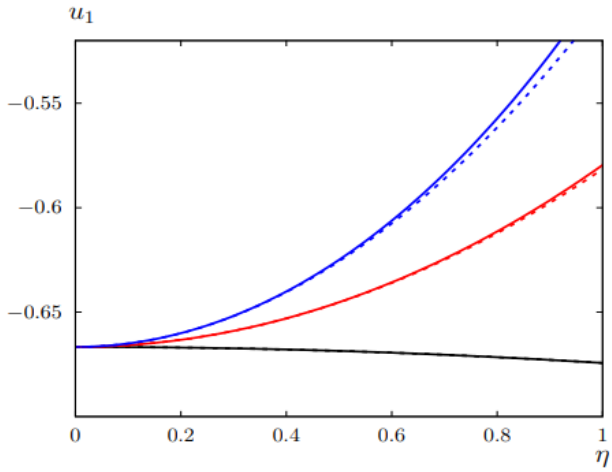

Fig. 5. Comparison of exact (solid lines) and approximate (dotted lines) displacements u_1 versus η for $y_1 = y_2 = 0.5$ (black), $y_1 = 1$, $y_2 = 0.5$ (red), and $y_1 = 1$, $y_2 = 0$ (blue) in case of a non-self-equilibrated load

Figures 4 and 5 demonstrate the variations of the longitudinal displacement with respect to the small frequency η in case of self- and non-self-equilibrated loads, respectively. A remarkable coincidence between the approximate and exact displacements is observed even in the global low-frequency regime. When the load is self-equilibrated, we observe from Fig. 4 that at very low frequencies the horizontal displacement u_1 acquires considerably small values both along the y_1-axis ($y_2 = 0$) as well as in the vertical direction. As the frequency increases, the horizontal displacement attains larger values that also increase in the positive vertical direction. For a non-self-equilibrated load, the displacements for the considered points are not small even for low-frequency regime. The displacement characteristics are also quite different than the previous case, clearly a result of non-self-equilibrated loading.

4.1. Time-Harmonic Uniform Loading

We now consider time-harmonic, uniform end loadings in the form:

$$P^{\pm} = A^{\pm} e^{-i\omega t} \tag{52}$$

where $A^{\pm}$ are again assumed to be constants. On using eqn. (18) and omitting $e^{-i\omega t}$, the leading order displacement may be obtained as:

$$u_1^{(0)} = -\frac{A_*^+ - A_*^-}{2}. \tag{53}$$

Similar to previous section, the next order solution for the displacement components may be written as

On substituting expansions (8) into the governing equations (6) and the constitutive relations (7), the leading order displacements, that:

$$u_1^{(1)} = \frac{A_*^+ - A_*^-}{4\kappa^2} y_1^2 + \frac{A_*^+ + A_*^-}{2\kappa^2} y_1 - \frac{A_*^+ - A_*^-}{12\kappa^2}, \tag{54}$$

and:

$$u_2^{(1)} = 0 \tag{55}$$

since each coefficient given in (43) becomes zero.

DOI 10.2478/ama-2021-0012

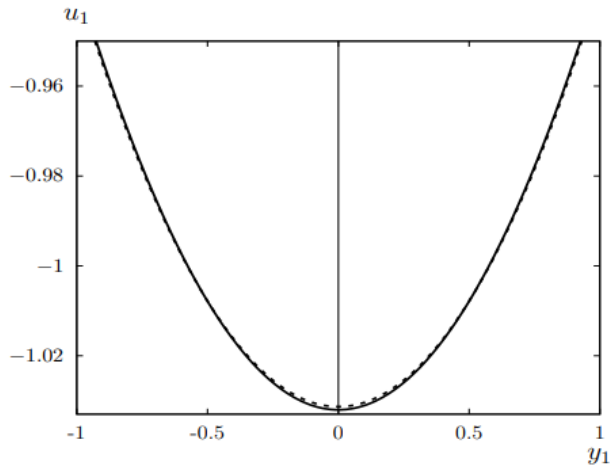

Fig. 6. Comparison of exact (solid lines) and approximate (dotted lines) displacements u_1 versus y_1 in case of a self-equilibrated load at $\eta = 0.75$

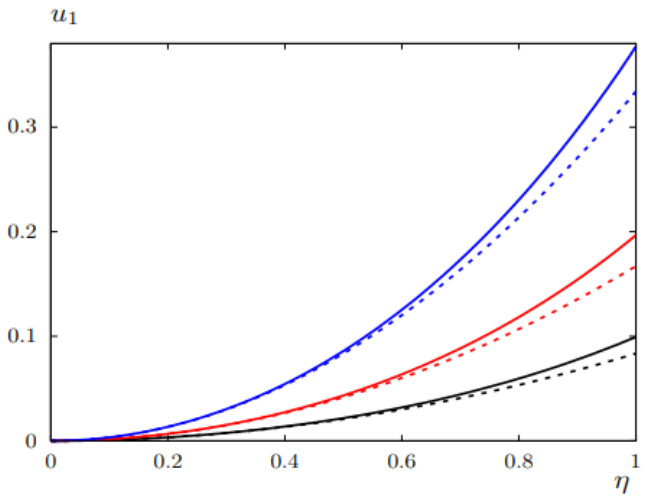

Fig. 7. Comparison of exact (solid lines) and approximate (dotted lines) displacements u_1 versus η for $y_1 = 0.25$ (black), $y_1 = 0.5$ (red), and $y_1 = 1$(blue) in case of a self-equilibrated load

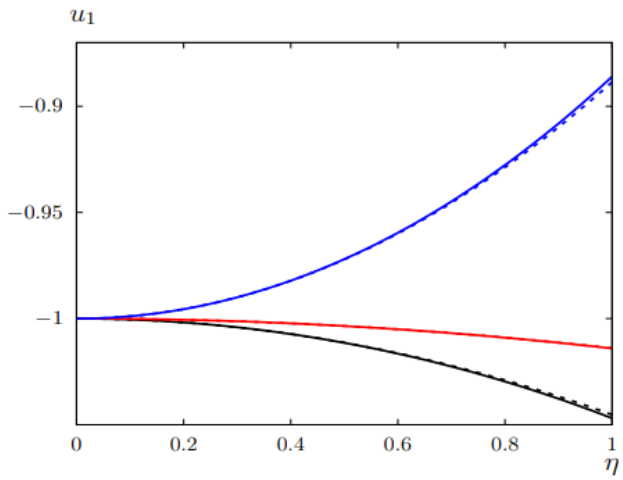

Fig. 8. Comparison of exact (solid lines) and approximate (dotted lines) displacements u_1 vs η for $y_1 = 0.25$ (black), $y_1 = 0.5$ (red), and $y_1 = 1$(blue) in case of a non-self-equilibrated load

The effect of a non-self-equilibrated uniform loading on the horizontal displacement along the y_1-axis is displayed both for approximate and exact formulations in Fig. 6. An apparent parabolic form emerges with the largest displacement arising along the center of the rectangle.

Figures 7 and 8 exhibit the same characteristics as their counterparts for parabolic loading. For a fixed value of the frequency, the displacements grow larger as we move to the edges of the rectangle. The displacements are positive for a self-equilibrated load, see Fig. 7, and they are negative for a non-self-equilibrated load, see Fig. 8. We also note that, as in the case of parabolic loading, the accuracy of approximate formulation is significant, which are displayed against the exact formulation in Figs. 6–8.

5. CONCLUSIONS

A perturbation scheme is implemented to calculate the first order low-frequency corrections to rigid body motions of an elastic rectangle subject to longitudinal forces applied to its opposite faces together with sliding boundary conditions on its upper and lower faces. The leading order solution of the nonhomogeneous harmonic equation corresponds to Newton's second law whereas the next order terms results in a nonhomogeneous biharmonic equation. A similar problem was considered in (Kaplunov and Şahin, 2020); however, the boundary conditions allowed explicit solutions only in the antiplane case and further assumptions had to be imposed in the case of in-plane motions. The sliding boundary considered in this paper, fortunately, allows the variables to be separated resulting in the derivation of an explicit approximate solution for the in-plane displacements of the rectangle. The solution of the next order problem, namely, the nonhomogeneous biharmonic equation, leads to a correction to the classical rigid body dynamics, see eqns. (35) and (36). The obtained corrections to rigid body motions in the low-frequency regime under the action of both self- and non-self-equilibrated loads allow the calculation of the variation of stress and displacement components over the interior of the rectangle. Several figures are presented displaying the variation of displacement components for the derived approximate model along with their exact counterparts. An excellent coincidence between the asymptotic and exact results is observed for a rather large interval of the small parameter η in all figures. It should also be noted that the case of self-equilibrated loading cannot be treated within the classical rigid body model.

The perturbation approach may also be extended to investigate the dynamic response of strongly inhomogeneous layered rectangular structures, see (Prikazchikova et al., 2020), with inner and/or outer sliding boundaries, including anisotropy; multi-span rectangles with contrasting material properties may also be investigated. It is also possible to consider a set of arbitrary stresses applied to opposing sides of the rectangle. The nonlinear structures might also be another promising research area for which the developed model may be employed. In addition, various problems of multi-body dynamics, including calculation of longitudinal forces in railcar dynamics might be taken into account.

APPENDIX. EXACT SOLUTION

In this section, we present the exact solutions of the longitudinal and transverse displacements of the elastic rectangle subject

to time-harmonic parabolic and uniform type end loadings. First, we derive the formulations for the parabolic type end loading.

The equations of motion and boundary conditions given in (1) and (2) can be written in terms of the displacement components, respectively, as:

$$\begin{aligned}&\frac{E(1-\nu)}{(1+\nu)(1-2\nu)}\frac{\partial^2 u_1}{\partial x_1^2}+\frac{E}{2(1+\nu)}\frac{\partial^2 u_1}{\partial x_2^2}+\\&+\frac{E(1-\nu)}{2(1+\nu)(1-2\nu)}\frac{\partial^2 u_2}{\partial x_1\partial x_2}=\rho\frac{\partial^2 u_1}{\partial t^2},\\&\frac{E}{2(1+\nu)}\frac{\partial^2 u_2}{\partial x_1^2}+\frac{E(1-\nu)}{(1+\nu)(1-2\nu)}\frac{\partial^2 u_2}{\partial x_2^2}+\\&+\frac{E(1-\nu)}{2(1+\nu)(1-2\nu)}\frac{\partial^2 u_1}{\partial x_1\partial x_2}=\rho\frac{\partial^2 u_2}{\partial t^2},\end{aligned}\tag{56}$$

and:

$$\begin{aligned}&\frac{E(1-\nu)}{(1+\nu)(1-2\nu)}\frac{\partial u_1}{\partial x_1}\\&\qquad+\frac{E\nu}{(1+\nu)(1-2\nu)}\frac{\partial u_2}{\partial x_2}\Big|_{x_1=\pm l_1}=\\&=M^{\pm}\left(1-\frac{x_2^2}{l_2^2}\right)e^{-i\omega t},\\&\frac{\partial u_1}{\partial x_2}+\frac{\partial u_2}{\partial x_1}\Big|_{x_1=\pm l_1}=0,\\&\frac{\partial u_1}{\partial x_2}+\frac{\partial u_2}{\partial x_1}\Big|_{x_2=\pm l_2}=0,\\&u_2|_{x_2=\pm l_2}.\end{aligned}\tag{57}$$

Considering time-harmonic vibrations together with scaled quantities introduced in (5), the boundary-value problem (56) and (57) may be rewritten as:

$$\begin{aligned}&\kappa^2\frac{\partial^2 u_1^*}{\partial y_1^2}+\delta^2\frac{\partial^2 u_1^*}{\partial y_2^2}+\delta(\kappa^2-1)\frac{\partial^2 u_2^*}{\partial y_1\partial y_2}+\eta^2 u_1^*,\\&\frac{\partial^2 u_2^*}{\partial y_1^2}+\delta^2\kappa^2\frac{\partial^2 u_2^*}{\partial y_2^2}+\delta(\kappa^2-1)\frac{\partial^2 u_1^*}{\partial y_1\partial y_2}+\eta^2 u_2^*,\end{aligned}\tag{58}$$

with:

$$\begin{aligned}&\kappa^2\frac{\partial u_1^*}{\partial y_1}+\delta(\kappa^2-2)\frac{\partial u_2^*}{\partial y_2}\Big|_{y_1=\pm 1}=\eta^2 M_*^{\pm}(1-y_2^2),\\&\delta\frac{\partial u_1^*}{\partial y_2}+\frac{\partial u_2^*}{\partial y_1}\Big|_{y_1=\pm 1}=0,\\&\delta\frac{\partial u_1^*}{\partial y_2}+\frac{\partial u_2^*}{\partial y_1}\Big|_{y_2=\pm 1}=0,\\&u_2^*|_{y_2=\pm 1}\end{aligned}\tag{59}$$

where $\eta=\omega l_1/c_2$.

Let us assume the solutions of (58) are in the form:

$$u_1^*=u_{10}^*+\sum_{n=1}^{\infty}u_{1n}^*(y_1)\cos n\pi y_2,\tag{60}$$

$$u_2^*=\sum_{n=1}^{\infty}u_{2n}^*(y_1)\cos n\pi y_2,$$

see (Kaplunov et al., 2005). Substituting equations (60) into the governing equations and boundary conditions given by (58) and (59) and employing a straightforward but a lengthy algebra we arrive at, omitting all the details:

$$\begin{aligned}u_{10}^*&=-\frac{M_*^+-M_*^-}{3\kappa\sin\frac{\eta}{\kappa}}\eta\cos\left(\frac{\eta}{\kappa}y_1\right)\\&\quad+\frac{M_*^++M_*^-}{3\kappa\cos\frac{\eta}{\kappa}}\eta\sin\left(\frac{\eta}{\kappa}y_1\right),\\u_{1n}^*&=E_1\cosh r_1y_1+E_2\sinh r_1y_1+E_3\cosh r_2y_1\\&\quad+E_4\sinh r_2y_1,\\u_{2n}^*&=-\frac{n\pi\delta E_1}{r_1}\sinh r_1y_1-\frac{n\pi\delta E_2}{r_1}\cosh r_1y_1-\\&\quad-\frac{r_2E_3}{n\pi\delta}\sinh r_2y_1-\frac{r_2E_4}{n\pi\delta}\cosh r_2y_1,\end{aligned}\tag{61}$$

where: $r_1=\pm\sqrt{\delta^2n^2\pi^2-\eta^2/\kappa^2}$, $r_2=\pm\sqrt{\delta^2n^2\pi^2-\eta^2}$, and E_i are the Fourier coefficients given by:

$$\begin{aligned}E_1&=\frac{2\eta^2(n^2\pi^2\delta^2+r_2^2)r_1\cosh r_2\cos n\pi(M_*^+-M_*^-)}{4n^4\pi^4\delta^2r_1r_2\cosh r_1\sinh r_2-n^2\pi^2(n^2\pi^2\delta^2+r_2^2)^2\sinh r_1\cosh r_2},\\E_2&=\frac{2\eta^2(n^2\pi^2\delta^2+r_2^2)r_1\sinh r_2\cos n\pi(M_*^++M_*^-)}{4n^4\pi^4\delta^2r_1r_2\sinh r_1\cosh r_2-n^2\pi^2(n^2\pi^2\delta^2+r_2^2)^2\cosh r_1\sinh r_2},\\E_3&=\frac{-4\eta^2\delta^2r_1\cosh r_1\cos n\pi(M_*^+-M_*^-)}{4n^2\pi^2\delta^2r_1r_2\cosh r_1\sinh r_2-(n^2\pi^2\delta^2+r_2^2)^2\sinh r_1\cosh r_2},\\E_4&=\frac{-4\eta^2\delta^2r_1\sinh r_1\cos n\pi(M_*^++M_*^-)}{4n^2\pi^2\delta^2r_1r_2\sinh r_1\cosh r_2-(n^2\pi^2\delta^2+r_2^2)^2\cosh r_1\sinh r_2}.\end{aligned}\tag{62}$$

The exact solution to the elastic rectangle subject to time-harmonic uniform loading may also be treated similarly. Therefore, leaving out all the algebraic details, the exact formulation for the displacement components are given as:

$$\begin{aligned}u_1^*&=-\frac{\eta(A_*^+-A_*^-)}{2\kappa\sin\frac{\eta}{\kappa}}\cos\frac{\eta}{\kappa}y_1\\&\quad+\frac{\eta(A_*^++A_*^-)}{2\kappa\cos\frac{\eta}{\kappa}}\sin\frac{\eta}{\kappa}y_1,\\u_2^*&=0.\end{aligned}\tag{63}$$

REFERENCES

1. **Babenkova E., Kaplunov J**. (2004), Low-frequency decay conditions for a semi-infinite elastic strip. *Proc. R. Soc. A*., 460(2048), 2153-2169.
2. **Babenkova Y.V., Kaplunov Y.D., Ustinov Y.A**. (2005), Saint-venant's principle in the case of the low-frequency oscillations of a half-strip, *Appl. Math. Mech.*, 69(3), 405-416.
3. **Gregory R.D., Wan F.Y.M**. (1985), On plate theories and Saint-Venant's principle, *International journal of solids and structures*, 21(10), 1005-1024.
4. **Kaplunov J., Prikazchikov D.A., Prikazchikova L.A.**, **Sergushova O.** (2019), The lowest vibration spectra of multi-component structures with contrast material properties, *J. Sound Vib.,* 445, 132-147.

5. **Kaplunov J., Prikazchikov D.A., Rogerson G.A.** (2005), On three-dimensional edge waves in semi-infinite isotropic plates subject to mixed face boundary conditions, *The Journal of the Acoustical Society of America*, 118 (5), 2975-2983.
6. **Kaplunov J., Prikazchikova L., Alkinidri M.** (2021), Antiplane shear of an asymmetric sandwich plate, *Continuum Mechanics and Thermodynamics*, 1-16.
7. **Kaplunov J., Şahin O.** (2020), Perturbed rigid body motions of an elastic rectangle, *Z Angew Math Phys.*, 71(5), 1-15.
8. **Kaplunov J., Shestakova A., Aleynikov I., Hopkins B., Talonov A.** (2015), Low-frequency perturbations of rigid body motions of a viscoelastic inhomogeneous bar, *Mechanics of Time-Dependent Materials*, 19(2), 135-151.
9. **Kudaibergenov A., Nobili A., Prikazchikova L.A.** (2016), On low-frequency vibrations of a composite string with contrast properties for energy scavenging fabric devices, *Journal of Mechanics of Materials and Structures,* 11 (3), 231-243.
10. **Martin T.P., Layman C.N., Moore K.M., Orris G.J.** (2012), Elastic shells with high-contrast material properties as acoustic metamaterial components, *Physical Review B,* 85 (16), 161103.
11. **Milton G.W. and Willis J.R.** (2007), On modifications of Newton's second law and linear continuum elastodynamics, *Proc. R. Soc. A.*, 463 (2079), 855-880.
12. **Prikazchikova L., Aydın Y.E., Erbaş B., Kaplunov J.** (2020), Asymptotic analysis of an anti-plane dynamic problem for a three-layered strongly inhomogeneous laminate, *Math. Mech. Solids,* 25 (1), 3-16.
13. **Qin Y., Wang X., Wang Z.L.** (2008), Microfibre--nanowire hybrid structure for energy scavenging, *Nature,* 451 (7180), 809—813.
14. **Şahin O.** (2019), The effect of boundary conditions on the lowest vibration modes of strongly inhomogeneous beams, *J. Mech. Mater. Struct.*, 14(4), 569-585.
15. **Şahin O., Erbaş B., Kaplunov J., Savsek T.** (2020), The lowest vibration modes of an elastic beam composed of alternating stiff and soft components, *Arch. Appl. Mech.,* 90 (2), 339-352.
16. **Srivastava A., Nemat-Nasser S.** (2012), Overall dynamic properties of three-dimensional periodic elastic composites, *Proc. R. Soc. A.,* 468 (2137), 269-287.
17. **Vigak V.M., Tokovyi Y.V.** (2002), Construction of elementary solutions to a plane elastic problem for a rectangular domain. *International applied mechanics*, 38(7), 829-836.
18. **Viverge K., Boutin C., Sallet F.** (2016), Model of highly contrasted plates ver- sus experiments on laminated glass, *International Journal of Solids and Structures,* 102, 238-258.
19. **Wang X.** (2014), Dynamic behaviour of a metamaterial system with negative mass and modulus, *Int. J. Solids Struct.*, 51(7-8), 1534-1541.
20. **Willis J.R.** (1981), Variational and related methods for the overall properties of composites, In *Advances in applied mechanics*, (21), pp. 1-78, Elsevier.
21. **Willis J.R.** (1981), Variational principles for dynamic problems for inhomogeneous elastic media, *Wave Motion*, 3(1) 1-11.

The authors would like to extend their sincere thanks to J. Kaplunov for the fruitful discussions and his invaluable comments.

sciendo

DOI 10.2478/ama-2021-0013

acta mechanica et automatica, vol.15 no.2 (2021)

PLATE STRUCTURAL ANALYSIS BASED ON A DOUBLE INTERPOLATION ELEMENT WITH ARBITRARY MESHING

Hoang Lan TON-THAT*

*Faculty of Civil Engineering, Ho Chi Minh City University of Architecture,
196 Pasteur, District 3, Ho Chi Minh city, Vietnam.

lan.tonthathoang@uah.edu.vn

received 8 December 2020, revised 8 June 2021, accepted 14 June 2021

Abstract: This paper presents the plate structural analysis based on the finite element method (FEM) using a double interpolation element with arbitrary meshing. This element used in this research is related to the first-order shear deformation theory (FSDT) and the double interpolation procedure. The first stage of the procedure is the same with the standard FEM for the quadrilateral element, but the averaged nodal gradients must be computed for the second stage of this interpolation. Shape functions established by the double interpolation procedure exhibit more continuous nodal gradients and higher-order polynomial contrast compared to the standard FEM when analysing the same mesh. Note that the total degrees of freedom (DOFs) do not increase in this procedure, and the trial solution and its derivatives are continuous across inter-element boundaries. Besides, with controlling distortion factors, the interior nodes of a plate domain are derived from a set of regular nodes. Four practical examples with good results and small errors are considered in this study for showing excellent efficiency for this element. Last but not least, this element allows us to implement the procedure in an existing FEM computer code as well as can be used for nonlinear analysis in the near future.

Key words: mesh irregularity, first-order shear deformation theory, double interpolation procedure

1. INTRODUCTION

The first-order shear deformation theory (FSDT) is simple to implement and is applied for plate-shell structures, but because of finite element analyses, the accuracy of solutions will be strongly dependent on the shear correction factors, as studied by Allman (1984). Hence, the finite element method (FEM) associated with the FSDT shows reasonable results and easy implementation of the standard FEM codes. Because of their better performance, quadrilateral elements are usually used compared with other elements. As referenced in the studies by Ansys (2009), Bui et al. (2014), Ton-That et al. (2020), Nguyen-Xuan et al. (2010), Ton-That (2019), Hoang (2020) and Ton-That (2020), the difficulty in the development of the four-node element related to thin plates will be rectified by using shear correction factors. Furthermore, in the literature, there are many other ways to enhance solutions of the FEM. A new method was proposed by Ahmadian and Farughi (2011) to obtain shape functions for superconvergent element models; by using an inverse method proposed by Ahmadian and Farughi (2011), new formulation for the plane stress element with superconvergent properties was also presented, and the superconvergent element formulations in local co-ordinates were obtained by using inverse strategies proposed by Farughi and Ahmadian (2010). Besides, a novel four-node quadrilateral element with five degrees of freedom (DOFs) per node, SQ4P, based on the FSDT and Chebyshev polynomials was introduced by Hoang-Lan et al. (2021) to analyse plate/shell structures. Another element was improved by using edge-based smoothed strains for analyses of laminated composite plates as in the study by Chau-Dinh et al. (2021). The C^0- type of Shi's third-order shear deformation theory can be applied for linear and nonlinear analyses of composite plates because this theory was taking the advantages and desirable properties of the third-order shear deformation theory such as in paper of Hoang-Lan (2020), etc. The smoothed FEM represented by the SQ4C element as in the studies by Hoang-Lan (2020), Ton-That et al. (2020), Hoang-Lan and Nguyen-Van (2021) or the isogeometric analysis shown in the studies by Tran et al. (2017), Da et al. (2012) and Devarajan et al. (2018, 2020) is reported here. Going back to this paper, the main objective of the present work is to review the influence of mesh irregularity on the results of plate structural analysis based on a double interpolation element that related to the double interpolation procedure. Several desirable characteristics of this procedure are listed here: (*i*) the total number of the DOFs of the whole system does not change, (*ii*) the trial solution and its derivatives are continuous across inter-element boundaries, or in other words, stress in the domain can be transited smoothly element by element as indicated in the studies by Bui et al. (2014), Wu et al. (2012), Zheng et al. (2010) or Ton-That et al. (2020). In this study, all parts of element stiffness matrices are established and then applied to consider the behaviours of plate structures.

The rest of this paper is given as follows. Section 2 briefly presents the formulation of the double interpolation element based on the FSDT and the double interpolation procedure. Section 3 shows the numerical results and some discussions related to this element with mesh irregularity for structural analysis. Finally, some conclusions drawn from the study are presented in the last section.

DOI 10.2478/ama-2021-0013

2. FORMULATION

2.1. The first-order shear deformation theory

The FSDT for plates includes the effect of transverse shear deformations. In the FSDT, the normals to the undeformed middle plane of the plate remain straight but not normal to the deformed middle surface.

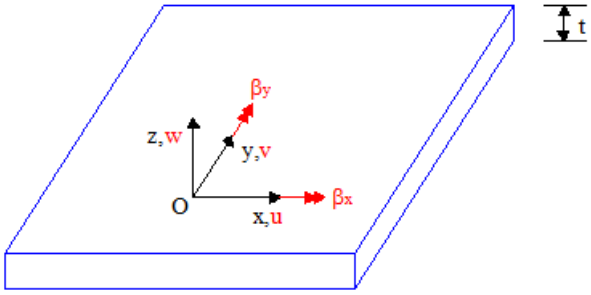

Fig. 1. A plate with positive definition of displacements and rotations

The displacements in the plate can be expressed by the FSDT of Reddy (2007) as follows:

$$u(x,y,z) = u_o(x,y) + z\beta_x \tag{1}$$

$$v(x,y,z) = v_o(x,y) + z\beta_y \tag{2}$$

$$w(x,y,z) = w_o(x,y) \tag{3}$$

where u, v and w are the translational displacements in the x, y and z directions, respectively, u_o, v_o and w_o correspond to the displacements of the middle plane and β_x and β_y are, respectively, the rotation of the mid-plane of x and y axis with positive directions defined in (Fig. 1).

The in-plane strains are obtained as

$$\varepsilon = \begin{bmatrix} u_{o,x} \\ v_{o,y} \\ u_{o,y} + v_{o,x} \end{bmatrix} + z \begin{bmatrix} \beta_{x,x} \\ \beta_{y,y} \\ \beta_{x,y} + \beta_{y,x} \end{bmatrix} = \varepsilon_m + z\varepsilon_b \tag{4}$$

while the transverse shear strains are obtained as

$$\gamma = \begin{bmatrix} \gamma_{xz} \\ \gamma_{yz} \end{bmatrix} = \begin{bmatrix} \beta_x + w_{,x} \\ \beta_y + w_{,y} \end{bmatrix} \tag{5}$$

The linear elastic stress-strain relations in in-plane part are defined for a homogeneous, isotropic material as

$$\boldsymbol{\sigma} = \mathbf{D}\boldsymbol{\varepsilon} \tag{6}$$

where **D** is defined as

$$\boldsymbol{D} = \begin{bmatrix} \boldsymbol{D_m} & \mathbf{0} \\ \mathbf{0} & \boldsymbol{D_b} \end{bmatrix} \tag{7}$$

$$\boldsymbol{D_m} = \frac{Et}{1-\nu^2} \begin{bmatrix} 1 & \nu & 0 \\ \nu & 1 & 0 \\ 0 & 0 & \frac{1-\nu}{2} \end{bmatrix} \tag{8}$$

$$\boldsymbol{D_b} = \frac{Et^3}{12(1-\nu^2)} \begin{bmatrix} 1 & \nu & 0 \\ \nu & 1 & 0 \\ 0 & 0 & \frac{1-\nu}{2} \end{bmatrix} \tag{9}$$

while the linear elastic stress-strain relations in transverse shear part are defined as

$$\boldsymbol{\tau} = \boldsymbol{D_s}\boldsymbol{\gamma} \tag{10}$$

with

$$\boldsymbol{D_s} = \frac{Etk_s}{2(1+\nu)} \begin{bmatrix} 1 & 0 \\ 0 & 1 \end{bmatrix} \tag{11}$$

and k_s = 5/6 is the shear correction factor.

Note that nonlinear relations are not mentioned in this paper.

2.2. The double interpolation procedure

Let x_C be a point in a four-node quadrilateral element with nodes i, j, k and m as shown in Fig. 2. The author denotes S_i, S_j, S_k and S_m elements that share nodes i, j, k and m. The supporting nodes for the point x_C in this quadrilateral element involve all nodes of elements S_i, S_j, S_k and S_m. The support domain of point x_C is much larger than the standard FEM support domain, and the trial solution at point x_C can be written as follows:

$$\breve{u}(x) = \sum_{r=1}^{n_{sp}} \breve{N}_r(x) d_r = \breve{N}(x) d \tag{12}$$

In equation (12), the double interpolation shape function is determined

$$\breve{N}_r = \varphi_i N_r^{[i]} + \varphi_{ix} \bar{N}_{r,x}^{[i]} + \varphi_{iy} \bar{N}_{r,y}^{[i]} + \varphi_j N_r^{[j]} + \varphi_{jx} \bar{N}_{r,x}^{[j]} + \varphi_{jy} \bar{N}_{r,y}^{[j]} + \varphi_k N_r^{[k]} + \varphi_{kx} \bar{N}_{r,x}^{[k]} + \varphi_{ky} \bar{N}_{r,y}^{[k]} + \varphi_m N_r^{[m]} + \varphi_{mx} \bar{N}_{r,x}^{[m]} + \varphi_{my} \bar{N}_{r,y}^{[m]} \tag{13}$$

where d_r denotes the nodal displacement vector, while $N_r^{[i]}$ is the shape function with respect to node i, and n_{sp} is the total number of the supporting nodes in regard to the point x_C.

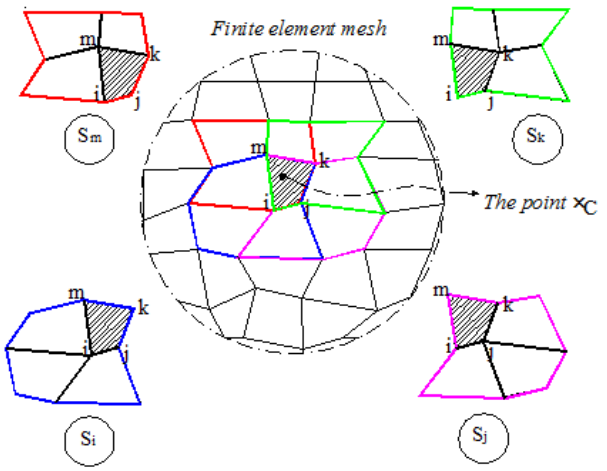

Fig. 2. Schematic sketch of the double interpolation procedure for a quadrilateral element in 2D

The formulation of the average derivative of the shape functions at node i is given (similar for other nodes).

$$\bar{N}_{r,x}^{[i]} = \sum_{e \in S_i} (\omega_e N_{r,x}^{[i][e]}) \tag{14}$$

$$\bar{N}_{r,y}^{[i]} = \sum_{e \in S_i} (\omega_e N_{r,y}^{[i][e]}) \tag{15}$$

In equations (14) and (15), the term $N_{r,x}^{[i][e]}$is the derivative of $N_r^{[i]}$ computed in element *e*, and ω_e is the weight function of element $e \in S_i$, which is defined

$$\omega_e = \frac{A_e}{\sum_{\bar{e}\in S_i} A_{\bar{e}}} \tag{16}$$

A_e being the area of the element *e*. In equation (13), the functions φ_i, φ_{ix} and φ_{iy} forming the polynomial basis associated with node *i* must satisfy the following conditions

$$\begin{aligned}
&\varphi_i(x_r) = \delta_{ir} \quad \varphi_{i,x}(x_r) = 0 \quad \varphi_{i,y}(x_r) = 0\\
&\varphi_{ix}(x_r) = 0 \quad \varphi_{ix,x}(x_r) = \delta_{ir} \quad \varphi_{ix,y}(x_r) = 0\\
&\varphi_{iy}(x_r) = 0 \quad \varphi_{iy,x}(x_r) = 0 \quad \varphi_{iy,y}(x_r) = \delta_{ir}
\end{aligned} \tag{17}$$

with *r* is any one of the indices *i, j, k* and *m*

$$\delta_{ir} = \begin{cases} 1 & if \quad i = r \\ 0 & if \quad i \neq r \end{cases} \tag{18}$$

The above conditions have to be applied in a similar manner to other functions, i.e., $\varphi_j, \varphi_{jx}, \varphi_{jy}, \varphi_k, \varphi_{kx}, \varphi_{ky}, \varphi_m, \varphi_{mx}$ and φ_{my}. These polynomial basis functions φ_i, φ_{ix} and φ_{iy} for the quadrilateral element are given

$$\begin{aligned}
\varphi_i &= R_i + R_i^2 R_j + R_i^2 R_k + R_i^2 R_m\\
&\quad - R_i R_j^2 - R_i R_k^2 - R_i R_m^2
\end{aligned} \tag{19}$$

$$\begin{aligned}
\varphi_{ix} &= -(x_i - x_j)(R_i^2 R_j + 0.5 R_i R_j R_k + 0.5 R_i R_j R_m)\\
&\quad -(x_i - x_k)(R_i^2 R_k + 0.5 R_i R_k R_j + 0.5 R_i R_k R_m)\\
&\quad -(x_i - x_m)(R_i^2 R_m + 0.5 R_i R_m R_j + 0.5 R_i R_m R_k)
\end{aligned} \tag{20}$$

$$\begin{aligned}
\varphi_{iy} &= -(y_i - y_j)(R_i^2 R_j + 0.5 R_i R_j R_k + 0.5 R_i R_j R_m)\\
&\quad -(y_i - y_k)(R_i^2 R_k + 0.5 R_i R_k R_j + 0.5 R_i R_k R_m)\\
&\quad -(y_i - y_m)(R_i^2 R_m + 0.5 R_i R_m R_j + 0.5 R_i R_m R_k)
\end{aligned} \tag{21}$$

Other functions can be calculated in the same manner by using Eqs (19)–(21) with a circulatory permutation of indices *i, j, k* and *m*. Besides, R_i, R_j, R_k and R_m are the area coordinates of the point x_C in the quadrilateral element with four nodes *i, j, k* and *m*; for more details, see in Bui et al. (2014), Wu et al. (2012), Zheng et al. (2010) and Ton-That et al. (2020). These shape functions are complete polynomials, satisfy properties of the partition of unity and possess Kronecker's delta function property.

2.3. The double interpolation element

With five degrees of freedom for one node, the in-plane strains at an arbitrary point x_C can be obtained as follows

$$\boldsymbol{\varepsilon}_{\mathbf{m}}(x_C) = \mathbf{B}_{\mathbf{m}}(x_C)\mathbf{q} \tag{22}$$

$$\boldsymbol{\varepsilon}_{\mathbf{b}}(x_C) = \mathbf{B}_{\mathbf{b}}(x_C)\mathbf{q} \tag{23}$$

in which

$$q_i = [u_i \quad v_i \quad w_i \quad \beta_{xi} \quad \beta_{yi}]^T \tag{24}$$

$\mathbf{B}_{\mathbf{m}}(x_C) =$

$$\begin{bmatrix}
\breve{N}_{1,x} & 0 & 0 & 0 & 0 & \dots & \breve{N}_{n_{sp},x} & 0 & 0 & 0 & 0\\
0 & \breve{N}_{1,y} & 0 & 0 & 0 & \dots & 0 & \breve{N}_{n_{sp},y} & 0 & 0 & 0\\
\breve{N}_{1,y} & \breve{N}_{1,x} & 0 & 0 & 0 & \dots & \breve{N}_{n_{sp},y} & \breve{N}_{n_{sp},x} & 0 & 0 & 0
\end{bmatrix}_{3\times 5n_{sp}} \tag{25}$$

$\mathbf{B}_{\mathbf{b}}(x_C) =$

$$\begin{bmatrix}
0 & 0 & 0 & \breve{N}_{1,x} & 0 & \dots & 0 & 0 & 0 & \breve{N}_{n_{sp},x} & 0\\
0 & 0 & 0 & 0 & \breve{N}_{1,y} & \dots & 0 & 0 & 0 & 0 & \breve{N}_{n_{sp},y}\\
0 & 0 & 0 & \breve{N}_{1,y} & \breve{N}_{1,x} & \dots & 0 & 0 & 0 & \breve{N}_{n_{sp},y} & \breve{N}_{n_{sp},x}
\end{bmatrix}_{3\times 5n_{sp}} \tag{26}$$

with n_{sp} is the total number of the supporting nodes in regard to the point x_C. The transverse shear strains are also expressed by

$$\boldsymbol{\gamma}(x_C) = \mathbf{B}_{\mathbf{s}}(x_C)\mathbf{q} \tag{27}$$

where

$\mathbf{B}_{\mathbf{s}}(x_C) =$

$$\begin{bmatrix}
0 & 0 & \breve{N}_{1,x} & \breve{N}_1 & 0 & \dots & 0 & 0 & \breve{N}_{n_{sp},x} & \breve{N}_{n_{sp}} & 0\\
0 & 0 & \breve{N}_{1,y} & 0 & \breve{N}_1 & \dots & 0 & 0 & \breve{N}_{n_{sp},y} & 0 & \breve{N}_{n_{sp}}
\end{bmatrix}_{2\times 5n_{sp}} \tag{28}$$

The double interpolation element stiffness matrix is then written as

$$\begin{aligned}
\mathbf{K}^{el} &= \mathbf{K_m} + \mathbf{K_m} + \mathbf{K_m} = \int_\Omega \mathbf{B_m^T D_m B_m} d\Omega\\
&+ \int_\Omega \mathbf{B_m^T D_m B_m} d\Omega + \int_\Omega \mathbf{B_m^T D_m B_m} d\Omega
\end{aligned} \tag{29}$$

For static analysis

$$\mathbf{Kq} = \mathbf{F} \tag{30}$$

with **K** is the global stiffness matrix and **F** is the load vector which is given as follows

$$\mathbf{F} = \int_\Omega \mathbf{N}^T \mathbf{p} d\Omega \tag{31}$$

in which **N** is the shape functions of standard quadrilateral element.

For free vibration analysis

$$(\mathbf{K} - \omega^2 \mathbf{M})\mathbf{q} = 0 \tag{32}$$

with ω is the natural frequency and **M** is the global mass matrix which is defined by

$$\mathbf{M} = \int_\Omega \mathbf{N}^T \mathbf{m} \mathbf{N} d\Omega \tag{33}$$

$$\mathbf{m} = \rho t \begin{bmatrix}
1 & 0 & 0 & 0 & 0\\
0 & 1 & 0 & 0 & 0\\
0 & 0 & 1 & 0 & 0\\
0 & 0 & 0 & \frac{t^2}{12} & 0\\
0 & 0 & 0 & 0 & \frac{t^2}{12}
\end{bmatrix} \tag{34}$$

2.4. The mesh irregularity procedure

The domain of the plate structure is created by the double interpolation elements related to irregular interior nodes. These interior nodes are derived from a set of regular nodes by using a controlling distortion factor *s*. The coordinates of an irregular mesh are obtained by the following expressions:

DOI 10.2478/ama-2021-0013

$$x' = x + r_c \times \Delta x \quad (35)$$

$$y' = y + r_c \times \Delta y \quad (36)$$

where r_c is a computer-generated random number between -1.0 and 1.0; Δx, Δy are initial regular element sizes in the *x*- and *y*-directions, respectively and *s* is used to control the shapes of the distorted elements. (Fig. 3) illustrates the mesh irregularity with three values 0.1, 0.2 and 0.3 of *s*.

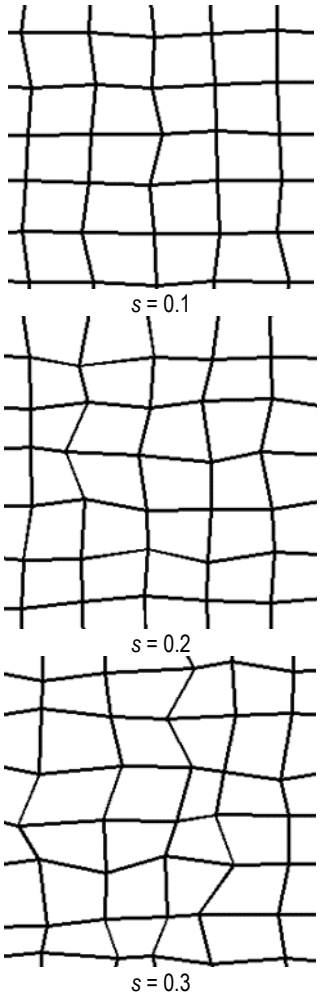

Fig. 3. Typical irregular meshes of 18 × 18 with various distortion factor *s*

3. SOLUTIONS AND DISCUSSIONS

The double interpolation element will be used through numerical examples. The SI units are used in this paper.

3.1. The Cook's membrane

The Cook's membrane problem is studied in this section with E = 1.0, v = 0.499 and thickness t = 1, and this model is shown in Fig. 4. Under plane stress conditions, the reference value of the vertical displacement at the centre of the tip section (point C) in Fredriksson et al. (2004) is 23.96. Here, the double interpolation element is compared with other elements listed in Tab. 1 as well as in Fig. 5: Allman's membrane triangle element (AT) by author Allman (1984), assumed stress hybrid methods such as P-S element by Pian et al. (1984), HQM/HQ4 element by Xie (2005) and node-based smoothed NSQ4 element by Xuan (2008). Furthermore, the normal stress field will be also plotted in Fig. 4.

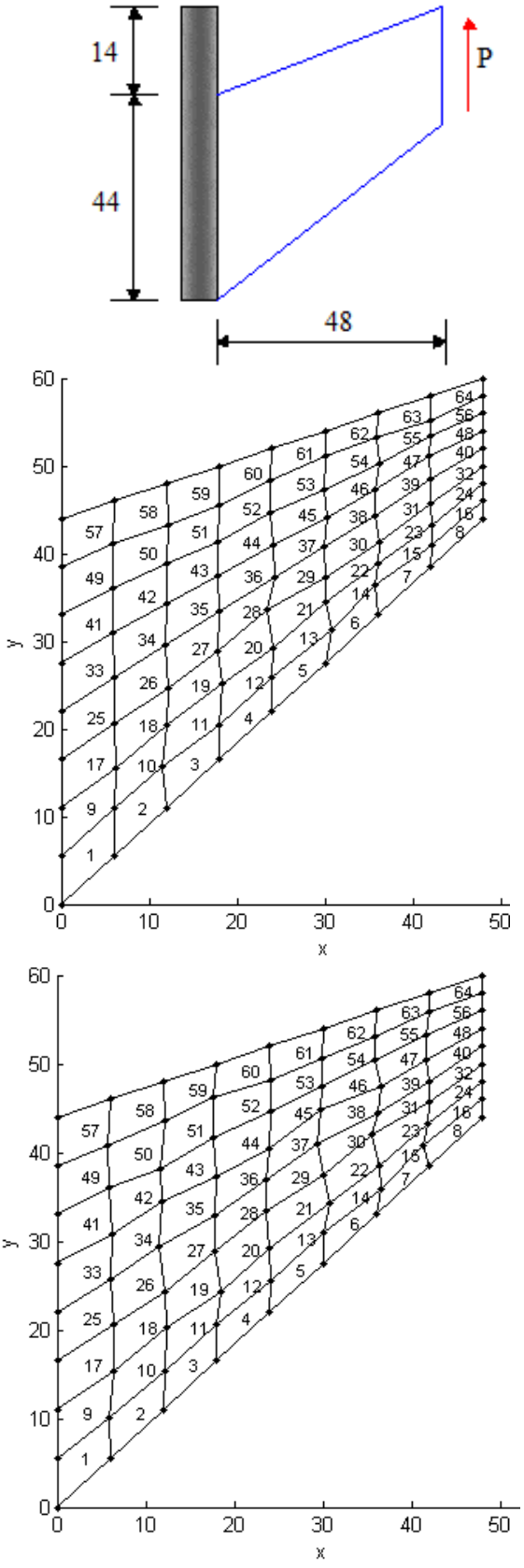

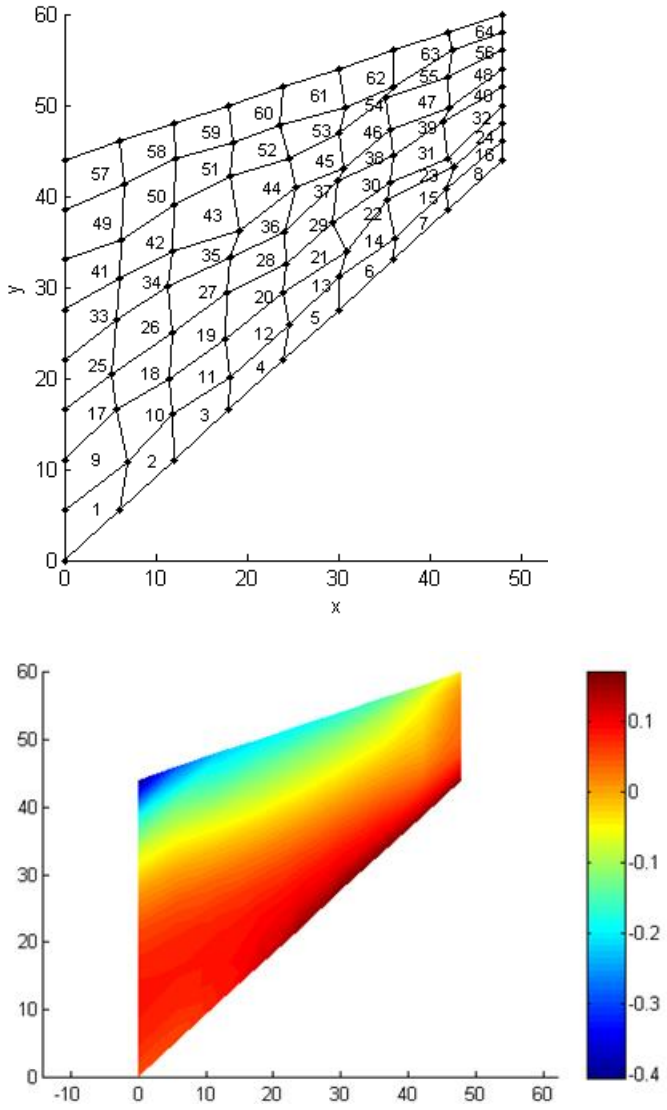

Fig. 4. Typical irregular meshes of 8×8 with various distortion factor *s* (0.1; 0.2 and 0.3) and the normal stress field

Tab. 1. Results of displacement tip (at C) for Cook's problem

Element	Displacement tip				
	2x2	4x4	6x6	8x8	10x10
AT	19.67	22.41	–	23.45	–
P-S	21.13	23.02	–	23.69	–
HQM/HQ4	21.35	23.04	–	23.69	–
NSQ4	24.69	25.38	–	24.51	–
Paper (s = 0)	15.24	22.23	23.40	23.76	23.91
Paper (s = 0.1)	14.31	21.87	23.36	23.62	23.90
Paper (s = 0.2)	14.98	22.17	23.39	23.72	23.88
Paper (s = 0.3)	15.34	22.04	23.04	23.75	23.81
Ref (Exact solutiion)	23.96	23.96	23.96	23.96	23.96

AT, Allman's membrane triangle element, P-S, element based on polynomial stress, HQM/HQ4, hybrid macro element, NSQ4, node-based smoothed element.

Based on the comparison results as below, we can see that (*i*) when changing the value of *s*, the results obtained by the proposed element do not have big differences or, in other words, these results achieved stability with different distorted meshes, and (*ii*) when the total number of elements increases beyond 60, these results also converge to the exact result better than the other elements.

Additionally, it is observed that the stress obtained by the proposed element is continuous and smooth, whereas the standard FEM does not guarantee such smoothness and continuity.

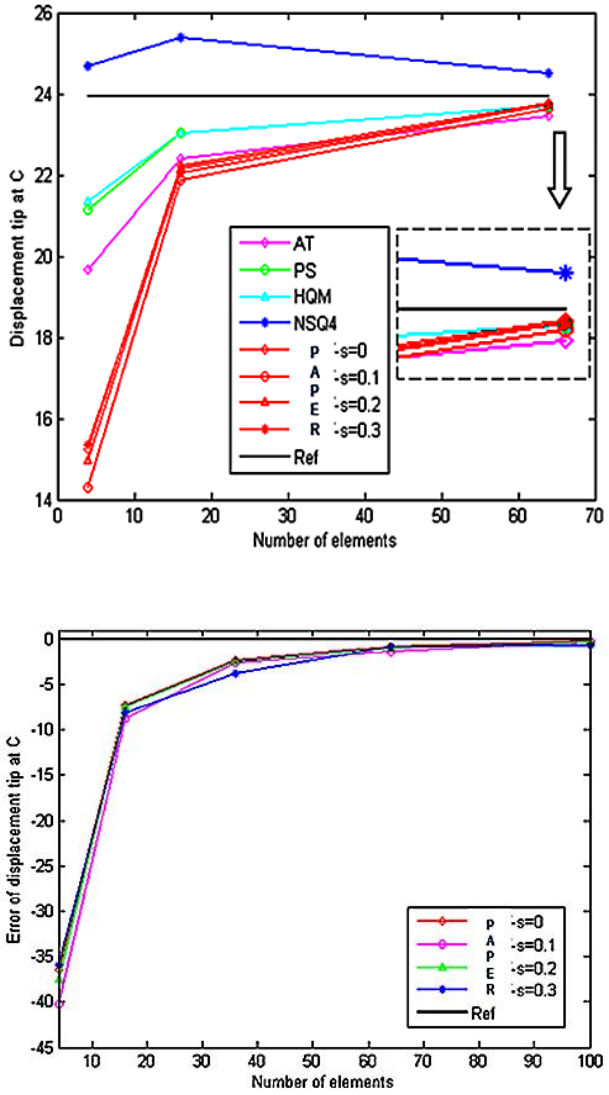

Fig. 5. The comparison of displacements at point C and error of these displacements with exact solution.

3.2. The L-shape plate subjected to in-plane load

Next, consider a L-shaped domain with applied tractions, boundary conditions and arbitrary meshing, as shown in Fig. 6. The parameters of the structure are as follows: Young's modulus $E = 1.0$, Poisson's ratio $v = 0.3$, length $a = 50$ and thickness $t = 1$. The reference value of the displacement at point A based on Ansys software from Ansys (2009, Canonsburg, PA 15317, USA) is 2.328,. The solutions of a double interpolation element related to $s = 0$; 0.1; 0.2 and 0.3 are in good agreement with Ansys solutions as depicted in Tab. 2. Besides, the normal stress field will be also plotted in Fig. 6.

DOI 10.2478/ama-2021-0013

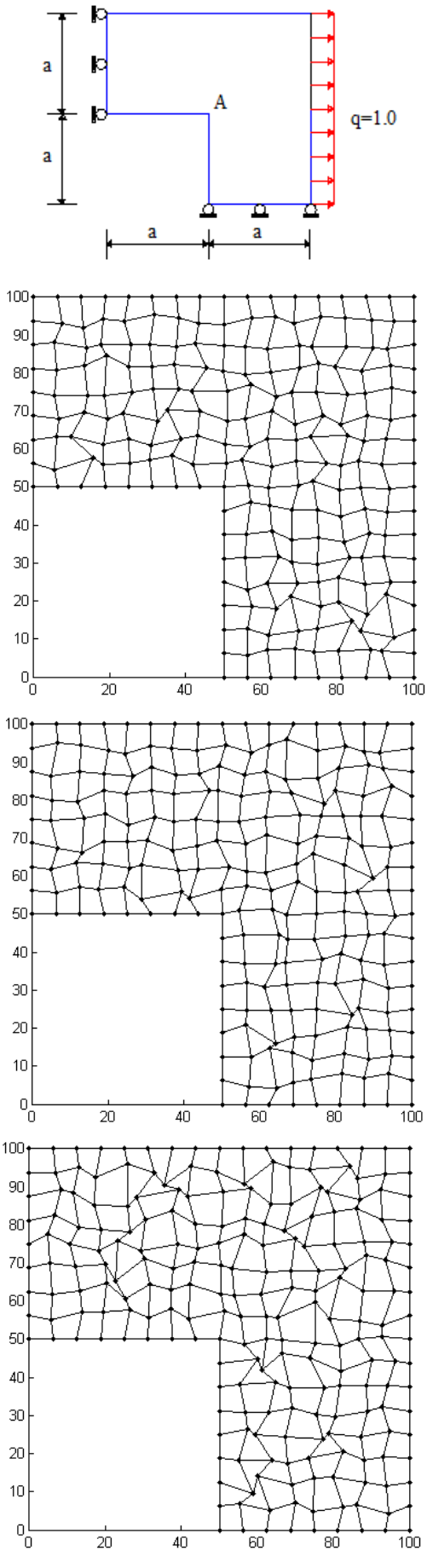

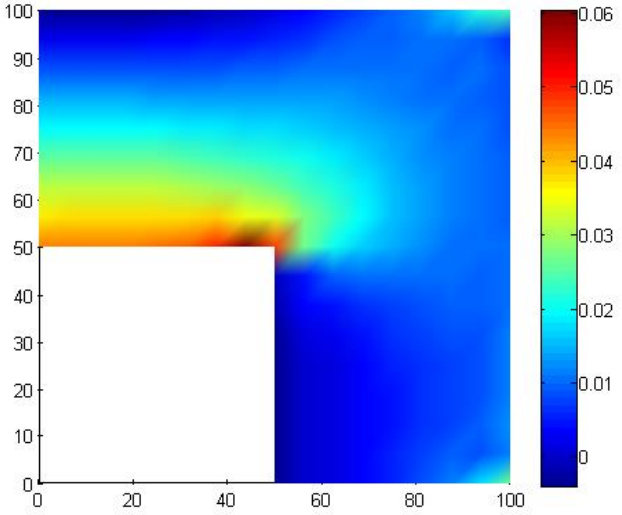

Fig. 6. Typical irregular meshes with various distortion factor *s* (0.1; 0.2 and 0.3) and the normal stress field

Tab. 2. Results of displacement u_A at point A for L-shape problems

u_A	Paper *s* = 0	*s* = 0.1	*s* = 0.2	*s* = 0.3	Ansys
	2.327	**2.323**	**2.319**	**2.317**	**2.328**
Error (%)	0.043	0.215	0.386	0.472	

Apparently, it is again shown that the normal stress achieved by the proposed element is continuous and smooth through all boundaries of the element.

3.3. The square plate subjected to uniformly distributed and sinusoidal load

The clamped square plate is considered in this section, as shown in Fig. 7.

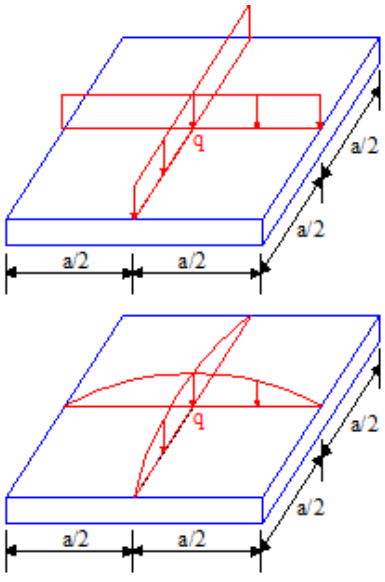

Fig. 7. A clamped square plate under uniformly distributed load and sinusoidal load

Following material properties of this isotropic plates are used: E = 210 GPa and v = 0.3. When subjected to uniformly distributed and sinusoidal load, the author's result obtained for the central displacement will now be compared and discussed with the corresponding results of the exponential shear deformation theory (ESDT) by Sayyad et al. (2012), the higher-order shear deformation theory (HSDT) by Reddy (1984), the trigonometric shear deformation theory (TSDT) by Ghugal et al. (2010), the FSDT by Mindlin (1951) and the classical plate theory (CPT) by Kirchhoff (1850), as shown in Tab. 3. The numerical result is presented in the following non-dimensional form $\bar{w} = 100Ew/[q(a/t)^4]$ and shows good agreement with others.

Tab. 3. Comparison of non-dimensional transverse displacement in an isotropic square plate subjected to uniformly distributed and sinusoidal load

Theory	Model	$\bar{w}$ (Uniform load)		$\bar{w}$ (Sinusoidal load)	
		a/t=4	*a/t*=10	*a/t*=4	*a/t*=10
Sayyad	ESDT	5.816	4.658	3.748	2.954
Reddy	HSDT	5.869	4.666	3.787	2.961
Ghugal	TSDT	5.680	4.625	3.653	2.933
Mindlin	FSDT	5.633	4.670	3.626	2.934
Kirchhoff	CPT	4.436	4.436	2.803	2.802
Paper (s = 0)	FSDT	5.626	4.633	3.782	2.913
Paper (s = 0.1)	FSDT	5.601	4.644	3.771	2.885
Paper (s = 0.2)	FSDT	5.583	4.556	3.734	2.889
Paper (s = 0)	FSDT	5.9861	8.5760	8.5760	
Paper (s = 0.1)	FSDT	5.9933	8.5822	8.5873	
Paper (s = 0.2)	FSDT	6.0182	8.6125	8.6165	
Paper (s = 0.3)	FSDT	6.0331	8.6396	8.6557	
Exact		5.9990	8.5680	8.5680	
DSG3		5.7616	7.9935	8.0525	
ES-DSG3		5.7250	7.9211	7.9627	
Paper (s = 0)		5.7396	7.9787	7.9787	
Paper (s = 0.1)		5.7402	7.9802	7.9803	
Paper (s = 0.2)		5.7419	7.9822	7.9839	
Paper (s = 0.3)		5.7449	7.9879	7.9901	
Exact		5.7100	7.8800	7.8800	

CPT, classical plate theory; ESDT, exponential shear deformation theory; FSDT, first-order shear deformation theory; HSDT, higher-order shear deformation theory; TSDT, trigonometric shear deformation theory.

3.4. Free vibration analysis of the square plate

In this last section, author investigates the efficiency of the double interpolation element for analyzing natural frequencies of square plates. The plate has clamped edges with length a and thickness t. The material parameters are E = 2.0 × 10^{11}, v = 0.3 and ρ = 8000 as follows Nguyen-Xuan et al. (2010). The plate is modeled with 16 elements per each side.

A non-dimensional frequency parameter $\omega = (\omega^2 \rho a^4 t/D)^{1/4}$ where $D = Et^3/(12(1-\nu^2))$ is often used and then compared to analytical solutions and other numerical results which are available in the literature Nguyen-Xuan et al. (2010) and Robert (1979). Tab. 4 shows the first three values of based on the double interpolation element.

Tab. 4. A non-dimensional frequency parameter of a CCCC square plate

t/a	Elements	Mode sequence number		
		1	2	3
0.005	DSG3	6.1786	8.8759	9.0680
	ES-DSG3	6.0355	8.6535	8.7081

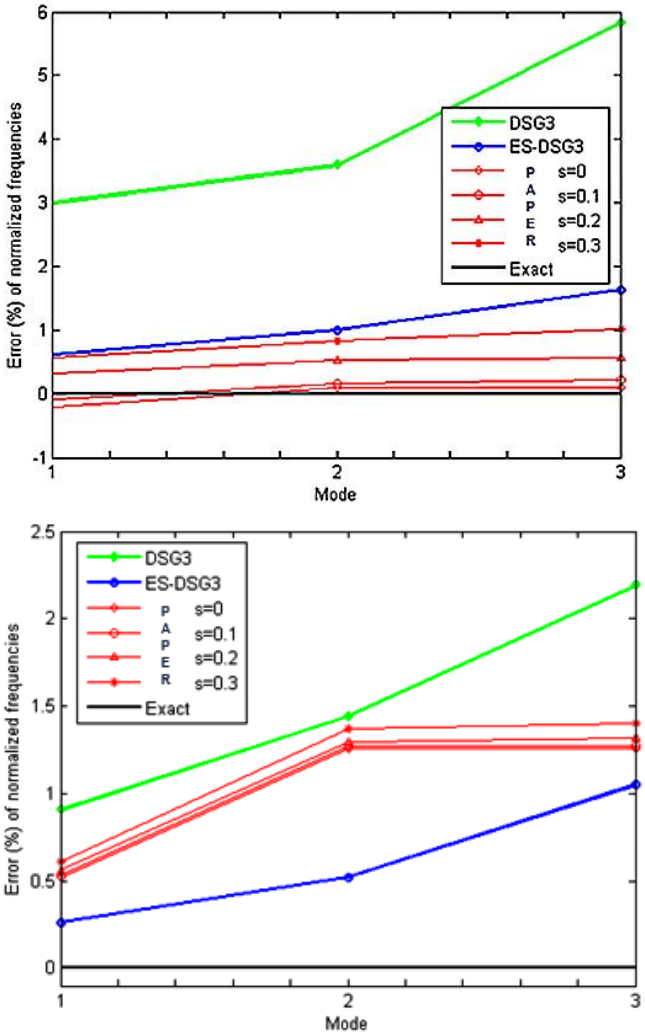

Fig. 8. Error of the normalized frequencies with *t/a* = 0.005 and *t/a* = 0.1

DOI 10.2478/ama-2021-0013

As shown in Fig. 8 with *t/a* = 0.005, the double interpolation element is almost better than the DSG3 and ES-DSG3 elements and gives a small error with the exact solution of Robert (1979) for all frequencies examined in this problem. Similarly, in Fig. 8 with *t/a* = 0.1, the paper's results are better than the DSG3's results for all frequencies. Besides, Fig. 9 shows the first mode shapes with the stability of paper's results related to the small errors.

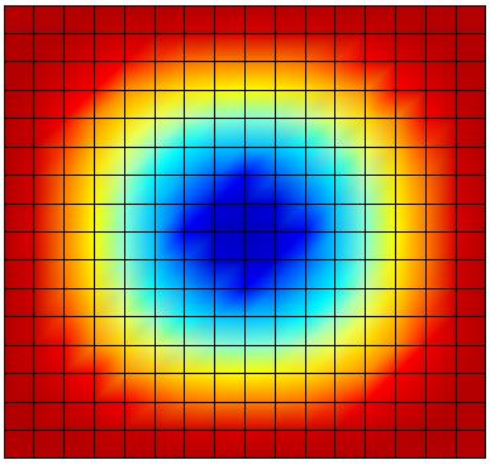

Mode 1_s = 0 (5.9861)

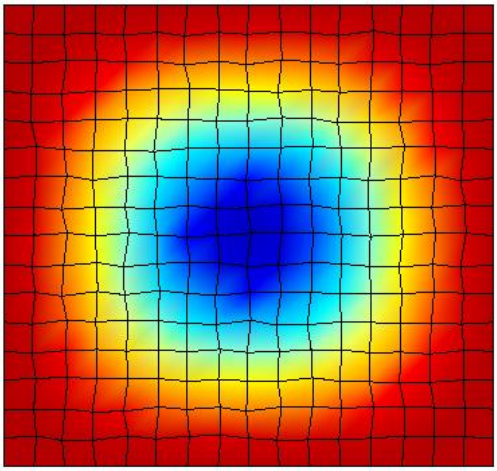

Mode 1_s = 0.1 (5.9933)

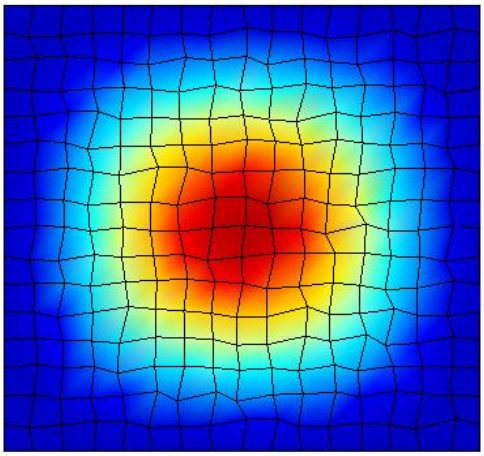

Mode 1_s = 0.2 (6.0182)

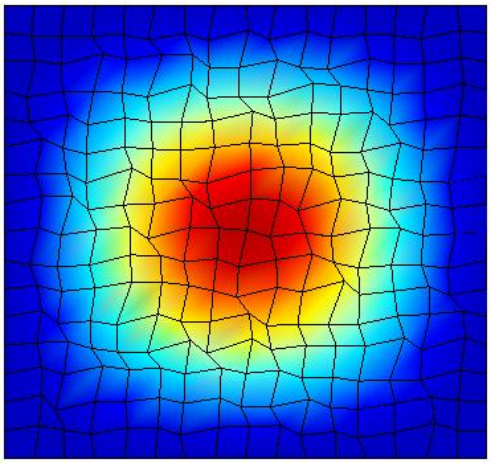

Mode 1_s = 0.3 (6.0331)

Fig. 9. The first mode shapes of clamped square plate with *t/a* = 0.005 and *s* = 0, 0.1, 0.2 and 0.3

4. CONCLUSION

This paper presented the stability of solutions when using mesh irregularity for structural analysis based on the FEM and the double interpolation elements. Due to the framework of the FSDT and the double interpolation procedure, the double interpolation element becomes an efficient flat quadrilateral element for structural analysis. The shape functions of this element are higher-order polynomials and posses the Kronecker-delta function property, which permits a straightforward imposition of the essential boundary conditions. Moreover, with the influence of neighbouring elements on the element under consideration, the errors will be reduced as well as the results will be stable and less affected by the mesh. Finally, the results obtained in this paper are also compared with other available numerical results to illustrate the robustness of this element as stated above.

REFERENCES

1. **Ahmadian H., Faroughi S.** (2011a), Development of super-convergent plane stress element formulation using an inverse approach, *Finite Elements in Analysis and Design*, 47(7), 796-803.
2. **Ahmadian H., Faroughi S.** (2011b), Shape functions of superconvergent finite element models, *Thin-Walled Structures*, 49(9), 1178-1183.
3. **Allman D. J.** (1984), A compatible triangular element including vertex rotations for plane elasticity analysis, *Computers and Structures*, 19(1), 1-8.
4. **Ansys** (2009), ANSYS Workbench User's Guide, *ANSYS, Inc.: Canonsburg, PA 15317, USA*.
5. **Bui T. Q., Vo D. Q., Zhang C., Nguyen D. D.** (2014), A consecutive-interpolation quadrilateral element (CQ4): Formulation and applications, *Finite Elements in Analysis and Design*, 84, 14-31.
6. **Chau-Dinh T., Trung-Kien N., Nguyen-Van H., Ton-That H. L.** (2021), A MITC3+ element improved by edge-based smoothed strains for analyses of laminated composite plates using the higher-order shear deformation theory, *Acta Mechanica*, 232(2), 389-422.
7. **Da V., Beirao L., Annalisa B., Lovadina C., Martinelli M., Sangalli G.** (2012), An isogeometric method for the Reissner Mindlin plate bending problem, *Computer Methods in Applied Mechanics and Engineering*, 209, 45-53.

8. **Devarajan B., Kapania R. K.** (2020), Thermal buckling of curvilinearly stiffened laminated composite plates with cutouts using isogeometric analysis, *Composite Structures*, 238, 111881.
9. **Faroughi S., Ahmadian H.** (2010), Shape functions associated with inverse element formulations, *Proceedings of the Institution of Mechanical Engineers, Part C: Journal of Mechanical Engineering Science*, 225(2), 304-311.
10. **Fredriksson M., Ottosen N. S.** (2004), Fast and accurate 4-node quadrilateral, *International Journal for Numerical Methods in Engineering*, 61(11), 1809-1834.
11. **Ghugal Y. M., Sayyad A. S.** (2010), Free vibration of thick orthotropic plates using trigonometric shear deformation theory, *Latin American Journal of Solids and Structures*, 8, 229-243.
12. **Hoang T. T. L.** (2020), A new C0 third-order shear deformation theory for the nonlinear free vibration analysis of stiffened functionally graded plates, *Facta Universitatis, Series: Mechanical Engineering*, Online first.
13. **Hoang-Lan T. T.** (2020), A Combined Strain Element to Functionally Graded Structures in Thermal Environment, *Acta Polytechnica*, 60(6), 528-539.
14. **Hoang-Lan T. T.** (2020), The linear and nonlinear bending analyses of functionally graded carbon nanotube-reinforced composite plates based on the novel four-node quadrilateral element, *European Journal of Computational Mechanics*, 29(1), 139-172.
15. **Hoang-Lan T. T., Nguyen-Van H.** (2021), A combined strain element in static, frequency and buckling analyses of laminated composite plates and shells, *Periodica Polytechnica Civil Engineering*, 65(1), 56-71.
16. **Hoang-Lan T. T., Nguyen-Van H., Chau-Dinh T.** (2021), A novel quadrilateral element for analysis of functionally graded porous plates/shells reinforced by graphene platelets, *Archive of Applied Mechanics*.
17. **Kirchhoff G. R.** (1850), Uber das Gleichgewicht und die Bewegung einer elastischen Scheibe, *Journal fur die reine und angewandte Mathematik*, 40, 51-88.
18. **Miglani J., Devarajan B., Kapania R. K.** (2018), Thermal buckling analysis of periodically supported composite beams using Isogeometric analysis, *AIAA/ASCE/AHS/ASC Structures, Structural Dynamics, and Materials Conference*, 1224.
19. **Mindlin R. D.** (1951), Influence of rotatory inertia and shear on flexural motions of isotropic, elastic plates, *ASME Journal of Applied Mechanics*, 18, 31-38.
20. **Nguyen-Xuan H., Liu G. R., Thai-Hoang C., Nguyen-Thoi T.** (2010), An edge-based smoothed finite element method (ES-FEM) with stabilized discrete shear gap technique for analysis of Reissner–Mindlin plates, *Computer Methods in Applied Mechanics and Engineering*, 199(9), 471-489.
21. **Pian T. H. H., Sumihara K.** (1984), Rational approach for assumed stress finite elements, *International Journal for Numerical Methods in Engineering*, 20(9), 1685-1695.
22. **Reddy J. N.** (1984), A simple higher-order theory for laminated composite plates, *Journal of Applied Mechanics*, 51(4), 745-752.
23. **Reddy J. N.** (2007), Theory and Analysis of Elastic Plates and Shells: *CRC Press*.
24. **Robert D. B.** (1979), Formulas for natural frequency and mode shape, *New York: Van Nostrand Reinhold*.
25. **Sayyad A. S., Ghugal Y. M.** (2012), Bending and free vibration analysis of thick isotropic plates by using exponential shear deformation theory, *Applied and Computational Mechanics*, 6(1), 65-82.
26. **Ton T. H. L.** (2019), Finite element analysis of functionally graded skew plates in thermal environment based on the new third-order shear deformation theory, *Journal of Applied and Computational Mechanics*, 6(4), 1044-1057.
27. **Ton T. H. L.** (2020), A novel quadrilateral element for dynamic response of plate structures subjected to blast loading, *Journal of Applied and Computational Mechanics,* 6, 1314-1323.
28. **Ton T. H. L.** (2020), Improvement on eight-node quadrilateral element (IQ8) using twice-interpolation strategy for linear elastic fracture mechanics, *Engineering Solid Mechanics*, 8(4), 323-336.
29. **Ton-That H. L., Nguyen-Van H., Chau-Dinh T.** (2020), Nonlinear Bending Analysis of Functionally Graded Plates Using SQ4T Elements based on Twice Interpolation Strategy, *Journal of Applied and Computational Mechanics*, 6(1), 125-136.
30. **Ton-That H. L., Nguyen-Van H., Chau-Dinh T.** (2020), Static and buckling analyses of stiffened plate/shell structures using the quadrilateral element SQ4C, *Comptes Rendus. Mécanique, 348(4), 285-305.*
31. **Tran L. V., Wahab M. A., Seung-Eock K.** (2017), An isogeometric finite element approach for thermal bending and buckling analyses of laminated composite plates, *Composite Structures*, 179, 35-49.
32. **Wu S. C., Zhang W. H., Peng X., Miao B. R.** (2012), A twice-interpolation finite element method (TFEM) for crack propagation problems, *International Journal of Computational Methods*, 9(4), 1250055.
33. **Xie X. P.** (2005), An accurate hybrid macro-element with linear displacements, *Communications in Numerical Methods in Engineering*, 21(1), 1-12.
34. **Xuan H. N.** (2008), A strain smoothing method in finite elements for structural analysis, *PhD thesis, University of Liege, Belgium*.
35. **Zheng C., Wu S. C., Tang X. H., Zhang J. H.** (2010), A novel twice-interpolation finite element method for solid mechanics problems, *Acta Mechanica Sinica*, 26(2), 265-278.

DOI 10.2478/ama-2021-0014

BIRDS STRIKE – IMPACT ON THE SAFETY OF CIVIL AIRCRAFT OPERATIONS IN POLAND IN 2008–2018

Włodzimierz BALICKI[*], Paweł GLOWACKI[*], Leszek LOROCH[*]

[*]Łukasiewicz Research Network – Institute of Aviation, Poland, 02-256 Warsaw, al. Krakowska 110/114, Poland

Wlodzimierz.Balicki@ilot.lukasiewicz.gov.pl, Pawel.Glowacki@ilot.lukasiewicz.gov.pl, Leszek.Loroch@ilot.lukasiewicz.gov.pl

received 1 May 2020, revised 8 June 2021, accepted 14 June 2021

Abstract: The authors assessed the real threat to civil aircraft traffic in Poland resulting from bird strikes. It was found that in the period 2013–2018, the probability of such events increased by four times. Data for this work were downloaded from the ECCAIRS database maintained by the Civil Aviation Authority. Air traffic events have been collected for several years in this database. An assessment of the energy of bird collision with the aircraft, resulting from the bird's mass and relative speed of movement, was also presented. Ways to minimise the risk of collision were described by introducing crew warning systems and means to scare off birds from the airport grounds. The method of testing the resistance of turbine engines to the foreign body's absorption was also shown, as well as design methods for increasing the engine resistance to bird strikes.

Key words: air transport, air traffic safety, aviation events, bird strike

1. INTRODUCTION

Birds and planes move in the same environment; this is the reason for the most frequent incidents occurring near airports. The first recorded bird collision report is from Orville Wright. His plane collided with a blackbird in Dayton in 1905. The first recorded casualty was that of pilot Calbraith Rogers, whose plane drowned in the sea after the collision with a seagull (3 April 1912 on Long Beach – California). The most tragic bird strike accident so far, claiming the lives of 62 passengers, was that of the Lockheed Electra L-188 plane, which crashed during take-off from Boston airport when three engines (Allison 501D) failed after a collision with a herd of starlings. The most famous case of a bird strike involved US Airways Flight 1549 in 2009 (popularly known as the 'Miracle on the Hudson'). Six minutes after take-off, the aircraft (Airbus A320-214) lost power in both engines as a result of a collision with a flock of wild geese, which caused damage to its engines and forced the pilot to perform an emergency landing on the Hudson River. Thanks to the pilot's skills, all the passengers survived the disaster (Fortońska, 2018, Korte, 2019).

The increase in the number of air operations in the world, the change in bird migration habits, and faster and quieter turbine-powered aircraft, which give birds less time to get off the flight line of an aircraft, are some of the causes for the increase observed in the number of collisions. The Federal Aviation Administration (FAA) in its study (1990–1999) reported that, while the number of reported bird collisions has increased rapidly, the number of reported harmful ones has decreased since 2000. The number of reported collisions occurring in US airspace has increased by 144% from 5,872 in 2000 to 14,349 in 2017. The number of serious incidents, however, fell by 16%, from 741 to 625. This decrease was most evident for commercial aircraft in the airport environment (at <1,500 ft above ground level). On average, there are 8–19 collisions per 10,000 flights, depending on the world region. The number of these cases depends on the season: in the northern hemisphere, the highest number of incidents occurs in August, September and October (40% of the annual number). The reason is migration of birds. The probability of a collision is significantly influenced by the flight altitude: as much as 80% is for flights below 1,000 feet (take-off, approach, moving flight). However, similar events have not decreased in the case of general aviation (GA) aircraft (Directive 2003/42/EC). These phenomena have attracted the interest of insurance companies, which pay significant compensation to the heirs of crash victims, as well as to airlines bearing the costs of aircraft maintenance and decommissioning. The average cost of removing the effects of a collision between a passenger aircraft and birds is US$235,000 if damage is detected and US$22,000 if there is no damage (inspection costs, cancelled flight, etc.). The seriousness of these issues led the International Civil Aviation Organization (ICAO) to establish the Bird Strike Committee Europe (Matijaca, 2001, 2008).

In Poland, there is also a significant increase in the number of air events caused by collisions with birds; however, no serious effects resulting from them were observed.

1.1. Methodology of analysis

The number of aircraft registered in Poland is growing (cf. Tab. 1 and Fig. 1). Some regularity is maintained as follows: there are 10 light aircraft with maximum take-off mass (MTOM) < 5,700 kg, while for one large aircraft it is MTOM > 5,700 kg.

The number of events caused by birds was referred to the number of aircraft registered in a given year to objectify the results of comparisons (Balicki W. et al 2016). Coefficient has been

DOI 10.2478/ama-2021-0014

added as:

$$K_{1000} = \frac{1000 * N_{ev}}{N_{reg}} \quad (1)$$

where: N_{ev} is the number of events involving birds and N_{reg} is the number of aircraft registered in the year under consideration.

Tab. 1. Change in the number of aircraft registered in Poland

Year	2007	2009	2010	2012	2013	2014	2016	2017	2018
Light air-craft	1.067	1.044	1.020	1.070	1.086	1.107	1.124	1.145	1,156
Large air-craft	94	96	98	125	113	116	123	133	152

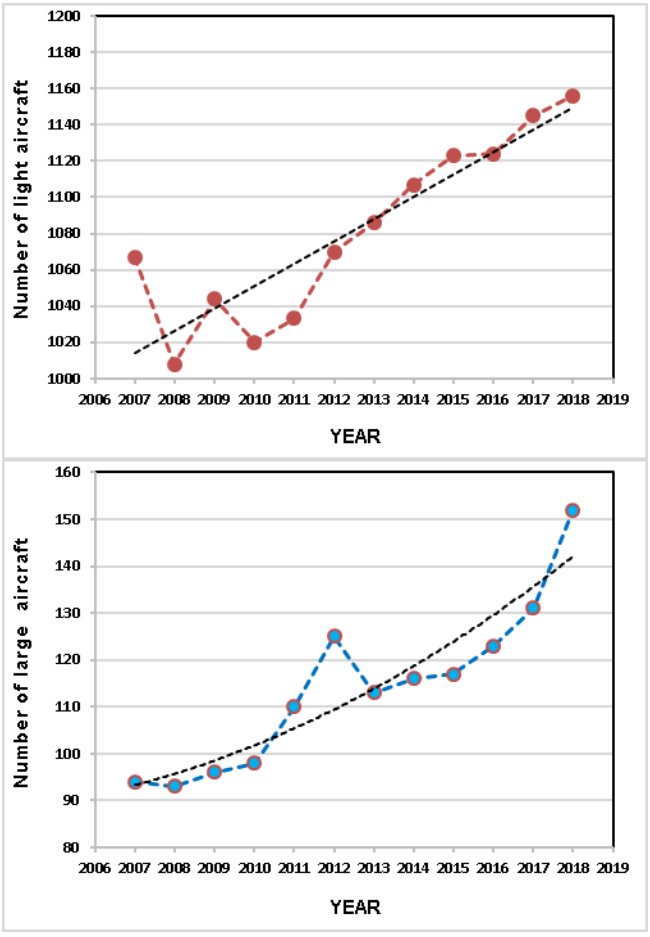

Fig. 1. Change in the number of aircraft registered in Poland

1.2. Effects of collision energy discharge

Previous observations of damage to the fan blades and the blades of the first compressor stages indicate that their collisions with so-called foreign bodies are found most often on 1/4–1/3 of the length of blades – measured from the tips of the shoulder blades.

When the engine is running at the take-off range, the peripheral speeds of the compressor blades at collision points reach 250–300 m/s and the fan blades to even 400 m/s. The energy of colliding with the body of a small bird is said to be similar to the energy of a bullet from a pistol fired (see Tab. 2).

Tab. 2. The energy of a bird hitting an aircraft compares with the weapon bullet energy

	Type of bullet	Mass of bullet	Bullet initial velocity	Energy of bullet
	Bird	Bird	Bird	Bird
Gun P-64 'CZAK'	Makarov 9 mm	6.1 g	310 m/s	293 J
Small airplane speed 200 km/h	Starling	80 g	56 m/s	125 J
Automatic rifle AK-47 'Kalash-nikov'	Intermedi-ate rifle cartridge 7.62 mm	7.91 g	715 m/s	2,022 J
Large aircraft speed 400 km/h	Seagull	500 g	111 m/s	3,080 J
High-calibre WKM M1921	0.50 BMG (12.7 mm)	33–47 g	885–1036 m/s	18,000 J
Large aircraft speed 400 km/h	Goose	2,000 g	111 m/s	12,320 J

The effects of 'discharging' such energy can be surprisingly serious, e.g. a swallow (40 g) can penetrate the cabin cover of a small flying plane and injure the pilot.

The range of damage to the turbine engine depends on the weight of the 'foreign body', flight speed and the range of engine operation (rotation speed). Most often it was found after suctioning as follows:

- a small bird (swallow, starling): disturbance of the flow through the compressor, unstable compressor operation, engine stalling;
- larger bird (seagull, crow, goose): breakage of the fan blades or first stages of the compressor rotor, damage to the air intake, damage to the wing edge, control system, puncture of the pilot cabin fairing.

Unfortunately, as much as 50% of collisions involve seagulls (Dolbeer, 2006; Wildlife Strikes, 2019). In the statistics of military aircraft accidents, the Turkish vulture (body weight > 6 kg), which in the 1990s participated in about 200 collisions, with losses of over 30 million dollars, also occupies a high position.

2. RESULTS OF DATA ANALYSYS

2.1. Light aircraft – with MTOM < 5,700 kg

Fig. 2 shows the percentage share of bird collisions for aircraft with MTOM < 5,700 kg compared to other categories of operational air events. Fig. 3 shows the change in the number of collisions of light aircraft with birds in 2008–2018, and Fig. 4 the change in the $K_{1,000}$ coefficient for this category of aircraft.

There is a systematic increase in this coefficient from 2013, but its values are small. In 2018 it came close to the alert level. Despite the fact that light airplanes very often perform air operations at field (grass) airports, collisions with birds do not dominate in the total number of reported occurrences (unlike large aircraft, for which bird strike is one of the significant causes of collision).

DOI 10.2478/ama-2021-0014

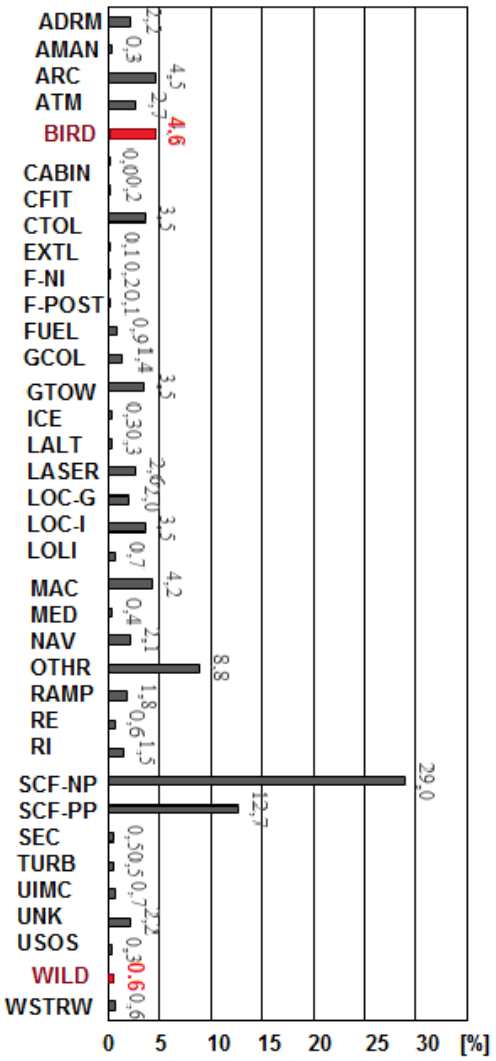

Fig. 2. Percentage share of particular categories of operational aviation events for light aircraft with MTOM < 5,700 kg in 2008–2018

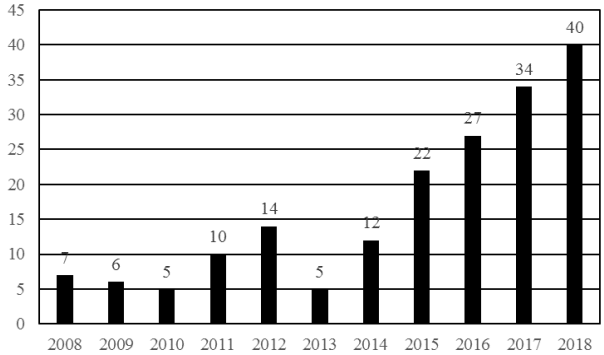

Fig. 3. Number of collisions with birds for light aircraft in the 2008–2018

Tab. 3. Probabilities of a safety hazard

Probability	Description	Size
Frequent	Occurs many times (took place frequently)	**5**

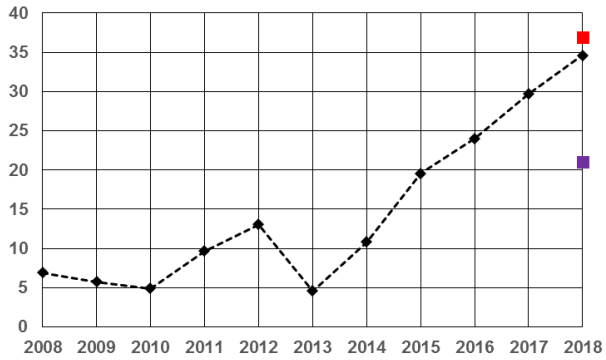

Fig. 4. Change in the $K_{1,000}$ coefficient for light aircraft in the 2008–2018

As shown in Fig. 5, the most frequent collisions with birds occur during the approach, cruising and take-off.

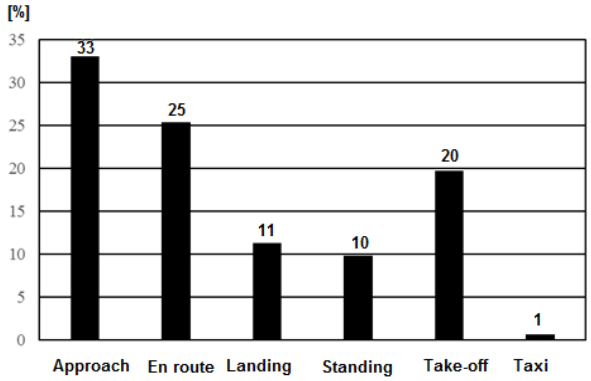

Fig. 5. Percentage of individual light aircraft traffic phases during which collisions with birds were recorded

Tab. 4. Severity assessment, safety risk in the event of collisions with birds

Severity	Description	Level
Lesser	Inconvenience Operational limitation Using emergency procedures Minor incident	**D**

Tab. 5. The real degree of threat to flight safety

Probability of danger	Degree of danger				
	Catastrophic A	Dangerous B	Serious C	Lesser D	Insignificant E
Unlikely	**3** A	3B	3C	**3D**	3E

An important task is to determine the alert levels as well as the level of security threat resulting from bird strikes. To determine the alert levels, the methodology developed at the Institute of Aviation (Balicki at all 2016) was used. The projected average value determined in 2017 for 2018 in the drawings (Fig. 4) is marked in magenta. However, the forecasted alarm level is marked in red. The security risk was determined using the meth-

od described in Safety Management Manual (Applying an SMS 2015, Bird Control 1991, Airport Service 2012). It should be emphasised that in Poland there were no major incidents related to the collision of aircraft with birds. That is why it was accepted that the security risk in this case is not significant. The analysis of the safety risk assessment consists in examining available statistical data and determining the level of collision effects with birds. In this case, it becomes necessary to rely on facts and not consider the potential possible effects of such events. Otherwise, it would lead to a situation in which virtually most aviation events could be classified as severe: level A – i.e. catastrophic. It was assumed on the basis of statistical data that for airplanes with MTOM < 5,700 kg, the security risk has a lower severity, as shown in Tab. 4. However, Tab. 3 presents the assessment of the likelihood of a security risk as isolated (unlikely). From conclusions drawn fromanalysing Tabs 3 and 4, a safety risk assessment matrix is constructed, which is presented in Tab. 5. It shows that for light airplanes, the real degree of threat to flight safety caused by collisions with birds is very low.

2.2. Large aircraft – with MTOM > 5,700 kg

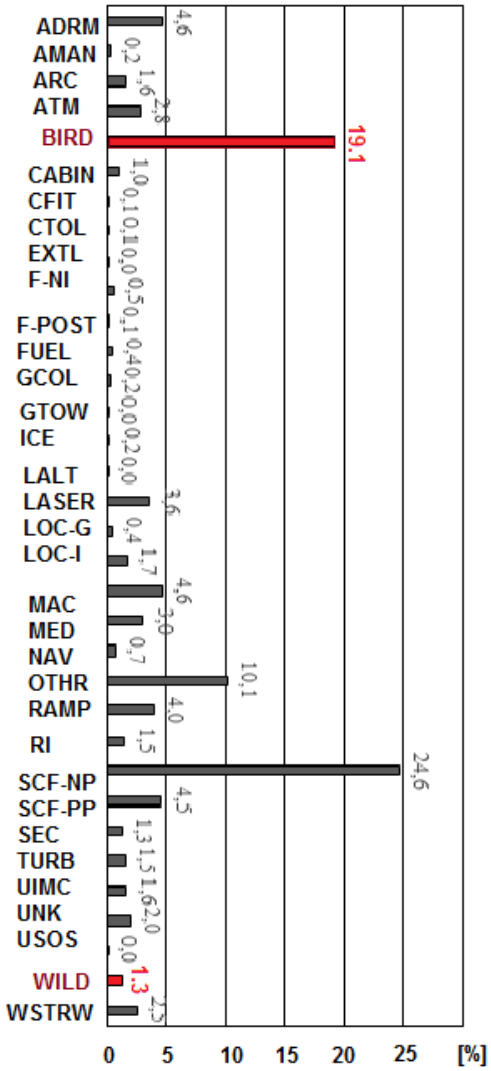

Fig. 6. Percentage share of individual categories of operational aviation events for large aircraft with MTOM > 5,700 kg in 2008–2018

The turbine engines of large aircraft are particularly sensitive to collisions with birds. The Bird Strike Committee Europe recommends, for example, the following:

- Plan the flight route in such a way as to avoid bird flyways;
- Avoid low-altitude flights, especially along sea shores, rivers, cliffs (these are nesting sites), lakes, islands, processing plants (especially fish) and landfills;
- Practice the procedures to be followed in case of damage to the cabin cover, engine damage;
- During landing, after noticing the flock of birds on the final approach to the lane, it is better to stop the landing and go to the second approach (unsuccessful approach procedure);
- After a collision with a bird, if possible, a control test should be carried out before the approach, and if the bird has been sucked into the engine, a flight procedure with a failed engine should be performed.

After a systematic decrease in the number of collisions with birds in the period 2009–2013 in the past 5 years, there was a clear increase. In 2018, despite a much larger number of bird strikes compared to those in 2017, the $K_{1,000}$ ratio dropped due to the fact that the number of registered aircraft had increased. This ratio is between the projected average value and the alert level. The number of aviation events related to bird strikes in the years 2008–2018 is shown in Fig. 7, and in Fig. 8 is shown the values of the $K_{1,000}$ coefficient. It is important to emphasise the fact that, according to the ICAO document, every bird-related event should be recorded, not only those confirmed by traces of impact on the airframe or power unit, but also those that could lead to a collision.

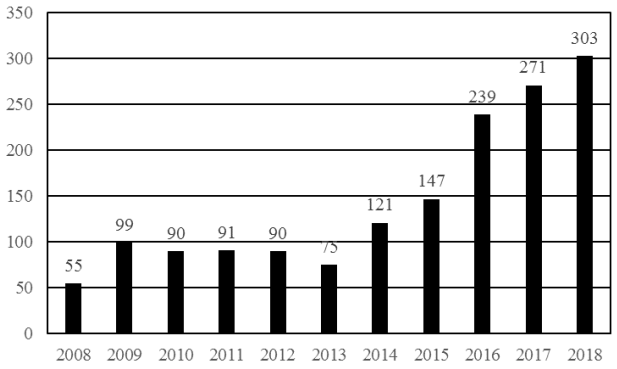

Fig. 7. Increase in the number of collisions with birds for aircraft with MTOM > 5,700 kg between 2008 and 2018

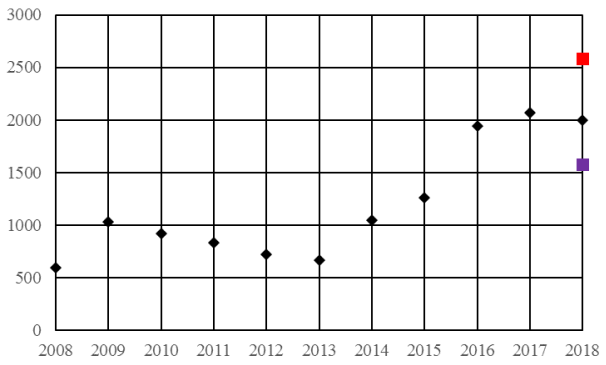

Fig. 8. $K_{1,000}$ values for large aircraft collisions with birds in 2008–2018

DOI 10.2478/ama-2021-0014

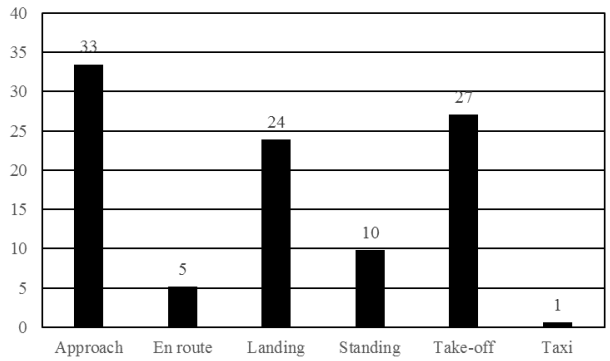

Fig. 9. Percentage of individual large aircraft traffic phases during which collisions with birds were recorded

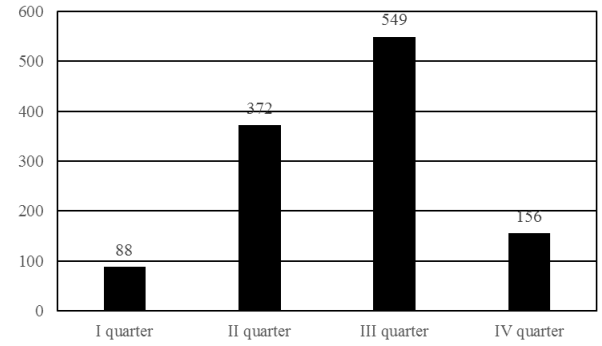

Fig. 10. Number of occurrences with birds near airports in individual quarters for aircraft with MTOM > 5,700 in 2011–2018

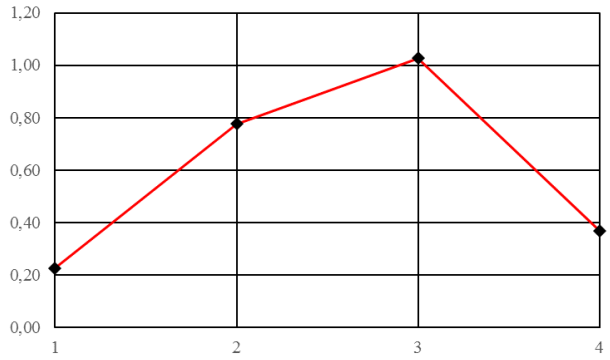

Fig. 11. Values of the number of bird events reported in relation to the number of passenger operations of large aircraft in individual quarters of the year

Fig. 9 shows the percentages of individual phases of flight during which bird strikes were reported. They occur most often during the approach, take-off and landing of the aircraft. It is somewhat obvious because of the limited 'flight altitude range' of birds. Almost every tenth event involving birds is detected only during aircraft inspection.

The above results are attributable to the fact that a significant number of bird collisions are not perceived by the crew and therefore are not reported by the pilots, but are only detected by the maintenance services.

Figs. 10 and 11 show the seasonality of changes of collision factor with birds in the number of passenger operations in 2011–2018. Most of them occur in the third quarter of the year, and the least in the winter.

Similar to the assessment carried out for light aircraft, the safety risk assessment matrix presented in Tab. 8 was developed. Likewise, for light aircraft, the consequences of collisions with birds of large aircraft were of lesser severity (Tab. 7), whereas the probability of this event is frequent (Tab. 6).

Tab. 6. Probabilities of a safety hazard

Probability	Description	Size
Frequent	Occurs many times (took place frequently)	**5**

Tab. 7. Severity assessment, safety risk in the event of collisions with birds

Severity	Description	Level
Lesser	Inconvenience Operational limitation Using emergency procedures Minor incident	**D**

Tab. 8. Real safety risk of performing flights

Probability of danger	Degree of danger				
	Catastrophic A	Dangerous B	Serious C	**Lesser D**	Insignificant E
Frequent	5 A	5B	5C	**5D**	5E

Although the analysis presented shows that the degree of risk is not high, the causes of the systematic increase in aviation events caused by bird strikes should be controlled and appropriate measures taken to reduce the possibility of a serious accident.

3. ACTIONS TO REDUCE THE RISK ASSOCIATED WITH BIRD STRIKES

3.1. Tests of engine resistance to bird collisions

During the implementation of the PZL-I22 'Iryda' aircraft programme, the Institute of Aviation conducted tests of turbine engines' resistance to collisions with birds. This type of research was carried out for the first time in our country, on a specially constructed test stand equipped with a pneumatic launcher and measuring apparatus (see Fig. 12) (Balicki at al., 2016). The pneumatic launcher with a 75-m barrel was supplied with compressed air (maximum pressure 0.8 MPa). The hydraulic retarding device controlled the increase in air pressure, and thus the container with a 'foreign body' (lumps of ice or a bird weighing up to 2 kg) was accelerated with an acceleration of not more than 50 g (g – gravitational acceleration; exceeding 50 g could crush the bird – that is the reason for the barrel length). The trigger unit has been activated by an electric signal from the operator's cab. At the same time, a fast film camera and an electronic container speed measuring system at the exit of the barrel were launched.

DOI 10.2478/ama-2021-0014

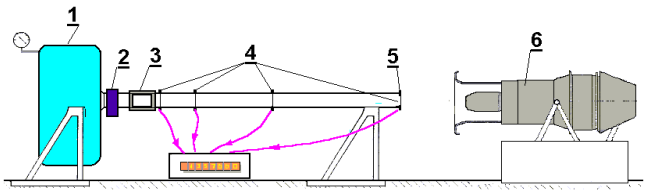

Fig. 12. Schematic diagram of a stand with a pneumatic launcher f or testing engine resistance to foreign body impact: (1 – compressed air tank, 2 – electric trigger with hydraulic delay unit, 3 – container with a 'foreign body', 4 – container speed measuring system, 5 – barrel outlet with a container stop device, 6 – engine tested)

The obtained tank movement speeds depended on the initial air pressure in the tank:

- for a pressure of 0.2 MPa the speed was 160 m/s;
- for 0.8 MPa, the speed was 250 m/s.

According to the regulations, after a collision with a bird shot at 200 m/s into the engine inlet operating in the take-off range, damage to the units may prevent its further operation, but no part of the engine can get out of its nacelle, threatening the airframe structure and its installations.

3.2. Increasing crash resistance by changing engine and airframe design

Experience till date shows that every single-flow engine is destroyed during take-off after a collision with a large animal (over 0.5 kg). This is because the impacted blades of the first stage of the compressor bend and 'rub' against the stationary steering blades behind them. The rotor performs 100–200 rotations per second. The chances of reducing the size and area of damage should be seen in the fragmentation of the bird's body before impacting the rotating vanes. For this purpose, for example, ribs acting as knives were placed in the inlets of a PZL TS-11 aircraft. A similar effect can be achieved by properly shaping (bending) the inlets to the jet engines of combat aircraft so that the birds bumping against the duct walls (at a speed of about 200 m/s) reach the rotors already sufficiently smashed. The use of this method requires appropriate computational and experimental research for each newly designed aircraft. One of the effects of such research is the design of a new, jet engine by General Electric (Dolbeer R.A. 2006), presented in Fig. 13 (GEnx series).

Based on the analysis of the 'foreign object' motion paths, in the inlet and flow ducts of this engine, the shape of the cap (conical–elliptical) was developed so that the falling elements (dust grains, pieces of ice, birds) would be ejected into the external flow duct of the engine, i.e. they would bypass the inlet to the low-pressure compressor. This is also done by increasing the distance between the fan rotor and the compressor inlet. As a result, grains with diameter >0.25 mm are ejected into the outer channel.

The fan blades of the GEnx series engines are made of carbon fibre composites. In the event of breakage, the blade is kept inside the engine nacelle (it does not pierce the nacelle wall), thanks to special reinforcements (bandage – armor) and 'pockets' into which it retracts after detaching from the hub.

When the engine is running in the low thrust range, e.g. when taxiing the plane to the runway, the discharge valves from the low pressure compressor open (inwards). This enables the ejection of finer particles from the compressor into the engine outer duct.

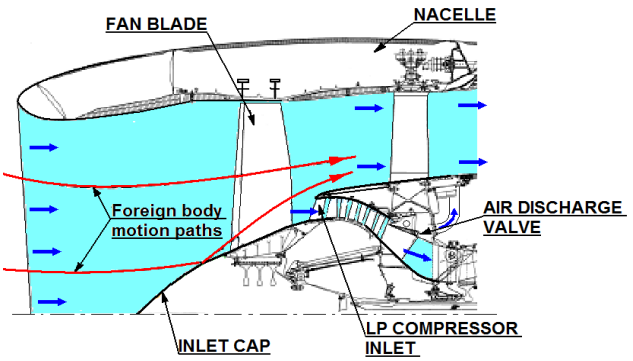

Fig. 13. A method of shaping the inlet of a large jet engine to increase resistance to damage caused by the ingress of a 'foreign body'

3.3. Crash prevention

The development of civilisation often creates conflicts concerning the coexistence of man and nature. Unfortunately, this also applies to the development of air traffic. 'For the safety of both parties', birds should be discouraged from being around airports. This is done by depriving the area of all the elements attractive for them, i.e. liquidation of feeding grounds near airports, drying water reservoirs, removing landfills – sources of food, mowing grass and thus depriving birds of comfortable shelters at the airport (Birdstrike risk, 2007; Shamoun-Baranes, 2008; Summary of Wildlife Strikes, 2017).

Birds repelling is another range of protective measures. For this purpose, the following areused:

- pyrotechnics: firecrackers, automatic gas cannon, firearms;
- acoustic means: e.g. 'shout of fear' reproduced around loudspeakers, or voices of hunting predators (high recording quality must be maintained);
- chemicals: spraying repellents, e.g. anthranilic methylate (range up to 500 m);
- use of trained birds of prey and trained dogs (the most effective border collie, which, however, must be accustomed to airplanes, and denied from entering the runway);
- a motorised 'flying crew' to drive away the flock.

The main disadvantage of all these deterrents is that the birds get used to them and therefore the same method cannot be used for a long time.

Flock detection systems in the vicinity of airports (usually passive infrared sensors) and information on bird migration/flights (satellite telemetry) are used to reduce the likelihood of aircraft encounters with birds. One of the ideas of such a system, presented in Fig. 14, was created during the observation of the spread of the H5N1 bird flu virus and assumes the use of the existing meteorological and military radar network to observe bird behaviour 'in real time'.

This network includes the following:

- long-range military surveillance radars – observation of migration of large flocks of birds within 150 km;
- weather radars – images of bird flights according to flight altitude within 25 km;
- specialised short-range radars (5–10 km) – movements near airports and training grounds.

DOI 10.2478/ama-2021-0014

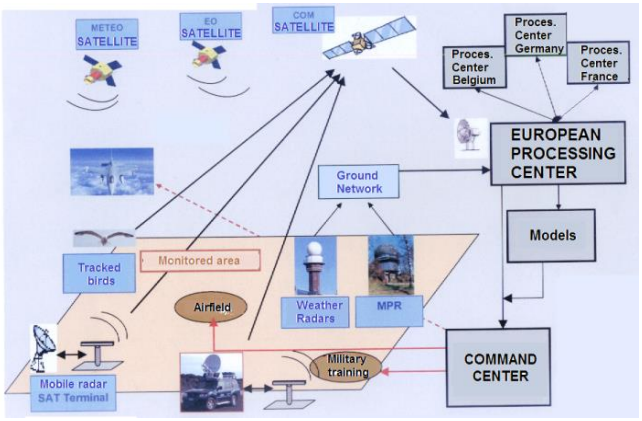

Fig. 14. Concept for a bird migration monitoring system to increase flight safety (Shamoun-Baranes, 2008)

Attempts have already been made to implement such a system to protect NATO air bases in Belgium, with a view to extending it to the Netherlands, France and Germany. Information on the likelihood of encounters of flying birds in the different zones of the observed area and current bird activity near the departure and destination airports is included in the bulletins (e.g. BIRDTAM – Bird Notice To Air Man) and should be taken into account in route planning.

4. CONCLUSION

The analysis of events included in the ECCAIRS database allows us to conclude that in Poland the actual level of risk of a dangerous event involving birds and large aircraft is moderate. However, air surveillance and airport authorities should take action to reduce the number of collisions with birds. Their number has been constantly increasing since 2013 – since then the probability of such an event has increased by four times.

Due to the increasing risk of collisions, there is a need for behavioural studies of birds in the vicinity of airports. Climate change, food distribution sites and low risk from predators contribute to their presence. They are also likely to become accustomed to the ways that are being used to deter them.

Every tenth collision with a bird is not noticed by the crew and its effects are only detected during technical inspections of aircraft.

What is puzzling is the small number of incidents reported for light aircraft (MTOM < 5,700 kg), although they operate mostly at airports and in remote areas. According to the current legal regulations, the level of self-service of small aircraft is expanding. In the current system, reporting of bird crashes should not be expected to increase due to the fact that the level of risk is accepted by small aircraft owners. It therefore seems appropriate to review the standards that cover bird collisions and related requirements. The results of analyses and examples of incidents related to bird collisions should also be disseminated in the industry and in specialised publications.

REFERENCES

1. Applying an SMS Approach to Wildlife Hazard Management, (2015) Airport Cooperative Research Program Report 145, National Academy of Sciences. Transportation Research Board, Washington D.C.
2. **Balicki W., Głowacki P., Loroch L** (2016), Safety performance indicators assessment for small aircraft airframe systems, *Journal of KONES Powertrain and Transport*, 23(2), 31–38.
3. Bird Control and Reduction, Airport Services Manual, (1991) Third Edition, Doc 9137 - AN/898, Part 3 Montreal, Canada,
4. Bird strike, a European risk with local specificities, (2013), European General Aviation Safety Team, Edition 1 – Germany,
5. Birdstrike risk/Warning procedures, (2007) STANAG 3879 FS (Edition 7), Military Committee Standardization Board (MCASB), NATO Standardization Agency
6. **Cleary E.C., Dolbeer R. A.** (2005), *Wildlife hazard management at airports, a manual for airport operators*, Second edition, Federal Aviation Administration, Office of Airport Safety and Standards, Washington, D.C. USA,
7. Convention on International Civil Aviation, Chicago 1944, doc 7300/9, Ninth Edition, available at: www.icao.int
8. **Dale L.A.** (2009), Personal and corporate liability in the aftermath of bird strikes: a costly consideration, University of Nebraska – Lincoln, Human – Wildlife Conflicts 3(2), 216–225,
9. Directive 2003/42/EC of the European Parliament and of the Council on occurrence reporting in civil aviation, (2003) Official Journal L 167, 04.07.2003, pp. 23 – 36
10. **Dolbeer R. A.** (2006), *Bird and Other Wildlife Hazards at Airports: Liability Issues for Airport Managers*, University of Nebraska – Lincoln, Wildlife Damage Management, Internet Center for USDA National Wildlife Research Center - Staff Publications,
11. Federal Aviation Administration (1990–1999), Wildlife strikes to civil aircraft in the USA,
12. **Fernandez -Juricic E., Gaffney J., Blackwell B., Baumhardt P**., (2011), Bird strikes and aircraft fuselage color: a correlational study, Human–Wildlife Interactions 5(2): 224–234,
13. **Fortońska A.** (2018), *The impact of bird strikes on air transport safety*, Scientific Papers of Silesian University of Technology. Transport, vol. 98.
http: //digitalcommons.unl.edu/hwi/12
http://digitalcom mons.unl.edu/icwdm usdanwrc/142
14. ICAO, (2012), Airport Service Manual. Wildlife Control and Reduction, Doc 9137P3 AN/898, Fourth Edition, ISBN 978-92-9231-929-8
15. **Kelly T.C., Allan J.** (2006), *Ecological effect of aviation*, in Davenport J. and Davenport J.L. editors. The ecology of transportation: managing mobility for the environment, Springer, Dordrecht, Netherlands,
16. **Korte G.** (2019), Planes strike birds more than 40 times a day, FAA data show, USA TODAY
17. **Matijaca A.** (2001), Damage Liability and Compensation in Case of Bird Strike, *Proceedings of the 3-rd Joint Bird Strike Committee USA/Canada*, Calgary, 89–100, http://www.int - birdstrike.org.
18. **Matijaca A**., (2008), Possible Exoneration of Airport from liability for bird strike damage. Proceedings of the 28-th International Bird Strike Committee, Brasil, 1–16, ://www.int - birdstrike.
19. Regulation (EC) No 261/2004 of the European Parliament and of the Council of 11 February (2004) establishing common rules on compensation and assistance to passengers in the event of denied boarding and of cancellation or extended delay of flights, and repealing, Regulation (EEC).Official Journal No 295/91, No 46, p. 1.
20. **Reza H., Mojtaba S.**(2015), *Bird Strike, an Experimental, Theoretical and Numerical Investigation*, Woodhead Publishing in Mechanical Engineering, Elsevier Ltd.
21. **Shamoun-Baranes J.** (2008), *The Bird Migration System of Systems FlySafe and Beyond*, IAP information day, Brussels,
22. Summary of Wildlife Strikes Reported to the ICAO Bird Strike Information System (IBIS) for the years 2008 – 2015, ICAO EB 2017/25, 12 May 2017.
23. Wildlife Strikes to Civil Aircraft in the United States 1990s2017, FAA Washington, DC. January 2019